

DEPARTMENT OF PHYSICS, UNIVERSITY OF JYVÄSKYLÄ

**JET TRANSVERSE MOMENTUM DISTRIBUTIONS
MEASURED BY ALICE**

**BY
TOMAS SNELLMAN**

PHD thesis

Supervisors: Jan Rak, Dong Jo Kim

Jyväskylä, Finland
December, 2018

3 Contents

4	1	Introduction	3
5	1.1	Quantum chromodynamics	4
6	1.1.1	Foundation of QCD	4
7	1.1.2	Asymptotic Freedom	5
8	1.2	heavy-ion physics	9
9	1.2.1	History	9
10	1.3	Features of Heavy-Ion Collisions	10
11	1.3.1	Collision Geometry	10
12	1.3.2	Nuclear Geometry	12
13	1.3.3	Hydrodynamical Modelling	15
14	1.4	Flow	18
15	1.4.1	Anisotropic Flow	19
16	1.5	Hard processes	20
17	1.5.1	pQCD factorization	20
18	1.5.2	Jet hadronisation	23
19	1.5.3	Jet energy loss	27
20	1.5.4	New paradigm of jet Quenching	33
21	1.5.5	Jet shape measurements	36
22	1.6	QGP in Small systems	36
23	1.6.1	Collective phenomena	38
24	1.6.2	Absence of jet quenching	39
25	1.6.3	Centrality determination in small systems	39
26	2	Experimental Setup	43
27	2.1	CERN	43
28	2.2	Large Hadron Collider	44
29	2.2.1	LHC experiments	45
30	2.3	ALICE	46
31	2.3.1	Tracking	47
32	2.3.2	TPC	49
33	2.3.3	TPC upgrade	49
34	2.3.4	Particle identification	53
35	2.3.5	Electromagnetic Calorimeter	54
36	2.3.6	Forward and trigger detectors	54
37	2.3.7	Muon spectrometer	57

38	2.3.8 Triggers	57
39	3 Event and track selection	60
40	3.1 Event selection	60
41	3.2 Track reconstruction	60
42	3.3 Cluster selection	64
43	4 Analysis method	66
44	4.1 Jet Finding	66
45	4.1.1 Anti k_T algorithm	66
46	4.2 Definition of j_T	67
47	4.3 Unfolding detector effects	69
48	4.3.1 Bayesian unfolding	70
49	4.3.2 Toy Monte Carlo	72
50	4.3.3 Pythia Response matrices	73
51	4.3.4 Unfolding algorithm	74
52	4.3.5 Unfolding closure test	74
53	4.4 Background	77
54	4.4.1 Perpendicular cone background	77
55	4.4.2 Random background	78
56	4.4.3 Auto-correlations	78
57	4.4.4 Comparing background methods	79
58	4.5 Fitting	80
59	5 Systematic errors	82
60	5.1 Background	82
61	5.2 Unfolding	82
62	5.2.1 Effect of number of iterations	83
63	5.2.2 Effect of different prior	85
64	5.2.3 Effect of p_T truncation	85
65	5.3 Tracking	86
66	5.4 EMCal clusters	87
67	5.5 Summary/Combining systematics	87
68	5.6 Additional checks	88
69	5.6.1 Comparison between A and C side	88
70	6 Results	90
71	6.1 Fitting	90
72	6.1.1 RMS values from fitted distributions	90
73	6.2 High multiplicity	90

⁷⁴	7	Discussion	93
⁷⁵	7.1	Dihadron j_T	93
⁷⁶	7.2	Comparing dihadron and jet j_T results	94
⁷⁷	7.2.1	Different R parameters	95
⁷⁸	7.2.2	Leading tracks versus jet	96
⁷⁹	8	Summary	98
⁸⁰	Appendices		99
⁸¹	A	Additional graphs	99

82 1 Introduction

83 REWRITE At sufficiently high energies quarks and gluons are no longer bound to
84 hadrons, but they form a deconfined state known as Quark-Gluon plasma (QGP).
85 The main goal of heavy-ion physics is the study of QGP and its properties. One
86 of the experimental observables that is sensitive to the properties of QGP is the
87 azimuthal distribution of particles in the plane perpendicular to the beam direc-
88 tion.

89 When nuclei collide at non-zero impact parameter (non-central collisions), their
90 overlap region is asymmetric. This initial spatial asymmetry is converted via multi-
91 ple collisions into an anisotropic momentum distribution of the produced particles.
92 For low momentum particles ($p_T \lesssim 3$ GeV/c), this anisotropy is understood to
93 result from hydrodynamically driven flow of the QGP [3–7].

94 One way to characterize this anisotropy is with coefficients from a Fourier se-
95 ries parametrization of the azimuthal angle distribution of emitted hadrons. The
96 second order coefficient, v_2 which is also known as elliptic flow, shows clear depen-
97 dence on centrality. The collision geometry is mainly responsible for the elliptic
98 flow. Higher harmonics don't depend that much on centrality. These higher har-
99 monics carry information about the fluctuations in collisions. The event-by-event
100 fluctuations have an increasing importance in measurements and it has been ob-
101 served that measurements of elliptic flow in central collisions and measurements
102 of higher order harmonics are consistent with the assumption that flow in these
103 cases is mainly due to fluctuations [8].

104 At LHC energies $\sqrt{s_{NN}} = 2.76\text{GeV}$ it has been observed that in general there
105 is little difference to flow at RHIC energies. The v_2 coefficient is about 20% greater
106 at LHC than at RHIC, depending on the centrality bin. The particle identified
107 v_2 for kaons and pions follows the same trend. However it was observed that for
108 proton v_2 the quark number scaling does not work [9]. So far there is no agreement
109 of why this scaling breaks down at LHC or why it works so well at RHIC energies.

110

111 **1.1 Quantum chromodynamics**

112 **1.1.1 Foundation of QCD**

113 There are four known basic interactions in the universe: gravity, electromagnetic,
114 weak and strong interactions. The standard model of particle physics includes
115 three of these, excluding the gravitational interaction. The theory of strong inter-
116 actions is known as Quantum Chromodynamics (QCD).

117 The development of QCD began after the introduction of new powerful particle
118 accelerators that were capable of particle physics research in the 1950s. Before this
119 particles were mainly discovered from cosmic rays. Positrons, neutrons and muons
120 were discovered in the 1930s and charged pions were discovered in 1947 []. The
121 neutral pion was discovered in 1950 [10].

122 The Lawrence Berkeley National Laboratory started the Bevalac accelerator in
123 1954, Super Proton Synchrotron (SPS) in CERN began operating in 1959 and the
124 Alternating Gradient Synchrotron (AGS) at Brookhaven started in 1960. With
125 an energy of 33 GeV AGS was the most powerful accelerator of that time. By
126 the beginning of 1960s several new particles had been discovered. These included
127 antiprotons, antineutrons, Δ -particles and the six hyperons (Ξ^0 , Ξ^- , Σ^\pm , Σ^0 and
128 Λ).

129 Facing this avalanche of new particles, physicists started the search for symme-
130 tries within them. Already in 1932 Heisenberg [11] had proposed an isospin model
131 to explain similarities between the proton and the neutron. In 1962 Gell-Mann
132 and Ne'eman presented that particles sharing the same quantum numbers (spin,
133 parity) could be organised using the symmetry of SU(3). [12] Heisenberg's Isospin
134 model followed the symmetry of SU(2). Using the SU(3) model known baryons
135 and mesons could be presented as octets. This also lead to the discovery of the
136 Ω^- particle since this was missing from the SU(3) decouplet that included heavier
137 baryons.

138 The most simple representation of SU(3) was a triplet. Inside this triplet parti-
139 cles would have electric charges $2/3$ or $-1/3$. However, these had not been detected.
140 In 1964 Gell-Mann [13] and Zweig proposed that baryons and mesons would be
141 bound states of these three hypothetical triplet particles that Gell-Mann called
142 quarks. Now we know that these are the u , d and s quarks. This original quark
143 model without colour was violating the Pauli exclusion principle. For example
144 the Ω^- particle is comprised of three s quarks which would have exactly the same
145 quantum states.

146 The first one to present the idea of colour was Greenberg already in 1964 [14].
147 In 1971 Gell-Mann and Fritsch presented their model, which solved the antisym-
148 metry problem. They added a colour quantum number to quarks, which separated
149 quarks of the same species. In the new colour model the baryonic wave function

150 became

$$(qqq) \rightarrow (q_r q_g q_b - q_g q_r q_b + q_b q_r q_g - q_r q_b q_g + q_g q_b q_r - q_b q_g q_r), \quad (1)$$

151 The colour model was also supported by experimental evidence. The decay
152 rate of a neutral pion with the addition of colours is

$$\Lambda(\pi^0 \rightarrow \gamma\gamma) = \frac{\alpha^2}{2\pi} \frac{N_c^2}{3^2} \frac{m_\pi^3}{f_\pi^2}. \quad (2)$$

153 For $N_c = 3$ this gives 7.75 eV and the measured value is (7.86 ± 0.54) eV [15].

154 Another observable that combines the colour information also to the number
155 of quark flavours is the Drell-Ratio R [16]

$$R = \frac{\sigma(e^+ + e^- \rightarrow \text{hadrons})}{\sigma(e^+ + e^- \rightarrow \mu^+ + \mu^-)} = N_c \sum_f Q_f^2. \quad (3)$$

156 This ratio has the numerical value 2 when including the three light quarks u , d
157 and s . When the collision energy reaches the threshold of heavy quark (c and
158 b) production processes this increases to $^{10}/_3$ (for $f = u, d, s, c$) and $^{11}/_3$ (for $f =$
159 u, d, s, c, b). The energy threshold ($\sqrt{s} \approx 350$ GeV) of $t\bar{t}$ production, has not been
160 reached so far by any e^+e^- colliders.

161 The colour model explained why no free quarks had been observed as only
162 colour neutral states are possible. The simplest ways of producing a colour neu-
163 tral object are the combination of three quarks, and the combination of a quark-
164 antiquark pair. These are known as baryons and mesons.

165 After the addition of colour the main ingredients of QCD had been estab-
166 lished. The final quantum field theory of Quantum Chromodynamics formed
167 quickly between 1972 and 1974. Main part of this was the work by Gross, Wilczek,
168 Politzer and George for non-abelian gauge field theories [17–21]. Gross, Wilczek
169 and Politzer received the Nobel Prize in Physics for their work. The role of gluons
170 as a colour octet was presented by Fritzsch, Gell-Mann and Leutwyler in 1973 [22].
171 The theory had now 8 massless gluons to mediate the strong interaction.

172 However, these gluons had not been discovered. Indirect evidence of the ex-
173 istence had been seen as it was observed that only about half of the momentum
174 of protons was transported by the quarks [23]. Direct evidence should be seen in
175 electron-electron collisions as a third, gluonic, jet in addition to two quark jets.
176 Three jet events were first seen in 1979 at the PETRA accelerator at DESY [24–26].

177 1.1.2 Asymptotic Freedom

178 In Quantum Electrodynamics (QED) the electric charge is screened. In the vicinity
179 of a charge, the vacuum becomes polarized. Virtual charged particle-antiparticle

¹⁸⁰ pairs around the charge are arranged so that opposing charges face each other.
¹⁸¹ Since the pairs also include an equal amount opposite charge compared to the
¹⁸² original charge the average charge seen by an observer at a distance is smaller.
¹⁸³ When the distance to the charge increases the effective charge decreases until the
¹⁸⁴ coupling constant of QED reaches the fine-structure constant $\alpha = \frac{1}{137}$.

¹⁸⁵ Contrary to QED, QCD is a non-abelian theory. In other words the generators
¹⁸⁶ of the symmetry group of QCD, SU(3), do not commute. This has the practical
¹⁸⁷ consequence that gluons interact also with other gluons, whereas in QED the
¹⁸⁸ neutral carrier particles, photons, only interact with charged particles. There
¹⁸⁹ is screening also in QCD because of the colour charges, but in addition to that
¹⁹⁰ there is antiscreening because of the gluon interactions. In QCD the antiscreening
¹⁹¹ effect dominates over screening. Thus for larger distances to the colour charge
¹⁹² the coupling constant is larger. This explains why no free colour charges can be
¹⁹³ observed. When the distance between charges increases the interaction strengthens
¹⁹⁴ until it is strong enough to produce a new quark-antiquark pair.

¹⁹⁵ On the other hand, at very small distances the coupling constant approaches
¹⁹⁶ 0. This is called asymptotic freedom. For large energies and small distances
¹⁹⁷ the coupling constant is negligible. In 1975 Collins [27] predicted a state where
¹⁹⁸ individual quarks and gluons are no longer confined into bound hadronic states.
¹⁹⁹ Instead they form a bulk QCD matter that Edward Shuryak called Quark-Gluon
²⁰⁰ plasma in his 1980 review of QCD and the theory of superdense matter [28]. QGP
²⁰¹ can be seen as a separate state of matter. A schematic view of a phase diagram
²⁰² for QCD matter is shown in Fig. 1.

²⁰³ In the early universe at the age of 10^{-6} s after the Big Bang the conditions
²⁰⁴ preferred the existence of QGP instead of hadronic matter. Nowadays bulk QCD
²⁰⁵ matter, its properties and its phase transitions between hadronic matter and the
²⁰⁶ quark-gluon plasma (QGP) can be explored in the laboratory, through collisions
²⁰⁷ of heavy atomic nuclei at ultra-relativistic energies. The study of QCD matter at
²⁰⁸ high temperature is of fundamental and broad interest. The phase transition in
²⁰⁹ QCD is the only phase transition in a quantum field theory that can be probed by
²¹⁰ any present or foreseeable technology.

²¹¹ One important property of the QGP is the shear viscosity to entropy ratio,
²¹² η/s . It is believed that this ratio has an universal minimum value of $1/4\pi \approx 0.08$,
²¹³ among all substances in nature. This limit would be reached in the strong coupling
²¹⁴ limit of certain gauge theories [30]. The temperature dependance of the ratio is
²¹⁵ shown in Fig. 2. The minimum value of η/s is found in the vicinity of the critical
²¹⁶ temperature, T_c [31]. Finding the η/s values in QGP matter would therefore also
²¹⁷ provide a way of determining the critical point of QCD matter.

²¹⁸ The η/s value for the matter created in Au-Au collisions at RHIC ($\sqrt{s_{NN}}$) has
²¹⁹ been estimated to be 0.09 ± 0.015 [31], which is very close to the lowest value for a

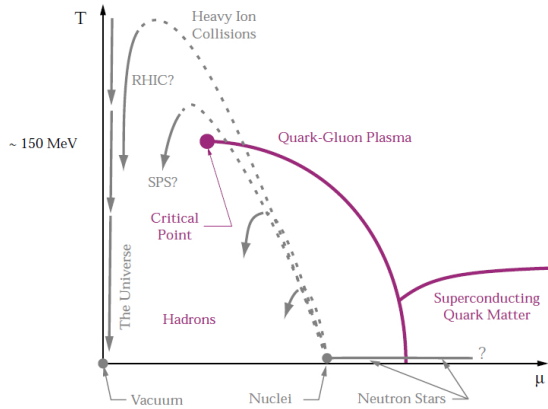


Figure 1: A schematic outline for the phase diagram of QCD matter at ultra-high density and temperature. The quark chemical potential μ that is on the x-axis represents the imbalance between quarks and antiquarks. At zero temperature this corresponds to the number of quarks but at higher temperatures there are also additional pairs of quarks and antiquarks. Along the horizontal axis the temperature is zero, and the density is zero up to the onset transition where it jumps to nuclear density, and then rises with increasing μ . Neutron stars are in this region of the phase diagram, although it is not known whether their cores are dense enough to reach the quark matter phase. Along the vertical axis the temperature rises, taking us through the crossover from a hadronic gas to the quark-gluon plasma. This is the regime explored by high-energy heavy-ion colliders. [29]

wide class of thermal quantum field theories [30] for all relativistic quantum field theories at finite temperature and zero chemical potential. This suggests that the matter created goes through a phase where it is close to the critical point of QCD.

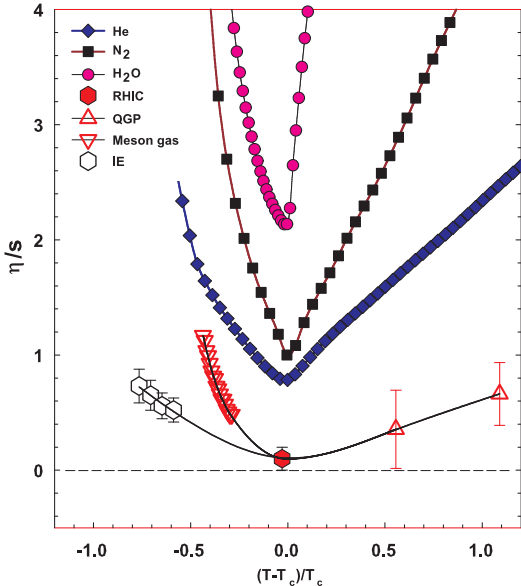


Figure 2: η/s as a function of $(T - T_c)/T_c$ for several substances as indicated. The calculated values for the meson-gas have an associated error of $\sim 50\%$. The lattice QCD value $T_c = 170$ MeV is assumed for nuclear matter. The lines are drawn to guide the eye. [31]

224 1.2 heavy-ion physics

225 The Quark Gluon Plasma (QGP) is experimentally accessible by colliding heavy-
226 ions at high energies. Nowadays research of Heavy-Ion Collisions is mainly per-
227 formed at two particle colliders; The Relativistic heavy-ion Collider (RHIC) at
228 BNL in New York, USA and the Large Hadron Collider (LHC) at CERN in Switzer-
229 land. Energy densities at these colliders should be enough to produce QGP and
230 convincing evidence of the creation has been seen at both colliders.

231 The development of heavy-ion physics is strongly connected to the development
232 of particle colliders. Experimental study of relativistic heavy-ion collisions has been
233 carried out for three decades, beginning with the Bevalac at Lawrence Berkeley
234 National Laboratory (LBNL) [32], and continuing with the AGS at Brookhaven
235 National Laboratory (BNL) [33], CERN SPS [34], RHIC at BNL and LHC at
236 CERN.

237 1.2.1 History

238 The first heavy-ion collisions were performed at the Bevalac experiment at the
239 Lawrence Berkeley National Laboratory [32] and at the Joint Institute for Nu-
240 clear Research in Dubna [35] at energies up to 1GeV per nucleon. In 1986 the
241 Super Proton Synchrotron (SPS) at CERN started to look for QGP signatures in
242 O+Pb collisions. The center-of-mass energy per colliding nucleon pair ($\sqrt{s_{NN}}$)
243 was 19.4 GeV [34]. These experiments did not find any decisive evidence of the
244 existence of QGP. In 1994 a heavier lead (Pb) beam was introduced for new experi-
245 ments at $\sqrt{s_{NN}} \approx 17$ GeV. At the same time the Alternating Gradient Synchrotron
246 (AGS) at BNL, Brookhaven collided ions up to ^{32}S with a fixed target at energies
247 up to 28 GeV [33]. Although the discovery of a new state of matter was reported
248 at CERN, these experiments provided no conclusive evidence of QGP. Now SPS
249 is used with 400 GeV proton beams for fixed-target experiments, such as the SPS
250 heavy-ion and Neutrino Experiment (SHINE) [36], which tries to search for the
251 critical point of strongly interacting matter.

252 The Relativistic heavy-ion Collider (RHIC) at BNL in New York, USA started
253 its operation in 2000. The top center-of-mass energy per nucleon pair at RHIC, 200
254 GeV, was reached in the following years. The results from the experiments at RHIC
255 have provided a lot of convincing evidences that QGP was created [3,4,37,38]. The
256 newest addition to the group of accelerators capable of heavy-ion physics is the
257 Large Hadron Collider (LHC) at CERN, Switzerland. LHC started operating in
258 November 2009 with proton-proton collisions. First Pb-Pb heavy-ion runs started
259 in November 2010 with $\sqrt{s_{NN}} = 2.76$ TeV, over ten times higher than at RHIC.
260 Among the six experiments at LHC, the Large Ion Collider Experiment (ALICE)
261 is dedicated to heavy-ion physics. Also CMS and ATLAS have active heavy-ion

²⁶² programs.

Table 1: Summary of datasets

Run 1 (2009-2013)			Run 2 (2015-2018)		
pp	0.9 TeV	$\sim 200 \mu\text{b}^{-1}$	pp	5.02 TeV	$\sim 1.3 \text{ pb}^{-1}$
	2.76 TeV	$\sim 100 \text{ nb}^{-1}$		13.0 TeV	$\sim 25 \text{ pb}^{-1}$
	7.0 TeV	$\sim 1.5 \text{ pb}^{-1}$	p-Pb	5.02 TeV	$\sim 3 \text{ nb}^{-1}$
	8.0 TeV	$\sim 2.5 \text{ pb}^{-1}$		8.16 TeV	$\sim 25 \text{ nb}^{-1}$
p-Pb	5.02 TeV	$\sim 15 \text{ nb}^{-1}$	XeXe	5.44 TeV	$\sim 0.3 \mu\text{b}^{-1}$
Pb-Pb	2.76 TeV	$\sim 75 \mu\text{b}^{-1}$	Pb-Pb	5.02 TeV	$\sim 1 \text{ nb}^{-1}$

263 **1.3 Features of Heavy-Ion Collisions**

264 **1.3.1 Collision Geometry**

265 In contrast to protons atomic nuclei are objects with considerable transverse size.
266 The properties of a heavy-ion collision depend strongly on the impact parameter
267 b which is the vector connecting the centers of the two colliding nuclei at their
268 closest approach. One illustration of a heavy-ion collision is shown in Fig. 3.

269 Impact parameter defines the reaction plane which is the plane spanned by b
270 and the beam direction. Ψ_{RP} gives the angle between the reaction plane and some
271 reference frame angle. Experimentally the reference frame is fixed by the detector
272 setup. Reaction plane angle cannot be directly measured in high energy nuclear
 collisions, but it can be estimated with the event plane method [39].

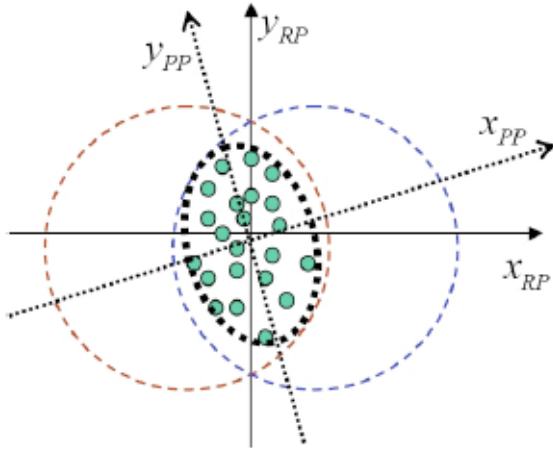


Figure 3: The definitions of the Reaction Plane and Participant Plane coordinate systems [40]. The dashed circles represent the two colliding nuclei and the green dots are partons that take part in the collision. x_{PP} and x_{RP} are the participant and reaction planes. The angle between x_{RP} and x_{PP} is given by Eq. (4). y_{PP} and y_{RP} are lines perpendicular to the participant and reaction planes.

273
274 Participant zone is the area containing the participants. The distribution of
275 nucleons in the nucleus exhibits time-dependent fluctuations. Because the nucleon
276 distribution at the time of the collision defines the participant zone, the axis of
277 the participant zone fluctuates and can deviate from the reaction plane. The angle
278 between the participant plane and the reaction plane is defined by [41]

$$\psi_{PP} = \arctan \frac{-2\sigma_{xy}}{\sigma_y^2 - \sigma_x^2 + \sqrt{(\sigma_y^2 - \sigma_x^2)^2 + 4\sigma_{xy}^2}}, \quad (4)$$

279 where the σ -terms are averaged over the energy density.

$$\sigma_y^2 = \langle y^2 \rangle - \langle y \rangle^2, \sigma_x^2 = \langle x^2 \rangle - \langle x \rangle^2, \sigma_{xy} = \langle xy \rangle - \langle x \rangle \langle y \rangle \quad (5)$$

280 The impact parameter is one way to quantize the centrality of a heavy-ion
 281 collision but it is impossible to measure in a collision. It can be estimated from
 282 observed data using theoretical models, but this is always model-dependent and
 283 to compare results from different experiments one needs an universal definition for
 284 centrality. The difference between central and peripheral collisions is illustrated
 285 in Fig. 4. In a central collision the overlap region is larger than in a peripheral
 286 collision. Larger overlap region translates into a larger number of nucleons partici-
 287 pating in the collision, which in turn leads to a larger number of particles produced
 288 in the event.

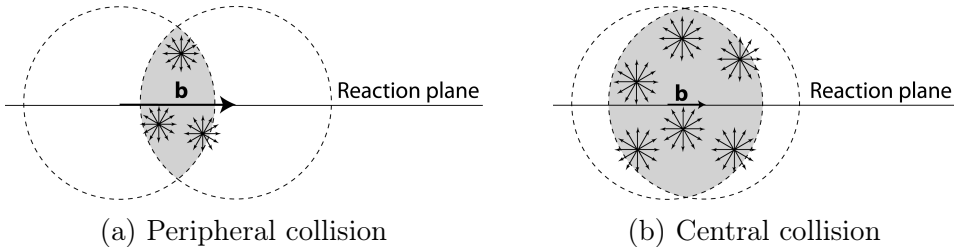


Figure 4: Interaction between partons in central and peripheral collisions. The snowflakes represent elementary parton-parton collisions. When the impact parameter b is large the number of elementary collisions is small. Particle production is small. Smaller impact parameter increases the number of elementary collisions. This increases particle production.

289 Usually centrality is defined by dividing collision events into percentile bins by
 290 the number participants or experimentally by the observed multiplicity. Centrality
 291 bin 0-5% corresponds to the most central collisions with the highest multiplicity
 292 and higher centrality percentages correspond to more peripheral collisions with
 293 lower multiplicities. A multiplicity distribution from ALICE measurements [42]
 294 illustrating the centrality division is shown in Fig. 5. The distribution is fitted
 295 using a phenomenological approach based on a Glauber Monte Carlo [43] plus a
 296 convolution of a model for the particle production and a negative binomial distri-
 297 bution.

298 1.3.2 Nuclear Geometry

299 To model heavy-ion collisions one must first have a description as good as possible
 300 of the colliding objects. Atomic nuclei are complex ensembles of nucleons. The
 301 nuclei used in heavy-ion physics have in the order of 200 nucleons. Mostly used

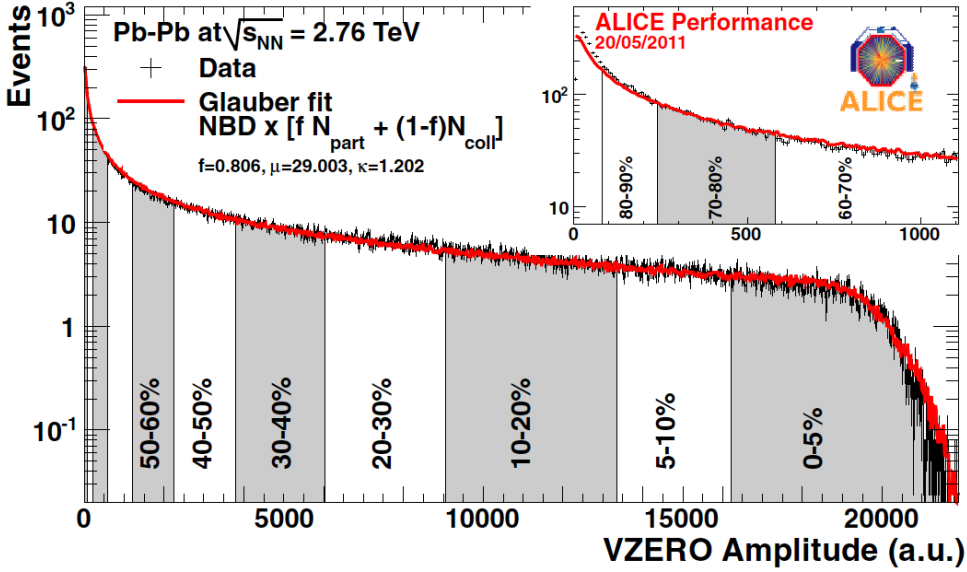


Figure 5: An illustration of the multiplicity distribution in ALICE measurements. The red line shows the fit of the Glauber calculation to the measurement. The data is divided into centrality bins [42]. The size of the bins corresponds to the indicated percentile.

nuclei are ^{208}Pb at LHC and ^{197}Au at RHIC. The distribution of these nucleons within a nucleus is not uniform and is subject to fluctuations in time.

Nuclear geometry in heavy-ion collisions is often modelled with the Glauber Model. The model was originally developed to address the problem of high energy scattering with composite particles. Glauber presented his first collection of papers and unpublished work in his 1958 lectures [44]. In the 1970's Glauber's work started to have utility in describing total cross sections. Maximon and Czyz applied it to proton-nucleus and nucleus-nucleus collisions in 1969 [45].

In 1976 [46] Białas, Bleszyński, and Czyz applied Glauber's approach to inelastic nuclear collisions. Their approach introduced the basic functions used in modern language including the thickness function and the nuclear overlap function. Thickness function is the integral of the nuclear density over a line going through the nucleus with minimum distance s from its center

$$T_A(s) = \int_{-\infty}^{\infty} dz \rho(\sqrt{s^2 + z^2}). \quad (6)$$

This function gives the thickness of the nucleus, i.e. the amount material seen by a particle passing through it.

³¹⁷ Overlap function is an integral of the thickness functions of two colliding nuclei
³¹⁸ over the overlap area. This can be seen as the material that takes part in the
³¹⁹ collision. It is given as a function of the impact parameter b

$$T_{AB}(b) = \int ds^2 T_A(\bar{s}) T_B(\bar{s} - \bar{b}) \quad (7)$$

³²⁰ The average overlap function, $\langle T_{AA} \rangle$, in an A-A collisions is given by [47]

$$\langle T_{AA} \rangle = \frac{\int T_{AA}(b) db}{\int (1 - e^{-\sigma_{pp}^{inel} T_{AA}(b)}) db}. \quad (8)$$

³²¹ Using $\langle T_{AA} \rangle$ one can calculate the mean number of binary collisions

$$\langle N_{coll} \rangle = \sigma_{pp}^{inel} \langle T_{AA} \rangle, \quad (9)$$

³²² where the total inelastic cross-section, σ_{pp}^{inel} , gives the probability of two nucleons
³²³ interacting. The number of binary collisions is related to the hard processes in a
³²⁴ heavy-ion collision. Each binary collision has equal probability for direct produc-
³²⁵ tion of high-momentum partons. Thus the number of high momentum particles is
³²⁶ proportional to $\langle N_{coll} \rangle$.

³²⁷ Soft production on the other hand is related to the number of participants.
³²⁸ It is assumed that in the binary interactions participants get excited and further
³²⁹ interactions are not affected by previous interactions because the time scales are
³³⁰ too short for any reaction to happen in the nucleons. After the interactions ex-
³³¹ cited nucleons are transformed into soft particle production. Production does not
³³² depend on the number of interactions a nucleon has gone through. The average
³³³ number of participants, $\langle N_{part} \rangle$ can also be calculated from the Glauber model

$$\begin{aligned} \langle N_{part}^{AB}(b) \rangle &= \int ds^2 T_A(\bar{s}) \left[1 - \left[1 - \sigma_{NN} \frac{T_B(\bar{s} - \bar{b})}{B} \right]^B \right] \\ &+ \int ds^2 T_B(\bar{s}) \left[1 - \left[1 - \sigma_{NN} \frac{T_A(\bar{s} - \bar{b})}{A} \right]^A \right]. \end{aligned} \quad (10)$$

³³⁴ Glauber calculations require some knowledge of the properties of the nuclei.
³³⁵ One requirement is the nucleon density distribution, which can be experimen-
³³⁶ tally determined by studying the nuclear charge distribution in low-energy elec-
³³⁷ tron scattering experiments [43]. The nucleon density is usually parametrized by
³³⁸ a Woods-Saxon distribution

$$\rho(r) = \frac{\rho_0}{1 + \exp\left(\frac{r-R}{a}\right)}, \quad (11)$$

where ρ_0 is the nucleon density in center of the nucleus, R is the nuclear radius and a parametrizes the depth of the skin. The density stays relatively constant as a function of r until around R where it drops to almost 0 within a distance given by a .

Another observable required in the calculations is the total inelastic nucleon-nucleon cross-section $\sigma_{\text{inel}}^{\text{NN}}$. This can be measured in proton-proton collisions at different energies.

There are two often used approaches to Glauber calculations. The optical approximation is one way to get simple analytical expressions for the nucleus-nucleus interaction cross-section, the number of interacting nucleons and the number of nucleon-nucleon collisions. In the optical Glauber it is assumed that during the crossing of the nuclei the nucleons move independently and they will be essentially undeflected.

With the increase of computational power at hand the Glauber Monte Carlo (GMC) approach has emerged as a method to get a more realistic description of the collisions. In GMC the nucleons are distributed randomly in three-dimensional coordinate system according to the nuclear density distributions. Also nuclear parameters, like the radius R can be sampled from a distribution. A heavy-ion collision is then treated as a series of independent nucleon-nucleon collisions, where in the simplest model nucleons interact if their distance in the plane orthogonal to the beam axis, d , satisfies

$$d < \sqrt{\sigma_{\text{inel}}^{\text{NN}}} \quad (12)$$

The average number of participants and binary collisions can then be determined by simulating many nucleus-nucleus collisions. The results of one GMC Pb-Pb event with impact parameter $b = 9.8$ fm is shown in Fig. 6

1.3.3 Hydrodynamical Modelling

The relativistic version of hydrodynamics has been used to model the deconfined phase of a heavy-ion collision with success. Heavy-ion collisions produce many hadrons going into all directions. It is expected that tools from statistical physics would be applicable to this complexity [48]. The power of relativistic hydrodynamics lies in its simplicity and generality. Hydrodynamics only requires that there is local thermal equilibrium in the system. In order to reach thermal equilibrium the system must be strongly coupled so that the mean free path is shorter than the length scales of interest [49].

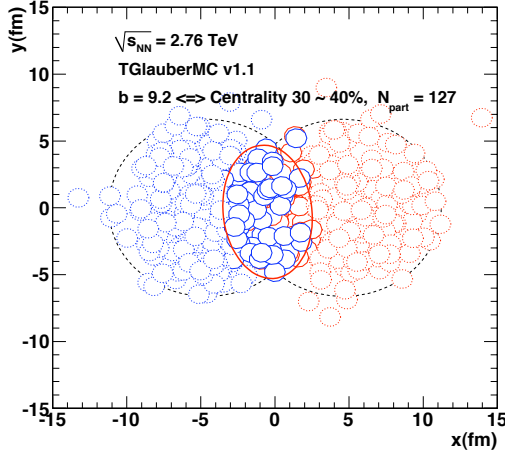


Figure 6: The results of one Glauber Monte Carlo simulation. Big circles with black dotted boundaries represent the two colliding nuclei. The participant zone is highlighted with the solid red line. Small red and blue circles represent nucleons. Circles with thick boundaries are participants i.e. they interact with at least one nucleon from the other nucleus. Small circles with dotted boundaries are spectators which do not take part in the collision.

372 The use of relativistic hydrodynamics in high-energy physics dates back to
 373 Landau [50] and the 1950's, before QCD was discovered. Back then it was used
 374 in proton-proton collisions. Development of hydrodynamics for the use of heavy-
 375 ion physics has been active since the 1980's, including Bjorken's study of boost-
 376 invariant longitudinal expansion and infinite transverse flow [51]. Major steps
 377 were taken later with the inclusion of finite size and and dynamically generated
 378 transverse size [52, 53], a part of which was done at the University of Jyväskylä.
 379 The role of hydrodynamics in heavy-ion physics was strengthened when QGP was
 380 observed to behave like a liquid by RHIC [3].

381 The evolution of a heavy-ion event can be divided into four stages. A schematic
 382 representation of the evolution of the collisions is shown in Fig. 7. Stage 1 follows
 383 immediately the collision. This is known as the pre-equilibrium stage. Hydrody-
 384 namic description is not applicable to this regime because thermal equilibrium is
 385 not yet reached. The length of this stage is not known but it is assumed to last
 386 about $1 \text{ fm}/c$ in proper time τ .

387 The second stage is the regime where thermal equilibrium or at least near-
 388 equilibrium is reached. In this stage hydrodynamics should be applicable if the
 389 temperature is above the deconfinement temperature [49]. This lasts about $5 - 10 \text{ fm}/c$ until the temperature of the system sinks low enough for hadronization to

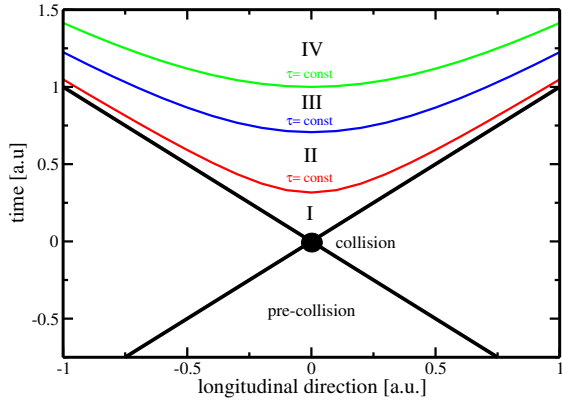


Figure 7: Schematic representation [49] of a heavy-ion collision as the function of time and longitudinal coordinates z . The various stages of the evolution correspond to proper time $\tau = \sqrt{t^2 - z^2}$ which is shown as hyperbolic curves separating the different stages.

391 occur. Now the system loses its deconfined, strongly coupled, state and hydrodynamics
 392 can no longer be used. The third stage is the hadron gas stage where the
 393 hadrons still interact. This ends when hadron scattering becomes rare and they
 394 no longer interact. In the final stage hadrons are free streaming and they fly in
 395 straight lines until they reach the detector.

396 The hydrodynamical approach treats the ensemble of particles as a fluid. It
 397 uses basic equations from hydrodynamics and thermodynamics but with a few
 398 modifications to account for the relativistic energies. The calculation is based
 399 on a collection of differential equations connecting the local thermal variables like
 400 temperature, pressure etc. to local velocities of the fluid. One also needs equations
 401 of state that connect the properties of the matter, e.g. temperature and pressure
 402 to density. Given initial conditions and equations of state the calculation gives the
 403 time-evolution of the system.

404 At first only ideal hydrodynamics was used. Ideal hydrodynamics does not
 405 include viscosity but it is a relatively good approximation and it could predict
 406 phenomena like elliptic flow. For more detailed calculations also viscosity must be
 407 considered and viscosity itself is an interesting property of QGP.

408 1.4 Flow

409 In a heavy-ion collision the bulk particle production is known as flow. The pro-
 410 duction is mainly isotropic but a lot of studies including my thesis focus on the
 411 small anisotropies. After the formation of the QGP, the matter begins to expand
 412 as it is driven outwards by the strong pressure difference between the center of the
 413 collision zone and the vacuum outside the collision volume. The pressure-driven
 414 expansion is transformed into flow of low-momentum particles in the hadroniza-
 415 tion phase. Since the expansion is mainly isotropic the resulting particle flow is
 416 isotropic with small anisotropic corrections that are of the order of 10% at most.
 417 The isotropic part of flow is referred to as radial flow.

418 The transverse momentum spectra dN/dp_T in heavy-ion collisions is shown

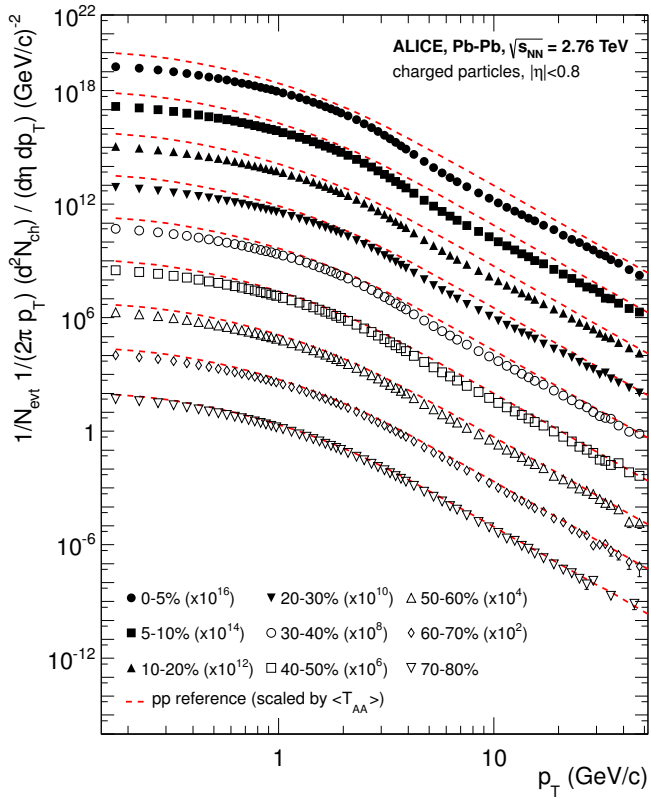


Figure 8: Charged particle spectra measured by ALICE [54] for the 9 centrality classes given in the legend. The distributions are offset by arbitrary factors given in the legend for clarity. The distributions are offset by arbitrary factors given in the legend for clarity. The dashed lines show the proton-proton reference spectra scaled by the nuclear overlap function determined for each centrality class and by the Pb-Pb spectra scaling factors [54].

419 in Fig. 8. The vast majority of produced particles have small p_T . The difference
 420 between the yield of 1 GeV/c and 4 GeV/c particles is already 2-3 orders of mag-
 421 nitude. Any observables that are integrated over p_T are therefore dominated by
 422 the small momentum particles.

423 1.4.1 Anisotropic Flow

424 In a non-central heavy-ion collision the shape of the impact zone is almond-like.
 425 In peripheral collisions the impact parameter is large which means a strongly
 426 asymmetric overlap region. In a central collision the overlap region is almost
 427 symmetric in the transverse plane. In this case the impact parameter is small.
 428 Collisions with different impact parameters are shown in Fig. 4.

429 The pressure gradient is largest in-plane, in the direction of the impact pa-
 430 rameter b , where the distance from high pressure, at the collision center, to low
 431 pressure, outside the overlap zone, is smallest. This leads to stronger collective
 432 flow into in-plane direction, which in turn results in enhanced thermal emission
 433 through a larger effective temperature into this direction, as compared to out-of-
 434 plane [5, 6, 55]. The resulting flow is illustrated in Fig. 9. Flow with two maxima
 435 in the direction of the reaction plane is called elliptic flow. This is the dominant

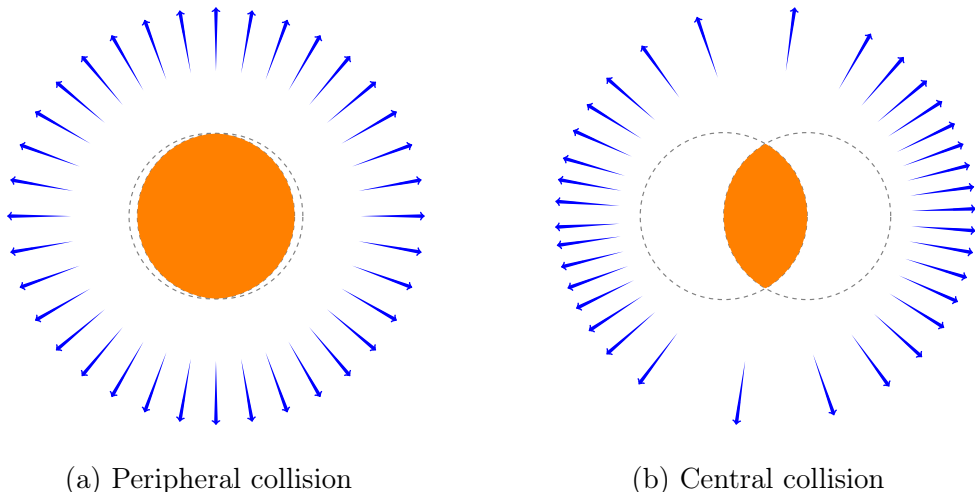


Figure 9: Illustration of flow in momentum space in central and peripheral collisions. The density of the arrows represent the magnitude of flow seen at a large distance from the collision in the corresponding azimuthal direction. In a peripheral collision momentum flow into in-plane direction is strong and flow into out-of-plane direction is weak. In a central collision anisotropy in flow is smaller, but the total yield of particles is larger.

436 part of anisotropic flow. Also more complex flow patterns can be identified. The
437 most notable of these is the triangular flow, which is mainly due to fluctuations in
438 the initial conditions.

439 Flow is nowadays usually quantified in the form of a Fourier composition

$$E \frac{d^3N}{dp^3} = \frac{1}{2\pi p_T} \frac{d^2N}{dp_T d\eta} \left(1 + \sum_{n=1}^{\infty} 2v_n(p_T, \eta) \cos(n(\phi - \Psi_n)) \right), \quad (13)$$

440 where the coefficients v_n give the relative strengths of different anisotropic flow
441 components and the overall normalisation gives the strength of radial flow. Elliptic
442 flow is represented by v_2 and v_3 represents triangular flow. The first coefficient,
443 v_1 , is connected to directed flow. This will however in total be zero because of
444 momentum conservation. It can be nonzero in some rapidity or momentum regions
445 but it must be canceled by other regions.

446 The first approaches to quantifying the anisotropy of flow did not use the
447 Fourier composition. Instead they approached the problem with a classic event
448 shape analysis using directivity [56] or sphericity [5, 57] to quantify the flow.

449 The first experimental studies of anisotropy were performed at the AGS [58]
450 in 1993. They noted that the anisotropy of particle production in one region
451 correlates with the reaction plane angle defined in another region.

452 The first ones to present the Fourier decomposition were Voloshin and Zhang in
453 1996 [59]. This new approach was useful for detecting different types of anisotropy
454 in flow, since the different Fourier coefficients give different harmonics in flow.
455 They also show the relative magnitude of each harmonic compared to radial flow.

456 Some parts of the Fourier composition approach were used for Au-Au collisions
457 at $\sqrt{s_{NN}} = 11.4\text{GeV}$ at AGS in 1994 [60]. This analysis still focused on event
458 shapes but they constructed these shapes using Fourier composition from different
459 rapidity windows.

460 Add a paragraph on the lessons learned from flow studies.

461 1.5 Hard processes

462 1.5.1 pQCD factorization

463 The term Hard Scattering is used in connection with the scattering of two point-
464 like constituents (partons) of colliding nucleons, when the momentum transfer Q^2
465 is large ($Q \gg \Lambda_{\text{QCD}}$). Figure 11 shows the incoming partons, quarks or gluons, as
466 they exchange a space-like virtual gluon and produce two highly virtual outgoing
467 partons. The outgoing partons will eventually fragment into collimated showers of
468 partons, referred to as jets

469 Jet fragmentation can be factorised into three components; the parton distribu-
470 tion functions f_a, f_b that give the probability of getting a parton with momentum

$$\begin{aligned}
q q' &\rightarrow q q' & \frac{4}{9} \frac{\hat{s}^2 + \hat{u}^2}{\hat{t}^2} \\
\bar{q} q' &\rightarrow \bar{q} q' & \\
q q &\rightarrow q q & \frac{4}{9} \left(\frac{\hat{s}^2 + \hat{u}^2}{\hat{t}^2} + \frac{\hat{s}^2 + \hat{u}^2}{\hat{t}^2} \right) - \frac{8}{27} \frac{\hat{s}^2}{\hat{u} \hat{t}} \\
\bar{q} q &\rightarrow \bar{q}' q' & \frac{4}{9} \frac{\hat{t}^2 + \hat{u}^2}{\hat{s}^2} \\
\bar{q} q &\rightarrow \bar{q} q & \frac{4}{9} \left(\frac{\hat{s}^2 + \hat{u}^2}{\hat{t}^2} + \frac{\hat{t}^2 + \hat{u}^2}{\hat{s}^2} \right) - \frac{8}{27} \frac{\hat{u}^2}{\hat{s} \hat{t}} \\
\bar{q} q &\rightarrow g g & \frac{32}{27} \frac{\hat{u}^2 + \hat{t}^2}{\hat{u} \hat{t}} - \frac{8}{3} \frac{\hat{u}^2 + \hat{t}^2}{\hat{s}^2} \\
g g &\rightarrow \bar{q} q & \frac{1}{6} \frac{\hat{u}^2 + \hat{t}^2}{\hat{u} \hat{t}} - \frac{3}{8} \frac{\hat{u}^2 + \hat{t}^2}{\hat{s}^2} \\
q g &\rightarrow q g & \frac{4}{9} \frac{\hat{u}^2 + \hat{s}^2}{\hat{u} \hat{s}} + \frac{\hat{u}^2 + \hat{s}^2}{\hat{t}^2} \\
g g &\rightarrow g g & \frac{9}{2} \left(3 - \frac{\hat{u} \hat{t}}{\hat{s}^2} - \frac{\hat{u} \hat{s}}{\hat{t}^2} - \frac{\hat{s} \hat{t}}{\hat{u}^2} \right)
\end{aligned}$$

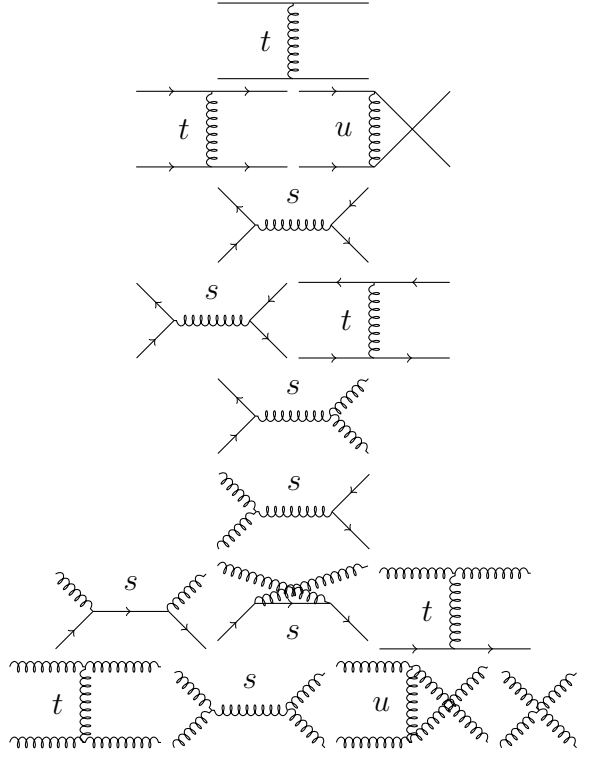


Figure 10: The basic pQCD processes and their quadratic matrix elements

⁴⁷¹ fraction x of the proton, the cross section of the elementary scattering $ab \rightarrow cd$
⁴⁷² (Fig. 10) and the fragmentation functions that give the probability of getting
⁴⁷³ hadron h from the parton.

$$\frac{d\sigma_{pp}^h}{dy d^2 p_T} = K \sum_{abcd} \int dx_a dx_b f_a(x_a, Q^2) f_b(x_b, Q^2) \frac{d\sigma}{dt} (ab \rightarrow cd) \frac{D_{h/c}^0}{\pi z_c}, \quad (14)$$

⁴⁷⁴ where

$$x_{a,b} = \frac{|p_{a,b}|}{|p_{proton}|}.$$

⁴⁷⁵ Parton Distribution Function

⁴⁷⁶ Parton Distribution Functions (PDFs) are essential to calculate the scattering cross
⁴⁷⁷ section. They are extracted from comprehensive global analysis of experimental
⁴⁷⁸ results from a variety of fixed-target and collider experiments. PDFs $f_a(x)$ give the

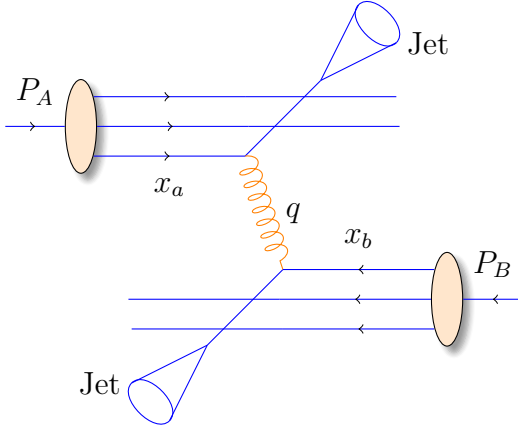


Figure 11: Schematic view of hard scattering process of $p + p \rightarrow 2 \text{ jets}$

479 differential probability for parton a to carry momentum fraction x of the proton
480 momentum.

481 As the PDFs cannot be calculated from first principles. In practice the PDFs
482 are measured in Deeply Inelastic Scattering (DIS) experiments and are extrapolated
483 to the relevant momentum scales at LHC using the Dokshitzer-Gribov-Lipatov-
484 Altarelli-Parisi (DGLAP) evolution scheme [61–63]

$$\mu_F^2 \frac{\partial f_i(x, \mu_F^2)}{\partial \mu_F^2} = \sum_j \frac{\alpha_s(\mu_F)}{2\pi i} \int_x^1 \frac{dz}{z} P_{ij}(z) f_j\left(\frac{x}{z}, \mu_F^2\right), \quad (15)$$

485 where μ_F is a factorization scale. The splitting functions P_{ij} describe a probability
486 to radiate parton i from parton j as a function of the momentum fraction z carried
487 away by the offspring parton.

488 Fragmentation functions

489 The final component in the factorization, fragmentation functions, describe the
490 distribution of the fractional momenta of particles radiated from the outgoing
491 parton. Fragmentation function are given with respect to the momentum fraction
492 z which is defined as the longitudinal momentum fraction of jet momentum p_{jet}
493 carried away by the jet fragment p_{part}

$$z = \frac{\bar{p}_{\text{part}} \cdot \bar{p}_{\text{jet}}}{p_{\text{jet}}^2} = \frac{p_{\text{part}}}{p_{\text{jet}}} \Big|_{\bar{p}_{\text{part}} \times \bar{p}_{\text{jet}} = 0} \quad (16)$$

494 Fragmentation function $D(z)$ then gives the average multiplicity m of jet frag-
495 ments having $z > z_0$ [1].

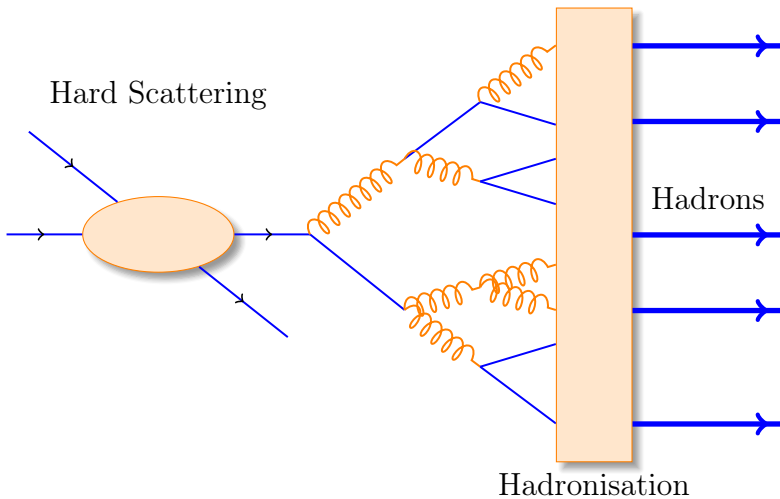


Figure 12: An illustration of jet showering. The highly virtual parton from the hard scattering will produce a shower of softer partons. When the virtuality is low enough the shower will go through a hadronisation process that produces the hadrons, which will be eventually observed in the detector.

$$m(z_0) = \int_{z_0}^1 D(z) dz \Rightarrow m(0) \equiv \langle m \rangle = \int_0^1 D(z) dz \quad (17)$$

496 Because of momentum conservation the sum of all jet fragments must be equal
497 to the jet momentum, i.e.

$$\sum p_{i,\text{part}} = p_{\text{jet}} \Rightarrow \sum z_i = 1 \Rightarrow \int_0^1 z D(z) dz = 1 \quad (18)$$

498 A natural consequence is that the average momentum fraction is the inverse of
499 the average multiplicity

$$\langle z \rangle = \frac{\int_0^1 z D(z) dz}{\int_0^1 D(z) dz} = \frac{1}{\langle m \rangle}. \quad (19)$$

500 1.5.2 Jet hadronisation

501 When the parton shower reaches a scale close to Λ_{QCD} , the perturbative descrip-
502 tion is no longer valid. Thus the hadronisation stage must be described in a
503 non-perturbative manner. One simple scenario that is used in several theory calcu-
504 lations is the so-called local parton-hadron duality [64]. In the local parton-hadron
505 duality hypothesis it is assumed that there exists a low virtuality scale Q_0 in which

506 the hadronisation happens, that is independent of the scale of the primary hard
 507 process. At this scale the partons are transformed into hadrons, assuming that the
 508 flow of momentum and quantum numbers for the hadrons can be directly obtained
 509 from those of partons introducing only small normalising constants.

510 Lund string model

511 One common implementation in MC generators is the Lund string fragmentation
 512 algorithm [65]. The string model is based on the fact that in QCD linear confine-
 513 ment is expected over large distances [66]. This can be modelled by imagining a
 514 colour flux tube being stretched between the outgoing partons. The left side of
 515 Fig. 13 illustrates this point for a $q\bar{q}$ -pair. The tube is assumed to have a uniform
 516 fixed transverse size of about 1 fm along its length, which leads to a linearly rising
 517 potential $V(r) = \kappa r$, where the string constant κ describes the amount of energy
 518 per unit length. A value of $\kappa \approx 1 \text{ GeV/fm} \approx 0.2 \text{ GeV}^2$ can be obtained from hadron
 519 mass spectroscopy.

520 The evolution of string fragmentation is illustrated schematically on the right
 521 side of Fig. 13. This figure is drawn in a light cone presentation, so the initial
 522 quark and antiquark are going to separate directions at the speed of light, which
 523 assumes them as massless. The string between them, illustrated in the figure by
 524 the red line, stretches until its potential energy becomes high enough that it can
 525 break, forming a new quark-antiquark pair. If the original pair was $q\bar{q}$ and the
 526 new pair $q'\bar{q}'$, now two new pairs $q\bar{q}'$ and $q'\bar{q}$ have formed. As these particles
 527 are also moving away from each other, the strings between them can stretch and
 528 break, creating yet more pairs. The process continues until the invariant mass of
 529 the system connected by the string becomes small enough and a final state meson
 530 is formed.

531 To mathematically model the string one can use a massless relativistic string
 532 with no transverse degrees of freedom. The gluons are represented as energy and
 533 momentum carrying kinks on the string with incoherent sums of one colour charge
 534 and one anticolour charge. When this string breaks, it is classically required that
 535 the created quark and antiquark are produced at a certain distance if they are to
 536 have any mass or transverse momentum. However, taking into account quantum
 537 mechanics, the pair must be created at one point and then tunnel out to the
 538 classically allowed region. Thus the probability to create a new quark-antiquark
 539 pair becomes proportional to the tunnelling probability [65].

$$P_{\text{tunnelling}} \propto \exp\left(\frac{-\pi m_\perp^2}{\kappa}\right) = \exp\left(\frac{-\pi m^2}{\kappa}\right)\left(\frac{-\pi p_\perp^2}{\kappa}\right), \quad (20)$$

540 where the transverse mass m_\perp is defined as $m_\perp^2 = m^2 + p_\perp^2$. The transverse
 541 momentum is now defined to be transverse to the string axis. This formula gives

542 flavour-independent Gaussian p_\perp -distribution for the created $q\bar{q}$ pairs.

543 As explained above the string fragmentation would only produce mesons in
544 the final state, but we know that also baryons are created in the process. In the
545 string fragmentation model baryon production is included by adding a probability
546 that a diquark-antidiquark pair is created instead of a quark-antiquark pair when
547 a string breaks.

548 The kinematics of each string breaking are determined iteratively. Since there
549 is no natural ordering, the string breaking can be considered in any order and
550 the answer obtained must be the same. One can start from the q leg and work
551 one's way to the \bar{q} leg, or vice versa. This give a left-right symmetry of the
552 string fragmentation. In the Lund model this is taken into account by defining a
553 symmetric fragmentation function

$$f(z) \propto \frac{1}{z} (1-z)^a \exp\left(-\frac{bm_\perp^2}{z}\right) \quad (21)$$

554 to break the string into a hadron and a remainder system. Here z is the fraction
555 of light-cone momentum p^+ given to the hadron in the string breaking, m_\perp is the
556 transverse mass of the hadron and a and b are tunable parameters of the model.
557 For heavy quarks this has to be modified as

$$f(z) \propto \frac{1}{z^{1+bm_Q^2}} (1-z)^a \exp\left(-\frac{bm_\perp^2}{z}\right) \quad (22)$$

558 The process can be thought as follows: first start from the q -leg of a $q\bar{q}$ system
559 and choose to consider the breaking to new $q'\bar{q}'$ pair closest to this leg. Now the
560 breaking will produce a hadron $q\bar{q}'$ and a remainder system spanning from $q'\bar{q}$.
561 Then the process is continued until the \bar{q} -leg is reached. A small detail here is
562 that in equation (21) it is assumed that the mass of the remainder system is large.
563 Thus some patching up is needed for the last two hadrons coming from a string.
564 The patching up is done such that the place where it happens looks as closely like
565 any other string break as possible.

566 One additional possibility one must consider is that a string can have such a
567 low mass that it cannot break at all. In this case a single hadron is generated out
568 of the string and if necessary energy and momentum are exchanged with other
569 partons in the event.

570 After all the hadrons are produced, the short-lived ones can still decay before
571 the set of final state particles in the simulation is obtained []

572 Cluster model

573 Instead of a string model HERWIG [] uses a cluster model [67] for hadronisation.
574 The advantage of cluster models is that they require a smaller number of param-

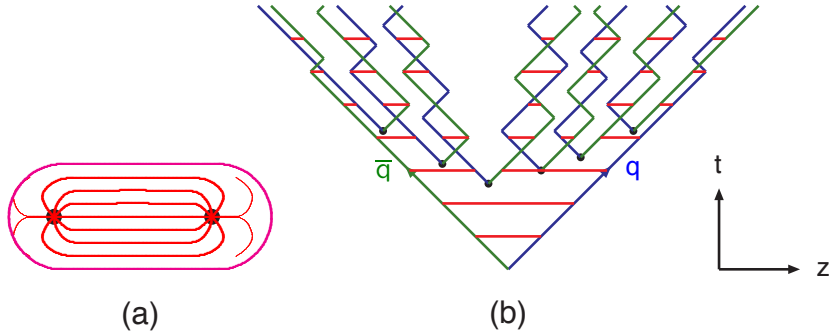


Figure 13: (a) A flux tube spanned between a quark and an antiquark. (b) The motion and breakup of a string system, with the two transverse degrees of freedom suppressed (diagonal lines are (anti)quarks, horizontal ones snapshots of the string field). [66]

eters than string models. The model is based on the preconfinement property of parton showers, i.e. the colour structure of the shower at any evolution scale Q_0 is such that colour singlet combinations of partons can be formed with an asymptotically universal invariant mass distribution. The invariant mass does not depend on the initial hard process scale Q , but only on Q_0 and the QCD scale Λ_{QCD} , when $Q \gg Q_0$.

The cluster model starts from transforming all gluons non-perturbatively into $q\bar{q}$ pairs, which requires that the gluons get a mass, which must be at least twice the lightest quark mass. After the gluons are transformed into quarks, the adjacent colour lines can be clustered together to colour singlet states with mesonic quantum numbers. The momentum of these clusters is defined to be the sum of the momenta of the clustering partons. According to preconfinement, the mass distribution of these clusters is independent of the details of the hard scattering. Additionally the clusters can be regarded as highly excited hadron resonances and decayed into the final state hadrons.

Some of these initial clusters are too heavy to reasonably describe an excited state of a hadron. These must be split before they are allowed to decay. The cluster C is split if its mass fulfills the condition []

$$M_C^p \geq M_{\max}^p + (m_1 + m_2)^p, \quad (23)$$

where $m_{1,2}$ are the masses of the constituents partons of the cluster and M_{\max} and p are the main parameters of the model. These have to be chosen separately for clusters containing light, charmed and bottom quarks. When a cluster is split, a pair of light quarks is generated from the vacuum and two new clusters are made, both containing one quark from the original cluster and one from the newly gen-

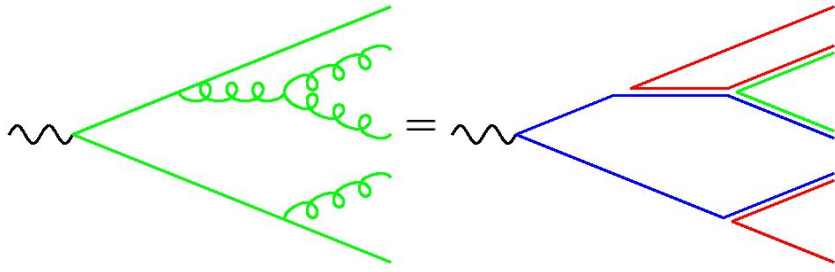


Figure 14: Colour structure of a parton shower to leading order in N_c . [66]

erated pair. The splitting is continued until no clusters with masses M_C fulfilling the equation 23 remains.

When the clusters are light enough, they decay into final state hadrons. If the mass of the cluster is high enough for decaying into a baryon-antibaryon pair, there is a parameter deciding whether the cluster undergoes mesonic or baryonic decay. For a mesonic decay a quark-antiquark pair is created from the vacuum and for the baryonic decay a diquark-antidiquark pair is made. Then the exact decay products are chosen and the cluster decays isotropically in the rest frame of the cluster. If there are partons produced in the perturbative phase involved in the decay, they retain their original direction in the cluster rest frame, up to some Gaussian smearing. If the cluster mass is too low to decay into a pair of mesons, it decays into the lightest possible hadron and some energy and momentum is exchanged with the adjacent clusters. At the end we are left with the final state hadrons, some of which might still decay until the end of the simulation if they are very short-lived. []

1.5.3 Jet energy loss

Discovery of jet quenching via leading hadron suppression

First evidence of jet quenching comes from observing high p_T tracks, i.e. the leading hadrons.

Jet quenching in heavy-ion collisions is usually quantized with the nuclear modification factor R_{AA} , which is defined as

$$R_{AA}(p_T) = \frac{(1/N_{AA}^{evt}) dN^{AA}/dp_T}{\langle N_{coll} \rangle (1/N_{pp}^{evt}) dN^{pp}/dp_T} \quad (24)$$

where dN^{AA}/dp_T and dN^{pp}/dp_T are the yields in heavy-ion and proton-proton collisions, respectively and $\langle N_{coll} \rangle$ is the average number of binary nucleon-nucleon collisions in one heavy-ion event. The number of binary collisions can be calculated from the Glauber model as shown in Sec. 1.3.2. From the point of view of direct

623 production a heavy-ion collision can be estimated relatively well to be only a series
 624 of proton-proton collisions.

625 If the medium has no effect on high p_T particles the nuclear modification factor
 626 should be 1. At RHIC and LHC this has been observed to be as low as 0.2 because
 627 of jet quenching. Measurements of R_{AA} from different sources are shown in Fig. 15

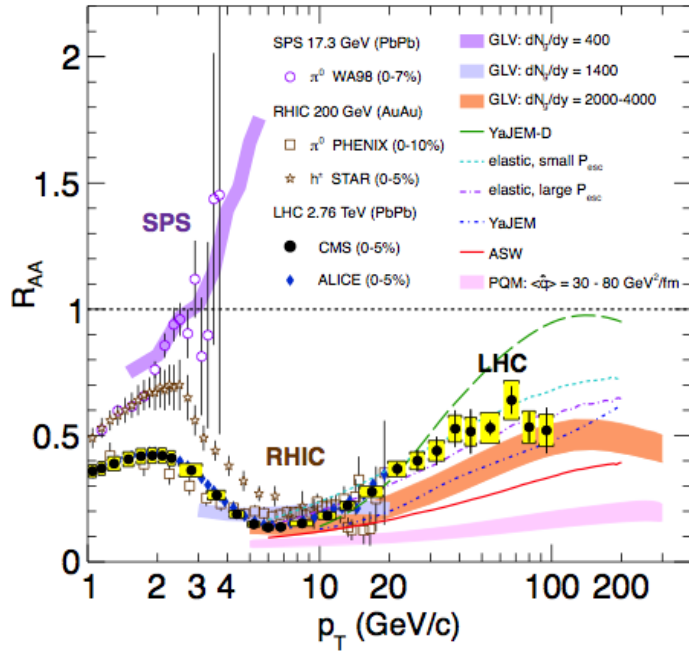


Figure 15: Measurements of the nuclear modification factor R_{AA} in central heavy-ion collisions at three different center-of-mass energies, as a function of p_T , for neutral pions (π^0), charged hadrons (h^\pm), and charged particles [68–72], compared to several theoretical predictions [34, 73–77]. The error bars on the points are the statistical uncertainties, and the yellow boxes around the CMS points are the systematic uncertainties. The bands for several of the theoretical calculations represent their uncertainties [78].

628 The nuclear modification factor can also be used to quantify anisotropy. In
 629 the study of anisotropy R_{AA} in-plane and out-of-plane can be compared. The
 630 distance traveled through medium is largest out-of-plane which leads to stronger
 631 suppression in this direction. The nuclear modification factor as a function of
 632 $\Delta\phi = \phi - \psi_n$ is given by

$$\begin{aligned}
R_{AA}(\Delta\phi, p_T) &= \frac{(1/N_{AA}^{evt}) d^2 N^{AA} / d\Delta\phi dp_T}{\langle N_{coll} \rangle (1/N_{pp}^{evt}) dN^{pp} / dp_T} \approx \frac{dN^{AA} / dp_T (1 + 2 \cdot v_2 \cos(2\Delta\phi))}{\langle N_{coll} \rangle dN^{pp} / dp_T} \\
&= R_{AA}^{incl}(p_T) (1 + 2 \cdot v_2 \cos(2\Delta\phi)). \tag{25}
\end{aligned}$$

633 The yield of proton-proton collisions is independent of the reaction plane and
634 the yield in heavy-ion collisions is modulated by the second harmonics. In Eq. (25)
635 R_{AA} is approximated only up to the second harmonics. From Eq. (25) it follows
636 that

$$\frac{R_{AA}(0, p_T) - R_{AA}(\pi/2, p_T)}{R_{AA}^{incl}(p_T)} \approx \frac{R_{AA}^{incl}(p_T) (1 + 2 \cdot v_2 - (1 - 2 \cdot v_2))}{R_{AA}^{incl}(p_T)} = 4 \cdot v_2 \tag{26}$$

637 The observed $R_{AA}(\Delta\phi, p_T)$ from PHENIX measurements in Au-Au collisions at
638 $\sqrt{s} = 200\text{GeV}$ [79] is compared to R_{AA} using v_2 via Eq. (25) in Fig. 16. They
639 agree very well within the statistical errors for all centrality and p_T bins.

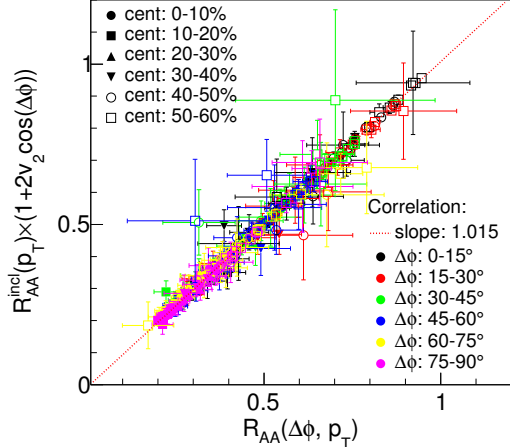


Figure 16: A comparison between observed $R_{AA}(\Delta\phi, p_T)$ and R_{AA} using v_2 from PHENIX measurements of Au-Au collisions at $\sqrt{s} = 200\text{GeV}$. On the X-axis is the measured $R_{AA}(\Delta\phi, p_T)$. On the y-axis is the inclusive R_{AA} multiplied by $1 + 2v_2 \cos(\Delta\phi)$ [79].

639 At high- p_T , the pQCD processes are dominant, hence the v_n (or $R_{AA}(\Delta\phi, p_T)$)
640 characterize the pathlength-dependence of the energy loss process.
641

Jet quenching is not the only high p_T phenomenon studied in heavy-ion collisions. Another property is jet fragmentation. The high momentum parton created in the initial collision fragments into a number of partons with smaller p_T . Jet fragmentation occurs also in proton-proton collisions in the vacuum, but it can be modified due to the presence of the medium. In order to study the jet fragmentation function ($D(z)$, where $z = p_T^h/p_T^{part}$) modification due the medium, we use the two-particle correlations. The particle yield can be extracted from the correlation function. The background from the flow processes is correlated and needs to be subtracted to get the particle yield associated only with the jet. The ratio of the jet yields in Au-Au and p-p collision $I_{AA} = Y^{Au+Au}/Y^{p+p}$ characterizes the jet fragmentation modification [80]. I_{AA} probes the interplay between the parton production spectrum, the relative importance of quark-quark, gluon-gluon and quark-gluon final states, and energy loss in the medium.

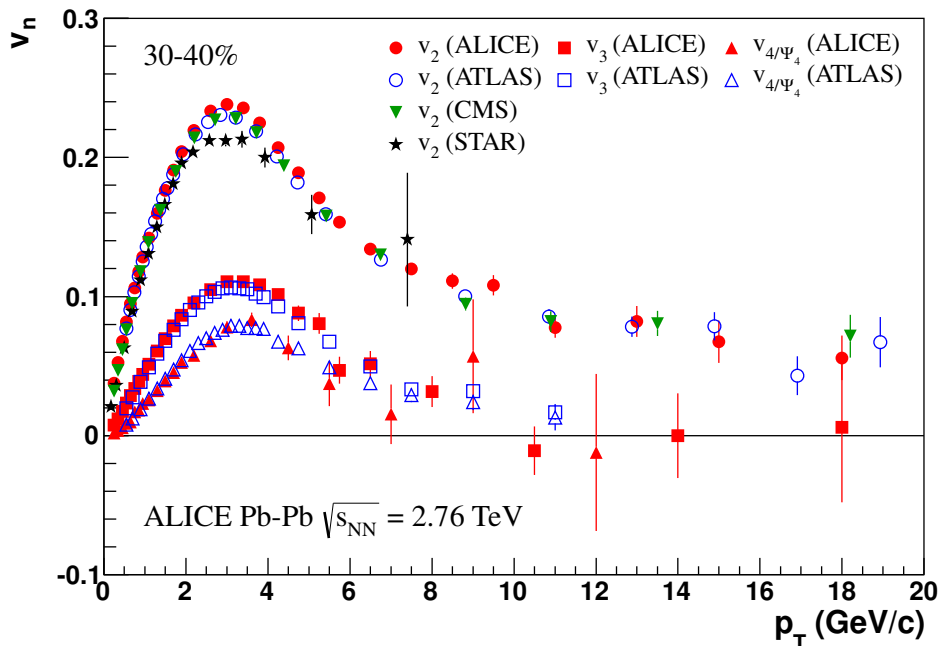


Figure 17

655 Theory of jet quenching

High momentum particles are very rare and they are only produced in the initial collisions. After they are created they escape the medium before a thermal equilibrium is reached. Thus they are not part of the pressure-driven collective expansion. Instead high momentum yield is suppressed because of energy loss in

the medium. When propagating through the medium these partons lose energy as they pass through the medium. This is referred to as jet quenching. Jet quenching depends on the path lengths through the medium. Thus anisotropy in this region is mainly dependent on the collision geometry and density of medium.

The energy loss of partons in medium is mainly due to QCD bremsstrahlung and to elastic scatterings between the parton and the medium.

The radiative energy loss mechanism is given in terms of the transport coefficient $\langle \hat{q} \rangle$, which describes the average momentum transfer between the medium and parton [81]. The exact definition of this depends on the theoretical formalism used to describe the energy loss mechanism.

Many of the energy loss models exploit the analogy between the QCD interaction of parton propagating through the colored medium and the QED energy loss of electron propagating through material. An electron propagating through matter loses its energy by photon Bremsstrahlung radiation. In the simplest case, each individual scattering center results in a single emission of a photon. This is known as the Bethe-Heitler regime [82]. The energy spectrum of radiated photons dN/dE is, in this case, proportional to $1/E$. However, the Bremsstrahlung photon, can be radiated only when the distance between the scattering centers is larger than the formation length. In the limit, when the scattering centers are closer than the formation length, the Bremsstrahlung process is suppressed. This phenomenon is known as the Landau-Pomeranchuk-Migdal (LPM) [83, 84] suppression. The radiated spectrum in this regime is proportional to $1/\sqrt{E}$.

Lower energy photons are further suppressed by the destructive interference leading to the suppression of Bremsstrahlung photons of $E < \gamma\omega_p$, where ω_p is the plasma frequency of the radiator. This is known as Dielectric suppression. The photon energy distribution in this regime is proportional to the energy of the photon. A schematic view of the effect of these three regimes is shown in Fig. 18.

The simplest energy loss process is elastic QCD scattering off the medium partons. In elastic scatterings the recoil energy of the scattered partons are absorbed by the thermal medium, which reduces the energy of the initial parton. The mean energy loss from elastic scatterings can be estimated by

$$\langle \Delta E \rangle_{\text{el}} = \sigma \rho L \langle E \rangle_{\text{1scatt}} \propto L, \quad (27)$$

where σ is the interaction cross section and $\langle E \rangle_{\text{1scatt}}$ is the mean energy transfer of one individual scattering [86]. This assumption holds if the mean energy is independent of the total energy of the parton (E). The transport coefficient of elastic scattering, $\langle \hat{q}_{\text{el}} \rangle = \langle \Delta E \rangle / L$, is defined as the mean energy loss per unit path length.

Another energy loss mechanism is medium-induced radiation. In QCD this radiation is mainly due to the elementary splitting processes, $q \rightarrow qg_r$ and $g \rightarrow gg_r$.

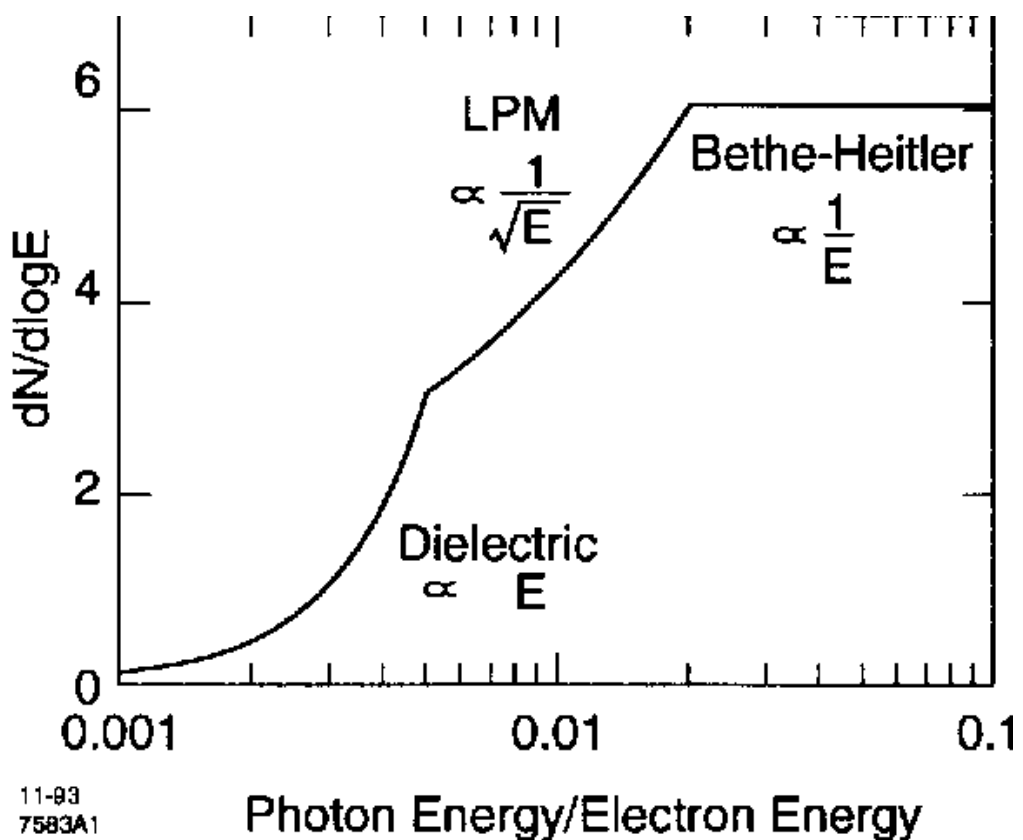


Figure 18: The expected bremsstrahlung spectrum for a electron propagating through material. [85].

698 Assuming that the parton is moving with the speed of light radiation energy loss
699 can be estimated by

$$\langle \Delta E \rangle_{rad} \propto T^3 L^2, \quad (28)$$

700 where L is the length of the medium and T is its temperature [87]. The differ-
701 ent exponents of L in equations 27 and 28 indicate that radiative energy loss is
702 dominant over elastic energy loss.

703 There are several models that attempt to describe the nature of the energy loss
704 mechanism. The most used models can be divided into four formalisms.

705 In the Gyulassy-Levai-Vitev (GLV) [88] opacity expansion model the radiative
706 energy loss is considered on a few scattering centers N_{scatt} . The radiated gluon
707 is constructed by pQCD calculation as summing up the relevant scattering am-
708 plitudes in terms of the number of scatterings. Another approach into opacity
709 expansion is the ASW model by Armesto, Salgado and Wiedermann [89].

710 Thermal effective theory formulation by Arnold, Moore and Yaffe (AMY) [90]
711 uses dynamical scattering centers. It is based on leading order pQCD hard thermal
712 loop effective field theory. This model assumes that because of the high temper-
713 ature of the plasma the strong coupling constant can be treated as small. The
714 parton propagating through the medium will lose energy from soft scatterings and
715 hard scatterings.

716 The above models calculate the energy loss while the parton propagates through
717 the medium, focusing on the pQCD part. The higher twist (HT) approach by Wang
718 and Guo [91] implements the energy loss mechanism in the energy scale evolution
719 of the fragmentation functions.

720 The last category is formed by the Monte Carlo methods. The PYTHIA event
721 generator [92] is widely used in high-energy particle physics. Two Monte Carlo
722 models based on PYTHIA describing the energy loss mechanism are PYQUEN [93]
723 and Q-Pythia [94]. Other Monte Carlo models include JEWEL [95] and Ya-
724 JEM [96].

725 1.5.4 New paradigm of jet Quenching

726 As described in the previous section there have been many experimental evi-
727 dences of jet energy loss, such as the suppression of inclusive hadron spectra at
728 high transverse momentum [97–101], the modification of back-to-back hadron-
729 hadron [80, 102] and direct photon-jet correlations [103], and the modification of
730 reconstructed jet spectra [104] and jet substructure [105–107], as compared to the
731 expectations from elementary proton-proton collisions.

732 The first indications of jet quenching, such as R_{AA} , looked essentially at the
733 leading hadrons of jets, the hard part, ignoring the soft scale part of jet phenomena.

⁷³⁴ However, experimental methods have since improved; jet reconstruction algorithms
⁷³⁵ have become reliable in the LHC era. Instead of the leading hadron we can study
⁷³⁶ the entire jet shower.

⁷³⁷ -Jet RAA -Jetscape

⁷³⁸ Thus the new paradigm in jet quenching in heavy-ion collisions involves multi-
⁷³⁹ scale problems [108, 109]. The elementary scattering and the subsequent branching
⁷⁴⁰ process down to non-perturbative scales are dominated by hard scales in the vac-
⁷⁴¹ uum as well as in the medium. Soft scales, of the order of the temperature of
⁷⁴² the medium, characterise the interactions of soft partons produced in the shower
⁷⁴³ with the QGP. Soft scales also rule hadronisation, which is expected to take place
⁷⁴⁴ in vacuum for sufficiently energetic probes, even though some modifications can
⁷⁴⁵ persist from modifications of color flow [110–112]. Understanding the contribu-
⁷⁴⁶ tions from the different processes to the jet shower evolution in medium and their
⁷⁴⁷ scale dependence is crucial to constrain the dynamics of jet energy loss in the
⁷⁴⁸ expanding medium, the role of colour coherence [113], and fundamental medium
⁷⁴⁹ properties like temperature dependent transport coefficient [114, 115].

⁷⁵⁰ **Lund diagram**

⁷⁵¹ The different momentum and angular scales are subject to different physical phe-
⁷⁵² nomena. Figure 19 shows the relevant medium modification phenomena for differ-
⁷⁵³ ent regions of the phase space at time t , when a jet propagates through a thermal
⁷⁵⁴ cloud of temperature T . As in practice jets propagate over a finite path-length
⁷⁵⁵ L in QCD matter, Fig. 19 can be taken as a representation of the distribution of
⁷⁵⁶ partonic jet fragments at moment $t \approx L$, when the jet escapes the medium.

⁷⁵⁷ The region marked as DGLAP is dominated by the primary vacuum splittings.
⁷⁵⁸ This region is determined by $\theta > \theta_{\text{vac}}$ with

$$\theta_{\text{vac}} \propto 1/\sqrt{pt}. \quad (29)$$

⁷⁵⁹ Medium-induced parton branching fills the log p -log- θ -plane from the bottom
⁷⁶⁰ up (in p) and from the inside out (in θ). This is because transverse momentum is
⁷⁶¹ acquired by Brownian motion in the medium, $k_{\perp}^2 \propto \hat{q}t$. Then the formation time
⁷⁶² constraint $t \geq p/k_{\perp}^2 \approx p/\hat{q}t$ implies that medium-induced quanta can be formed in
⁷⁶³ the region $p \leq k_{\text{form}}$ where

$$k_{\text{form}}(t) = \hat{q}t^2$$

⁷⁶⁴ .

⁷⁶⁵ The probability of finding a splittee with a momentum p with $p < k_{\text{form}}$ is

$$\frac{dP_{\text{find}}(t)}{d \log p} \propto \alpha_s t/t_{\text{form}}(p) \propto \alpha_s \hat{q}^{nicefrac{1}{2}} p^{-1/2} t \quad (30)$$

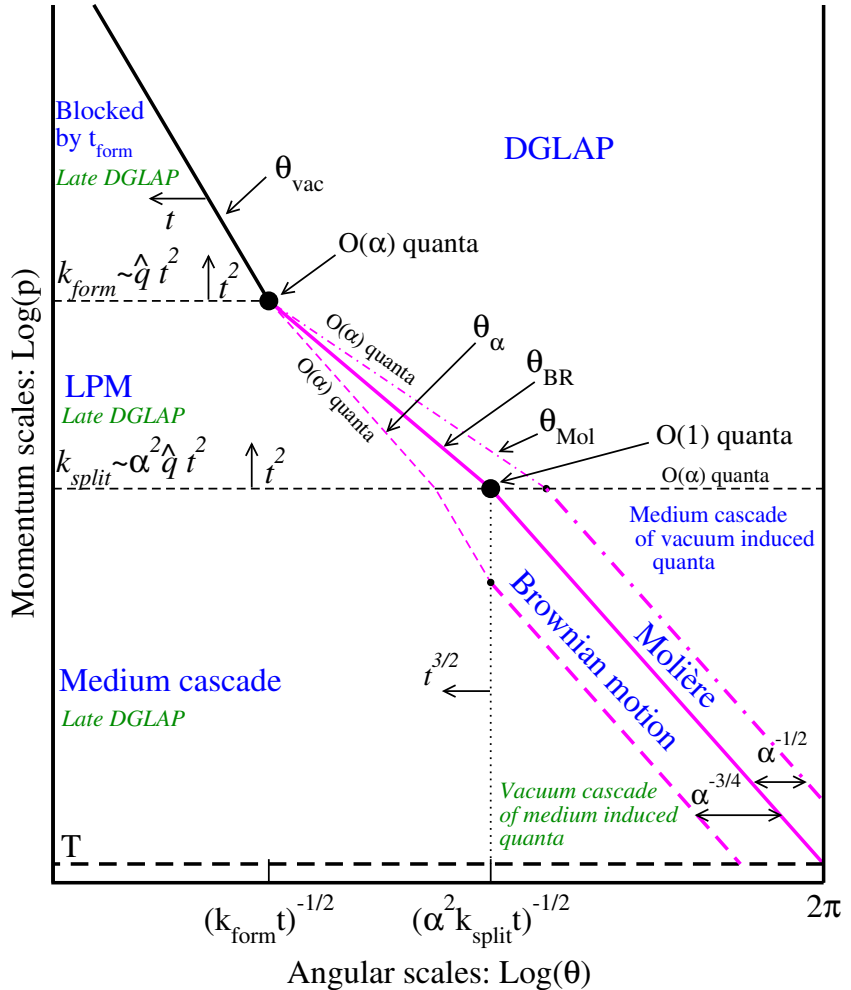


Figure 19: Parametrically accurate picture of how a medium-modified parton cascade fills the phase space. At time t , quanta can be formed up to momentum scale k_{form} and they are formed with $O(1)$ probability per $\log p$ at lower scale k_{split} . Quanta below k_{split} split further and their energy cascades to the thermal scale T in less than an epoch t . Transverse Brownian motion moves quanta up to the angle $\theta_{\text{BR}}(p)$ denoted by the thick purple line. The Molière region at larger θ is dominated by rare large angle scattering. At even larger angle, there are $O(\alpha_s)$ quanta per double logarithmic phase space from DGLAP ‘vacuum’ radiation, and for momenta below k_{split} these cascade within time t to T . After the jet escapes the medium, the jet and the emitted fragments will undergo vacuum radiation. This late time vacuum radiation emitted by the original parton dominates at sufficiently small $\log \theta$ (regions marked “late DGLAP” and bounded by θ_{vac} and θ_α), whereas the late time radiation of the fragments dominates in the region denoted by “Vacuum cascade of the medium induced quanta”. [108].

Not all quanta will stay where they were created. Those modes that have time to lose a significant fraction of their energy will cascade to a significantly lower scale p . For LPM-type radiation, the splitting that degrades energy the most is the hardest splitting.

The $\log p$ distribution has the same $\frac{1}{\sqrt{p}}$ dependence as in the LPM region

$$\frac{dn}{d \log p} = \frac{1}{p} \frac{d\epsilon}{d \log p} \approx \alpha_s \frac{\sqrt{\hat{q}t}}{\sqrt{p}} \quad (31)$$

Also the quanta originating from the DGLAP region will undergo medium interactions that will make the quanta radiate and split. The distribution of radiation is the same as from any other mode. Above a certain momentum scale k_{split} the distribution of originating daughters is

$$\frac{dP_{\text{find}}}{d \log p d \log \theta} \approx \alpha_s \frac{t}{t_{\text{split}}(p)}, \quad (32)$$

Note that the ratio t/t_{split} is smaller than 1 for nodes above k_{split} and therefore the number of daughters is smaller than the number of vacuum splitted quanta. Below k_{split} the cascade is similar to the medium cascade and the number of quanta become

$$\frac{dn}{d \log p d \log \theta} \approx \alpha_s \frac{t}{t_{\text{split}}(p)}, \text{ for } p < k_{\text{split}}(p) \quad (33)$$

The angular distribution is driven by two mechanisms; Multiple soft scatterings give rise to transverse Brownian motion, which determines the distribution at small angles. The typical angle reached in the LPM region is

$$\theta_{\text{BR}}(p) \approx \frac{\sqrt{\hat{q}t}}{p}, \text{ for } k_{\text{form}} > p > k_{\text{split}}, \quad (34)$$

while in the medium cascade region of the phase space this becomes

$$\theta_{\text{BR}}(p) \approx \left(\frac{T}{p}\right)^{\frac{3}{4}} \quad (35)$$

Large angular scales cannot be reached by Brownian motion, but can arise from rare large angle scatterings, described by Molière [1].

1.5.5 Jet shape measurements

1.6 QGP in Small systems

After the existence of QGP in heavy-ion collisions has been established, attention has been turned to small systems. Proton-proton (pp) and proton-Lead (pPb)

789 collisions have been studied at LHC and RHIC has studied a host of different
 790 collision systems; namely proton-Gold (pAu), deuteron-Gold (dAu) and Helium³-
 791 Gold (³HeAu) collisions starting in 2000.

792 Already before the era of modern colliders, collective behaviour in proton-
 793 proton collisions was considered by names like Heisenberg, Fermi and Bjorken. [116]
 794 Eventually there were some experimental searches of QGP in pp and $p\bar{p}$ collisions
 795 in E735 at Tevatron [117] and MiniMAX [118]. However no conclusive evidence
 796 was found.

797 In the early years of RHIC these small systems were mostly considered as con-
 798 trol measurement, for example in constraining nuclear modified parton distribution
 799 functions (nPDFs) that determine the initial gluon distributions that determine
 800 the first epoch of heavy-ion collisions [119, 120].

801 In 2010 ultrahigh-multiplicity pp collisions were studied at CMS. The study
 802 found that particles had a weak but clear preference to be emitted along a com-
 803 mon transverse ϕ angle across all rapidities [121]. This seemed like behaviour
 804 were similar to AA collisions, but it was argued that it could as well come from
 805 momentum correlations present in the earliest moments of the collision.

806 In 2012 LHC ran its first pPb data taking period. Around the same time
 807 dAu data was reexamined at RHIC. Now it was revealed that most of the flow
 808 signatures attributed to hydrodynamic expansion in AA collisions also existed in
 809 smaller systems.

810 -Sub nucleonic structure needed to describe intial conditions in pA, pp

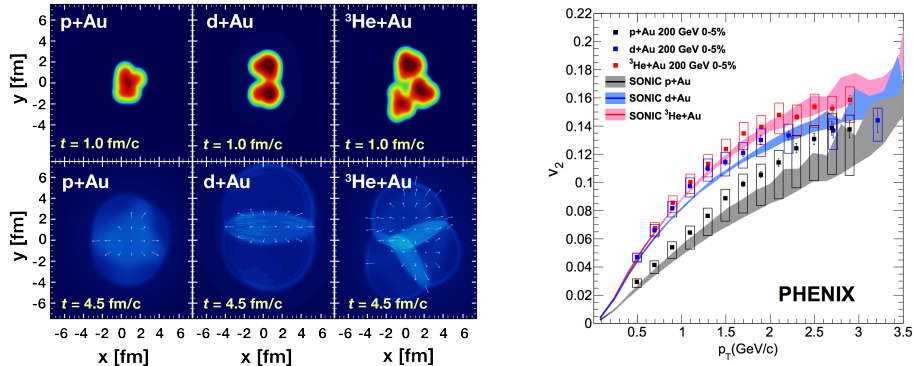


Figure 20: Calculations of the intial energy density in small collision systems at RHIC and the resulting hydrodynamic evolution.

811 1.6.1 Collective phenomena

812 The most rugged analysis of collective behaviour concerns the two (or more) parti-
 813 cle correlations, often parametrised via the relative azimuthal angle and pseudora-
 814 pidity differences, $\Delta\phi$ and $\Delta\eta$ respectively. Figure 21 shows two-particle correla-
 815 tions measurements in PbPb, pPb and pp collisions at the LHC. In PbPb collisions
 816 long-range correlations dominate over short-range phenomena. This shows in the
 817 two ridges at $\Delta\phi = 0$ and $\Delta\phi = \pi$. At $\Delta\phi \approx \Delta\eta \approx 0$, there is a peak coming from
 818 single jet fragmentation. Since the away-side jet can be spread out in $\Delta\eta$, this
 819 contribution disappears when compared to the flow contribution at the away side
 820 ridge. In pPb, and pp the near side peak is more distinguished and the away-side
 821 jet contribution starts to show. Still, one can see long-range correlations that seem
 822 like flow-like collective behaviour in both systems.

823 In addition to the two particle correlations, correlations have been observed in
 824 the form of v_n coefficients both at LHC and at RHIC. The results have also been
 825 described with hydrodynamical models, although the applicability of said models
 826 is questionable, because of the large Reynolds numbers in small systems. Figure
 827 20 shows results for v_2 in different collisions systems at RHIC as measured by
 828 PHENIX. These different systems provide also different initial geometries. dAu
 829 collisions naturally have an ellipsoidal form, while a He3 collision has a triangular
 830 form and thus produces larger triangular flow, v_3 components.

831 Other observations that produce flow-like results include mass ordered v_2 coeffi-
 832 cients and higher order harmonics coming from fluctuations in the initial geometry.
 833 Thus all the major collective flow phenomena observed in heavy-ion collisions have
 834 been also identified in small systems.

835 One open question is identifying the point the point, where flow-like correla-
 836 tions end. The question has proved challenging since low multiplicity events are
 837 dominated by non-flow phenomena. This makes observations in low multiplicity
 838 events model/method dependant. Different methods assess non-flow contributions

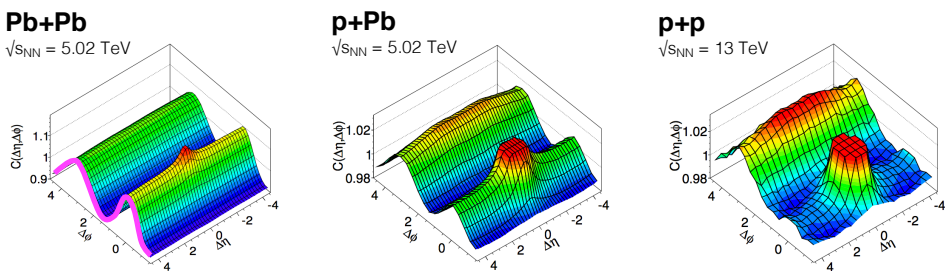


Figure 21: Two-particle correlation results in PbPb, pPb, and pp collisions at the LHC [1].

839 differently. Thus some methods fail to observe a signal in cases, where others do
840 and it is unclear whether this is true collective motion or it comes from non-flow
841 contributions.

842 1.6.2 Absence of jet quenching

843 In A+A collisions, an important confirmation of the standard model comes from
844 the energy loss of high p_T partons traversing the medium, referred to as jet quench-
845 ing [122–124]. In 2003 the jet quenching effect was observed to disappear in d+Au
846 collisions. This was taken as an indication that no QGP was created. Similarly at
847 LHC no jet modification has been observed in pPb collisions. Fig. 22 shows the
848 nuclear modification factor R_{pA} in pPb collisions as measured at the LHC.

849 The lack of jet modification seems surprising considering the multitude of flow
850 observations supporting the existence of QGP in small systems. One possible
851 explanation is simply the size of medium. In PbPb collision partons traversing
852 through the medium lose energy to the medium. If the medium is very small there
853 is limited time for interaction with the medium.

854 Calculations indicate that there should be modification in the most central
855 pPb collisions, but selecting these in the analysis is complicated. In PbPb colli-
856 sions most of the particle production comes from the medium and thus the total
857 multiplicity is a good indicator of centrality. In pPb collisions, however the total
858 multiplicity is smaller and is more strongly influenced by jet phenomena. Events
859 with jets have naturally larger multiplicities and are more likely to be classified as
860 central events.

861 So far the only observable indicative of jet quenching in pPb collisions is the
862 high $p_T v_2$. In heavy-ion collisions this is not explained by hydrodynamics. Instead
863 it is assumed to come from jet quenching with different path lengths through the
864 medium in different directions. In Fig.22 ATLAS and CMS measurements of v_2 in
865 pPb and PbPb collisions are shown. The pPb results seem to follow a very similar
866 pattern.

867 1.6.3 Centrality determination in small systems

868 In lead-lead collisions the total multiplicity of the event is a good indicator of the
869 centrality of the collision. In proton-lead collisions the connection of multipli-
870 city and centrality is less clear. In p-Pb collisions the impact parameter is only
871 loosely correlated to N_{part} or N_{coll} . Hence, although one uses traditionally the
872 term centrality to refer to these measurements, the relevant parameters are N_{part}
873 and N_{coll} [1].

874 The Glauber model [43] is generally used to calculate geometrical quantities of
875 nuclear collisions (A-A or p-A). In this model, the impact parameter b controls the

Table 2: Summary of observations in small system

Observable	PbPb	pPb	pp
Jet RpA/RAA	Modified	No modification	-
Hadron RpA/RAA	Modified	No modification	-
Heavy flavors			
Jet shape	Broadening	No observations	-
Two-particle correlations	Ridge	Ridge	Ridge
v_2	Observed	Observed	Observed
Mass ordered flow			
Higher ordered harmonics			
High $p_T v_2$	Observed	Maybe	-

876 average number of participating nucleons N_{part} and the corresponding number of
 877 collisions N_{coll} . It is expected that variations of the amount of matter overlapping
 878 in the collision region will change the number of produced particles, and parameters
 879 such as N_{part} and N_{coll} have traditionally been used to describe those changes
 880 quantitatively, and to relate them to pp collisions.

881 The problem in p–Pb collisions, is that fluctuations in multiplicity coming from
 882 for example hard scatterings are of the same order as the differences in multiplicity
 883 between centrality classes. In Pb–Pb collisions these multiplicity fluctuations have
 884 little influence on the centrality determination, the range of N_{part} or N_{coll} is large
 885 and $P(M|v)$ converges quickly to a Gaussian with a small width relative to the
 886 range of v .

887 Thus in practice selecting high multiplicity one chooses not only large average

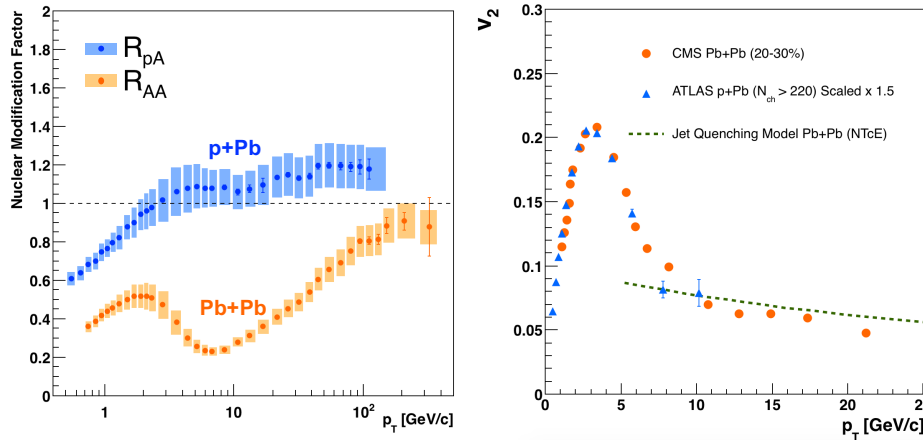


Figure 22: RpA in proton-lead collisions

888 N_{part} , but also positive multiplicity fluctuations leading to deviations from the
 889 binary scaling of hard processes. These fluctuations are partly related to qualitatively
 890 different types of collisions. High multiplicity nucleon-nucleon collisions
 891 show a significantly higher particle mean transverse momentum. They can be
 892 understood as harder collisions with larger momentum transfer Q^2 or as nucleon-nucleon
 893 collisions where multiple parton-parton interactions (MPI) take place.
 894 This is illustrated in Fig. 24.

895 Of particular interest are estimators from kinematic regions that are causally disconnected after the collision. The measurement of a finite correlation between
 896 them unambiguously establishes their connection to the common collision geometry.
 897 Typically these studies are performed with observables from well separated pseudorapidity (η) intervals, e.g. at zero-degree (spectators, slow-nucleons,
 898 deuteron break-up probability) and multiplicity in the rapidity plateau.
 899

900 One centrality selection that is argued not to induce a bias on the binary scaling
 901 of hard processes is provided by the energy measurement with the Zero Degree
 902 Calorimeters (ZDC) in ALICE, due to their large η -separation from the central
 903 barrel detectors. They detect the "slow" nucleons produced in the interaction by
 904 nuclear de-excitation processes or knocked out by wounded nucleons.
 905

906 Additional kinematic biases exist for events containing high- p_T particles, which
 907 arise from the fragmentation of partons produced in parton-parton scattering with
 908 large momentum transfer. Their contribution to the overall multiplicity increases
 909 with increasing parton energy and thus can introduce a trivial correlation between
 910 the centrality estimator and the presence of a high- p_T particle in the event. For
 911 very peripheral collisions, the multiplicity range that governs the centrality for the
 912 bulk of soft collisions can represent an effective veto on hard processes. For the

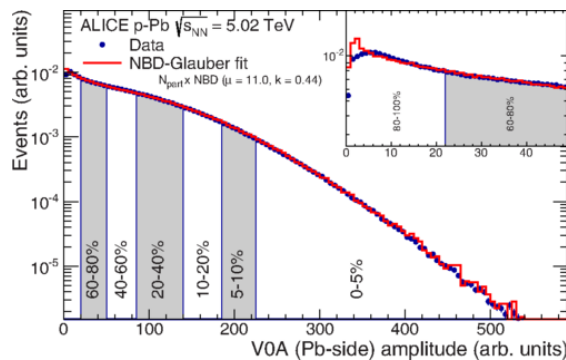


Figure 23: Distribution of the sum of amplitudes in the V0A hodoscopes (Pb-going), as well as the NBD-Glauber fit (explained in the text). Centrality classes are indicated by vertical lines. The inset shows a zoom-in on the most peripheral events. [1]

₉₁₃ nuclear modification factor this would lead to $R_{\text{pPb}} < 1$.

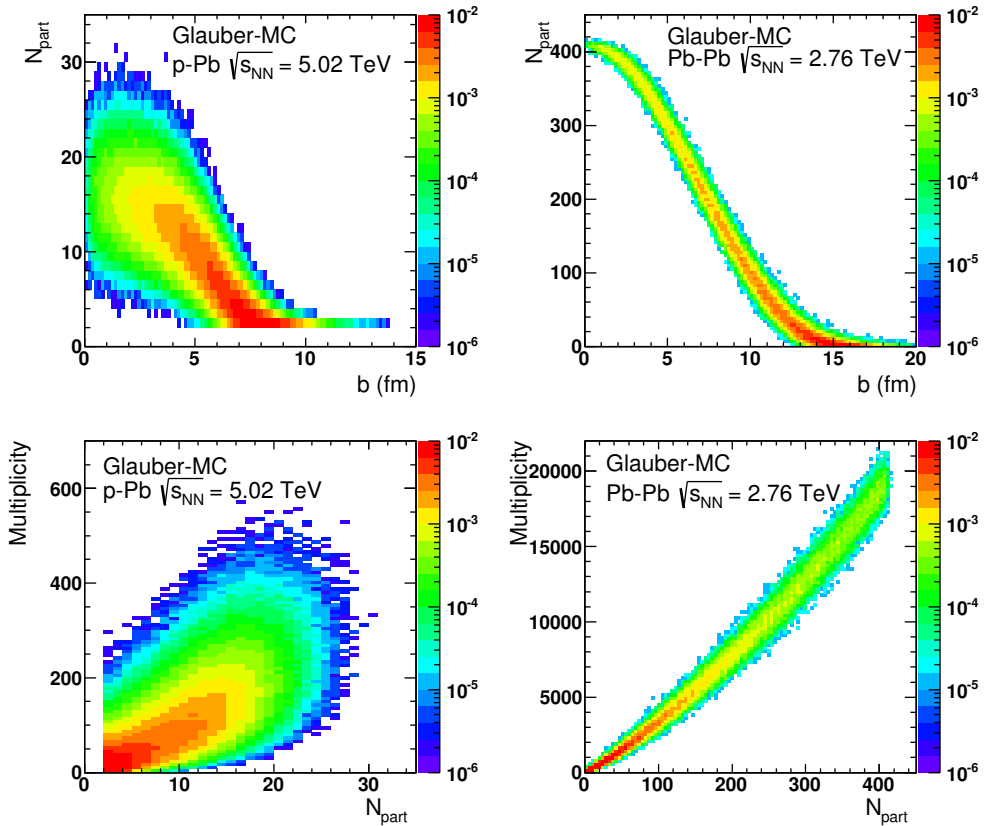


Figure 24: Top: Scatter plot of number of participating nucleons versus impact parameter; Bottom: Scatter plot of multiplicity versus the number of participating nucleons from the Glauber fit for V0A. The quantities are calculated with a Glauber Monte Carlo of p-Pb (left) and Pb-Pb (right) collisions. [1]

914 2 Experimental Setup

915 2.1 CERN

916 The European Organization for Nuclear Research (CERN), established in 1954, op-
 917 erates the largest particle physics laboratory in the world. In 2019 CERN consists
 918 of 22 member states. Additionally CERN has contacts with a number of associate
 919 member states and various individual institutions. The laboratory, also referred
 920 to as CERN, itself is located near Geneva at the border of France and Switzerland
 921 employs about 2500 people. Additionally some 12000 visiting scientists from over
 922 600 institutions in over 70 countries come to CERN for their research.

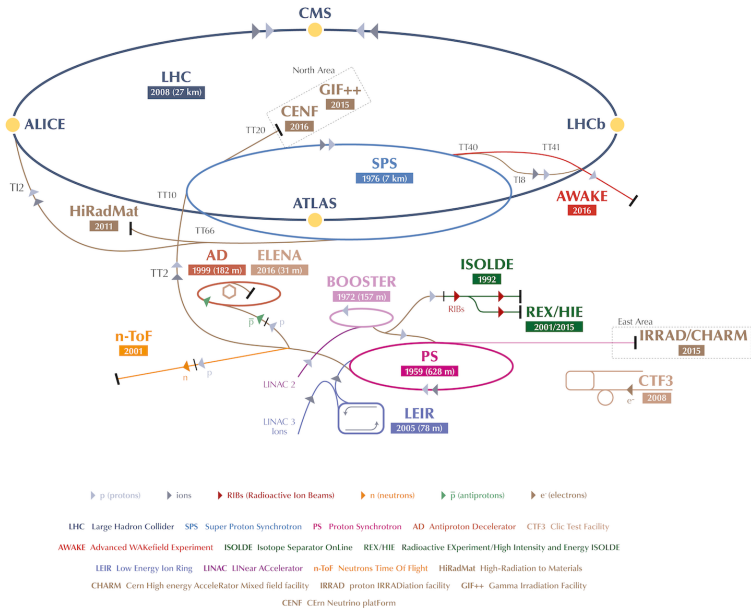


Figure 25: A schematic view of the accelerator complex at CERN. Before particles can be injected into the LHC they require a series of accelerators with increasing size. Until 2018 protons started their journey in LINAC2 (Linear Accelerator) and continue through the Booster, Proton Synchrotron (PS) and Super Proton Synchrotron (SPS). Between 2019 and 2020 LINAC2 will be replaced by LINAC4 [125]

923 The laboratory includes a series of accelerators, which are used to accelerate
 924 the particle beams used. A schematic view of the complex as of 2019 is shown in
 925 Figure 25. In the framework of this thesis the most important component is the
 926 Large Hadron Collider (LHC), the largest collider at CERN. LHC will be discussed

927 in more detail in Sec. 2.2. Other accelerators in the series are used to inject the
928 particle beams into LHC, but they are also used in itself for various experimental
929 studies.

930 The second largest accelerator is the super proton synchrotron (SPS). It is
931 the final step before the particle beam is injected into LHC. Commissioned in
932 1976, it was the largest accelerator at CERN until the the Large Electron-Positron
933 Collider (LEP) was finished in 1989. Originally it was used as a proton-antiproton
934 collider and as such provided the data for the UA1 and UA2 experiments, which
935 resulted in the discovery of the W and Z bosons [126]. At the moment there are
936 several fixed target experiments utilising the beam from the SPS. These study
937 the structure (COMPASS) and properties (NA61/SHINE) of hadrons, rare decays
938 of kaons (NA62) and radiation processes in strong electromagnetic fields (NA63).
939 Additionally the AWAKE and UA9 experiments are used for accelerator research
940 and development.

941 The third largest accelerator in CERN is the proton synchrotron (PS). Capable
942 of accelerating beams up to an energy of 25 GeV PS provides the beam to SPS.
943 Additionally PS has experiments for studying strong force (DIRAC), the effect
944 of cosmic rays on cloud formation (CLOUD) and neutron-nucleus interactions
945 (nTOF).

946 Additionally PS provides the beam to the antiproton decelerator (AD), which
947 uses the beam and a block of metal to produce antiprotons. These are then
948 decelerated in AD into a useful low-energy beam, which is provided to a host of
949 experiments studying the properties of antimatter.

950 PS gets proton beams from LINAC2 through BOOSTER and ion beams from
951 LINAC3 through LEIR. From BOOSTER beams are also provided to the On-Line
952 Isotope Mass Separator (ISOLDE). ISOLDE directs the beam into thick targets
953 to produce low energy beams of radioactive nuclei. These beams are used to study
954 the properties of even the most exotic of atomic nuclei in a host of experiments.

955 More information of the various experiments at CERN can be found online
956 from [127].

957 2.2 Large Hadron Collider

958 The Large Hadron Collider (LHC) with its circumference of 26.7 km is the largest
959 accelerator at CERN and the largest particle collider ever built. The LHC is
960 designed to accelerate protons up to an energy of 8 TeV and lead ions up to
961 2.76 TeV per nucleon [128]. The design luminosity of the LHC is $10^{34} \text{ cm}^{-2}\text{s}^{-1}$.
962 In 2017 it achieved a record peak luminosity of $2 \cdot 10^{34} \text{ cm}^{-2}\text{s}^{-1}$. For lead beams
963 luminosities of up to $6 \cdot 10^{27} \text{ cm}^{-2}\text{s}^{-1}$ were reached in 2018. All this is achieved
964 with a ring consisting of 1232 superconducting dipole magnets that keep particles
965 in orbit.

966 The LHC receives beams with energies of 450 GeV from the SPS. In the LHC
967 the particles are accelerated through the use of radio-frequency (RF) cavities.
968 Electromagnetic waves become resonant and build up inside the cavity. As they
969 consist of electromagnetic waves, the field in the RF cavity oscillates. Charges
970 passing through the cavity feel the overall force and are pushed forward along the
971 accelerator. Particles must enter the cavity at the correct phase of oscillation to
972 receive a forward push. When timed correctly, the particles will feel zero acceler-
973 erating voltage when they have exactly the correct energy. Particles with higher
974 energies will be decelerated and particles with lower energies will be accelerated.
975 This focuses particles in distinct bunches. The RF oscillation frequency at the
976 LHC is 400.8 MHz. Thus RF "buckets" are separated by 2.5 ns. However only 10
977 % are actually filled with particles, so the bunch spacing in the LHC is 25 ns, at
978 a bunch frequency of 40 MHz.

979 With 7 TeV proton beams the dipole magnets used to bend the beam must
980 produce a magnetic field of 8.33 T. This can be only achieved through making
981 the magnets superconducting, which requires cooling them down with helium to a
982 temperature of 1.9 K. The 1232 dipole magnets make up roughly 2/3 of the LHC
983 circumference. The remaining part is made up of the RF cavities, various sensors
984 and higher multipole magnets used to keep the beam focused. The most notable
985 of these are the 392 quadrupole magnets.

986 The LHC is divided into octants, where each octant has a distinct function.
987 Octants 2 and 8 are used to inject beam into the LHC from SPS. The 2 beams
988 are crossed in octants 1,2,5 and 8. The main experiments are built around these
989 crossing points. Octants 3 and 7 are used for beam cleansing. This is achieved
990 through collimators that scatter particles with too high momentum or position
991 offsets off from the beam. The RF cavities used for acceleration are located in
992 octant 4 and octant 6 is used for dumping the beam. The beam dump is made
993 up of two iron septum magnets, one for each beam, that will kick the beam away
994 from machine components into an absorber when needed.

995 2.2.1 LHC experiments

996 As of 2018 there are four main experiments at the LHC; ALICE, ATLAS, CMS
997 and LHCb and three smaller ones LHCf, TOTEM and MoEDAL. ALICE will be
998 covered in detail in section 2.3.

999 ATLAS (A Toroidal LHC ApparatuS) and CMS (Compact Muon Solenoid) are
1000 the two largest experiments at the LHC. They are both multipurpose experiments
1001 designed to be sensitive to many different possible new physics signals, such as ex-
1002 tra dimensions and dark matter particles. The biggest discovery made by these so
1003 far is the discovery of the Standard Model Higgs boson, which was simultaneously
1004 published by the experiments in 2012 [129,130].

1005 The LHCb (LHC beauty) experiment [131] is made for studying the bottom
1006 (beauty) quark. Main physics goals of the LHCb include the measurement of the
1007 parameters of CP violation with decays of hadrons containing the bottom quark.
1008 One of the most important results published by LHCb is the first measurement of
1009 $B_s^0 \rightarrow \mu^+ \mu^-$ decay, which was found to be in line with the Standard Model.

1010 In addition to the four large experiments there are three smaller experiments
1011 along the LHC ring. LHCf (LHC forward) [132] is located at interaction point 1
1012 with ATLAS. It aims to simulate cosmic rays by the particles thrown forwards by
1013 the collisions in ATLAS.

1014 TOTEM (TOTal Elastic and diffractive cross section Measurement) is located
1015 near the CMS experiment at point 5. This allows it to measure particles emerging
1016 from CMS with small angles. The main goals is to measure the total, elastic and
1017 inelastic cross-sections in pp collisions [133].

1018 The MoEDAL (Monopole and Exotics Detector At the LHC) experiment [134]
1019 is located at the interaction point 8 together with the LHCb experiment. MoEDAL
1020 tries to measure signatures of hypothetical particles with magnetic charge, mag-
1021 netic monopoles.

1022 2.3 ALICE

1023 ALICE (A Large Ion Collider Experiment) [135] is the dedicated heavy ion ex-
1024 periment at the LHC. ALICE was designed to cope with the expected very high
1025 multiplicity environment of heavy ion collisions. The design allows measurement
1026 of a large number of low momentum tracks. The different detector subsystems are
1027 optimised to provide high momentum resolution and excellent particle identifica-
1028 tion capabilities over a broad range of momentum.

1029 A schematic view of the ALICE detector in 2018 is presented in Figure 26.
1030 This section will go through the composition of ALICE as it has been during run 2
1031 between 2014 and 2018. The detector will go through significant upgrades during
1032 Long Shutdown 2 (LS2) in 2019-2020.

1033 As in all the major high energy physics experiments the positioning of the de-
1034 tectors follows a layered structure. Closest to the interaction point are the tracking
1035 detectors. The main task of these detectors is to locate the position of the pri-
1036 mary interaction vertex accurately and to record the tracks of charged particles.
1037 To achieve this they need a very good spatial resolution close to the interaction
1038 point. Tracking detectors do not significantly alter the tracks of traversing parti-
1039 cles. Thus they can be located in the innermost layers.

1040 Calorimeters are designed to stop any particles hitting them and use the ab-
1041 sorption to measure the energy of the particles. Thus they must be located behind
1042 the tracking detectors. ALICE has two separate calorimeter systems, the elec-
1043 tromagnetic calorimeters measure mainly electrons and photons, while the muon

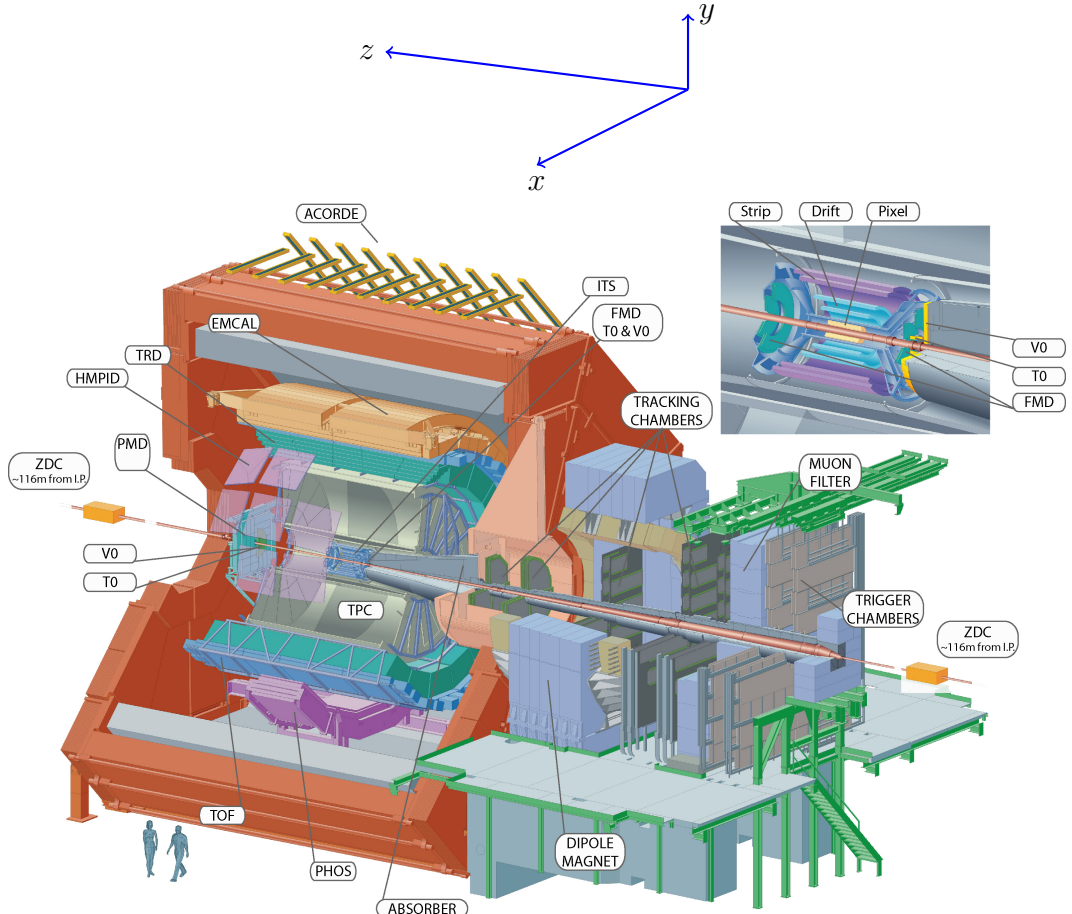


Figure 26: Schematic view of the ALICE detector with the definition of coordinates. The positive direction of *z* is also referred to as the A side and the negative direction as the C side

1044 detection system measures muons.

1045 2.3.1 Tracking

1046 The main design guideline for the tracking detectors in ALICE was the require-
1047 ment to have good track separation and high granularity in the high multiplicity
1048 environment of heavy ion collisions. Before the LHC started heavy ion runs the
1049 wildest estimates put the particle density at 8000 charged particles per unit of ra-
1050 pidity [135]. In reality the particle density turned out to be significantly smaller,
1051 about 1600 charged particles per rapidity unit [136].

1052 The main tracking detector in ALICE is the Time Projection Chamber
1053 (TPC) [137]. TPS is discussed in more detail in section 2.3.2

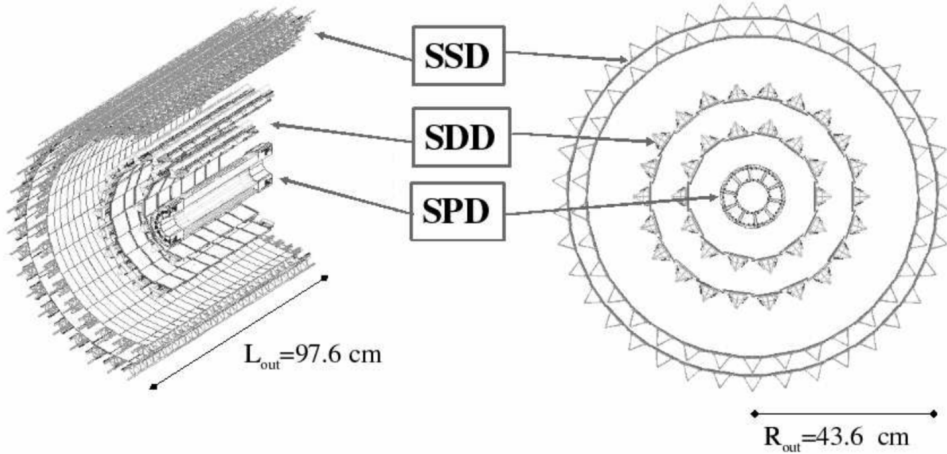


Figure 27: Schematic view of ALICE Inner Tracking System

1054 Between TPC and the beam pipe there is an array of six layers of silicon
 1055 detectors, called the inner tracking system (ITS) [138]. The main tasks of the
 1056 ITS are to locate the primary vertex with a resolution better than $100 \mu m$, to
 1057 reconstruct the secondary vertices from decaying particles, to track and identify
 1058 particles with momenta below 200 MeV and to compliment the momentum and
 1059 angle measurements of TPC. During long shutdown 2 in 2019-2020 the entire ITS
 1060 will be replaced [139]. As of 2018 the two innermost layers are made of the silicon
 1061 pixel detector (SPD). As it is the closest detector to the interaction point it requires
 1062 a very high spatial resolution. Thus the choice of pixel technology is natural. In
 1063 heavy ion collisions the particle density is around 50 particles per cm^2 .

1064 The next two layers together are the silicon drift detector (SDD). The layers
 1065 are made out of homogeneous neutron transmutation doped silicon, that is ionized
 1066 when a charged particle goes through the material. The generated charge then
 1067 drifts to the collection anodes, where it is measured. The maximum drift time
 1068 in SDD is about $5 \mu s$. This design gives very good multitrack capabilities and
 1069 provides two out of the four dE/dx samples in the ITS.

1070 The two remaining layers in the ITS are the silicon strip detector (SSD). The
 1071 strips work in a similar way as silicon pixels, but by itself one layer only provides
 1072 good resolution in one direction. Combining two crossing grids of strips provides 2
 1073 dimensional detection. Each charged particle will hit two intervening strips. The
 1074 position of the hit can be deduced from the place where the strips cross each other.

1075 **2.3.2 TPC**

1076 The time projection chamber (TPC) is a cylindrical detector filled with 88 m^3
1077 of Ne – CO₂ (90/10 %) gas mixture. The gas is contained in a field cage that
1078 provides an uniform electric field of 400 V/cm along the z-axis. Charged particles
1079 traversing through the TPC volume will ionise the gas along their path. This
1080 liberates electrons that drift towards the end plates of the cylinder. A schematic
1081 of the TPC is shown in Fig. 28.

1082 The field cage is separated into two detection volumes by the central high
1083 voltage electrode. Both sides have a drift length of 2.5 m and inner and outer
1084 diameters of 1.2 m and 5 m respectively. This means the central electrode must
1085 provide a maximum potential of 100 kV to achieve the design field magnitude. The
1086 maximum time required for electrons to drift through the chamber is about 90 μs .

1087 When electrons reach the end of the main cylinder they enter the readout
1088 chambers. The readout section of both sides consists of 18 outer chambers and
1089 18 inner chambers. Each of them is made of multiwire proportional chambers
1090 with cathode pad readouts. This design has been used in many TPCs before.
1091 During LS2 in 2019-2020, the multiwire chambers will be replaced by Gas Electron
1092 Multipliers (GEMs, see section 2.3.3).

1093 **2.3.3 TPC upgrade**

1094 During LS2 in 2019-2020 ALICE will go through significant modifications. The
1095 goal is to be able have continuous readout [140] in heavy ion collisions at an
1096 interaction rate of 50 kHz. ALICE will add a new Forward Interaction trigger
1097 (FIT) to replace the V0 and T0 detectors.

1098 Additionally the current inner tracking system (ITS) will be completely re-
1099 placed. The current layered structure with three different technologies will be
1100 replaced by an all pixel detector with significantly reduced pixel size. Additionally
1101 the first layer will be brought closer to the beam pipe. The new ITS will have
1102 better tracking efficiency and better impact parameter resolution.

1103 The muon detection will be complimented by the Muon Forward Tracker
1104 (MFT) [141]. Based on the same technology as the new ITS, MFT will be placed
1105 before the hadron absorber that sits in front of the existing muon spectrometer.
1106 MFT should significantly increase the signal/background ratio in heavy quark
1107 measurements.

1108 Many subdetectors will make small improvements to enhance the readout rate.
1109 The central trigger processor will be replaced and ALICE will introduce a new
1110 framework O^2 that combines both online data acquisition and offline analysis.

1111 The detector restricting the readout the most at the moment is the TPC.
1112 The current wire chamber based system limits the readout rate to 3.5 kHz. To

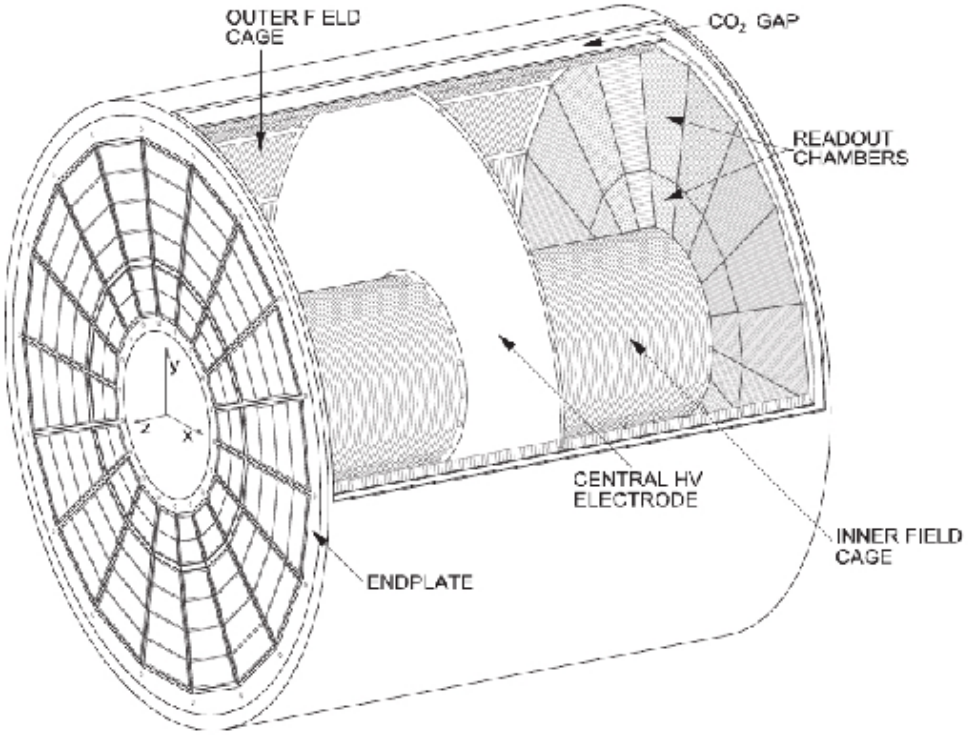


Figure 28: Schematic view of ALICE Time Projection Chamber

1113 achieve the 50 kHz readout rate goal the wire chambers will be replaced by a Gas
 1114 Electron Multiplier (GEM) based system. The GEMs are designed to minimise
 1115 ion backflow to allow continuous, ungated and untriggered readout. I have made
 1116 a personal contribution to the quality assurance of the new GEM readout of TPC.

1117 TPC has a total of 36 inner and 36 outer readout chambers. Each of these will
 1118 consist of 4 layers of GEM foils. The inner chambers will only have one foil for
 1119 each layer. The outer chambers are separated into three sections, each with its
 1120 own layer of foils. Each GEM foil is made up of a $50 \mu\text{m}$ thick resistive capton
 1121 layer, coated on both sides by $5\mu\text{m}$ thick layers of copper. Each foils is separated
 1122 into a number (20-24 depending on the size of the foil) of distinct active areas.
 1123 The active areas are pierced densely with holes. They have 50-100 holes in the
 1124 area of a single mm^2 . The density of holes changes from layer to layer. The two
 1125 middle layers of foils have a larger (double) pitch (smaller hole density) while the
 1126 top and bottom layers have a smaller (normal) pitch (larger hole density).

1127 The purpose of the multilayered structure is to reduce the ion backflow []; not
 1128 only one layer of GEM foils will be installed, but a 4 layer stack. In the stack there
 1129 are 2 standard pitch GEM foils, where the pitch size, i.e. the separation of the

holes inside a foil is around $140 \mu\text{m}$, and 2 large pitch GEM foils, there the hole spacing is two times larger, $280 \mu\text{m}$. The two outer layers will have standard pitch and the two middle layers have large pitch. The middle layers with large pitch serve as extra insulator against the ion backflow. Additionally the setup allows operating individual GEM foils at lower voltages and still have an increase in the gain of a few orders of magnitude. [142]

The holes have a conical shape which they acquire during a two step chemical etching process. The designed inner and outer diameters of the holes are $50 \pm 5 \mu\text{m}$ and $70 \pm 5 \mu\text{m}$ respectively. Fig. 29 shows the cross-section of a hole alongside with the operation principle of a GEM foil.

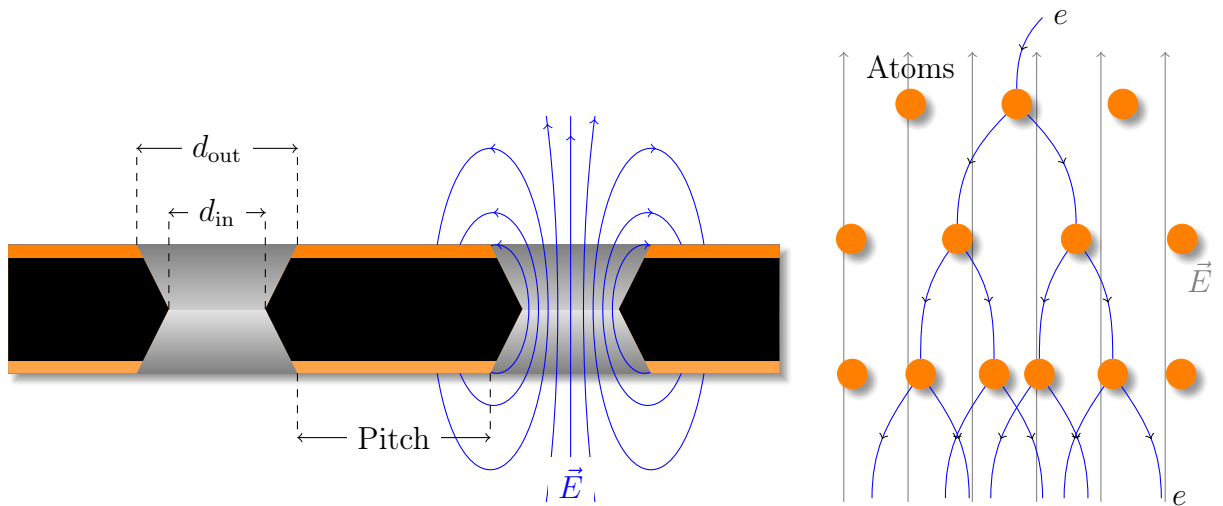


Figure 29: *left* Cross-section of a GEM foil. (Not to scale). The hole diameters are $d_{\text{in}} = 50 \pm 5 \mu\text{m}$ and $d_{\text{out}} = 70 \pm 5 \mu\text{m}$ and pitch is either 140 or 280 μm . *right* The amplification of a GEM foil is based on the Townsend avalanche phenomenon. Electrons entering the electric field inside the hole are accelerated. If they gain enough energy before colliding with atoms they can liberate additional electrons, which are further accelerated leading to a chain reaction.

The working principle of these foils is based on the Townsend avalanche phenomenon, which is also used in proportional counters such as Geiger counters. There is a large potential difference (140-400 V) applied to the two sides of the foil, which results in large field in each hole. Electrons gain energy in the field and if the electric field is strong enough, the free electron can gain sufficient velocity (energy) to liberate another electron when it next collides with a molecule. The two free electrons then travel along the electric field and can gain sufficient energy from the electric field to cause further impact ionisations, and so on, leading to a chain reaction. Under the right conditions a single electron entering any hole will

1149 create an avalanche containing 100–1000 electrons; this is the gain of the GEM
1150 foil.

1151 As opposed to wire chambers, which typically have one voltage setting, a GEM-
1152 based detector requires several independent voltage settings: there is a drift voltage
1153 which drives the electrons from the ionisation point to the GEM, an amplification
1154 voltage, and an extraction voltage that brings electrons from the GEM exit to the
1155 readout plane. In a multilayer system this is further complicated by the voltages
1156 between layers of foils.

1157 Quality Assurance of the GEM foils

1158 The GEM foils are produced at CERN, where they will undergo a basic QA (QA-B)
1159 procedure, that includes a coarse optical inspection for any large defects ($\gtrsim 1$ mm)
1160 and a short term high voltage measurement. Afterwards the foils are sent for an
1161 advanced quality assurance (QA-A) procedure which is performed in one of the
1162 two QA-A centers, one in the Helsinki Institute of Physics (HIP) and one in the
1163 Wigner Research Centre in Budapest. Details of the QA-A procedure can be found
1164 in the thesis of Márton Vargyas [143] and in [144]. In the QA-A centers all foils
1165 are put through a detailed optical scanning process and a long term high voltage
1166 measurement. I was personally performing the QA production in Helsinki for the
1167 final 6 months of the project.

1168 The optical scan is performed with the help of a scanning robot. The setup
1169 along with most of the software was developed at the Detector Laboratory of the
1170 Helsinki Institute of Physics [145]. The optical scan is able to distinguish every
1171 single hole on the GEM foil and measure their properties. The purpose of the
1172 scan is two-fold; to catch defects that could affect the performance and classify the
1173 foils based on their hole parameters. It is expected that these are connected with
1174 the foil’s electric properties [145]. For example, smaller holes create more intense
1175 and focused fields, which would result in larger amplification of their avalanche
1176 electrons, i.e. the local gain is expected to be larger.

1177 After the optical scanning, the foils are subjected to a long term (5-12 hours)
1178 high voltage leakage current measurement. Each segment of the GEM foil is con-
1179 nected to a high voltage of 500 V and the leakage current is measured separately
1180 for each segment. The accepted leakage current in each segment is 0.16 nA.

1181 Foils that fail the criteria are either trashed or sent to CERN for recleaning or
1182 repairing, after which they will go through the QA pipeline again.

1183 Additionally some foils will be put through a gain mapping procedure. As it is
1184 time consuming can only be performed in the QA-A center in Budapest it is only
1185 a small subset of foils. However, by measuring the gain in some foils the gain can
1186 be correlated with foil properties. Thus the single foil gain can be predicted based
1187 on the results of the optical scan. Details can be found in [143].

1188 **2.3.4 Particle identification**

1189 One guiding principle in the design of ALICE was to achieve good particle iden-
1190 tification (PID) over a large part of phases space and for several different particle
1191 types. In ALICE there are several detectors taking part in the identification of
1192 particles.

1193 One of the particle identification detectors is the transition radiation detector
1194 (TRD) [146]. Its main task is identifying electors with momenta larger than 1 GeV.
1195 Transition radiation is produced when highly relativistic particles traverse the
1196 boundary between two media having different dielectric constants. The average
1197 energy of the emitted photon is approximately proportional to the Lorentz factor γ
1198 of the particle, which provides an excellent way of discriminating between electrons
1199 and pion. ALICE TRD is made of a composite layer of foam and fibres. The
1200 emitted photons are then measured in six layers of Xe/CO₂ filled time expansion
1201 wire chambers.

1202 The time of flight (TOF) detector [147] uses a very simple physics principle,
1203 i.e. calculating the velocity of the particle using the time of flight between two
1204 points. Combining this with the momentum of particle, obtained from the tracking
1205 detectors, one can calculate the mass of the particle, which identifies particles. The
1206 TOF detector consists of multigap resistive wire chambers. These are stacks of
1207 resistive plates spaced equally. They allow time of flight measurements in large
1208 acceptance with high efficiency and with a resolution better than 100 ps.

1209 The third specific particle identification detector is the high momentum particle
1210 identification (HMPID) detector [148]. The HMPID uses a ring imaging Cherenkov
1211 counter to identify particles with momenta larger than 1 GeV. Particles moving
1212 through a material faster than the speed of light in the material will produce
1213 Cherenkov radiation. The velocity of the particle determines the angle at which
1214 the radiation is emitted. Measuring this angle gives the velocity of the particle.
1215 This can be again used to calculate the mass of the particle, if the momentum is
1216 known. In HMPID the material is a liquid radiator and the photons are measured
1217 with multiwire proportional chambers in conjunction with photocathodes.

1218 In addition to the specific particle identification detectors, the general purpose
1219 tracking detectors can be used for identification through the use of specific energy
1220 loss of charged particles traversing through a medium and the transition radiation
1221 emitted by charged particles when crossing the boundary between two materials.

1222 dE/dx measurements are provided by the last four layers of the ITS detector,
1223 i.e. the SDD and the SSD, thanks to their analog readout [149]. ITS can provide
1224 particle identification in the low p_T region, up to 1 GeV, and pions reconstructed in
1225 the standalone mode can be identified down to 100 MeV. Similar to ITS the TPC
1226 detector provides specific energy loss measurements. TPC can identify charged
1227 hadrons up to p_T 1 – 2 GeV as well as light nuclei, He3 and He4.

1228 **2.3.5 Electromagnetic Calorimeter**

1229 Calorimeters are designed to measure the energy of particles. Electromagnetic
1230 calorimeters specialise in detecting particles that interact primarily through the
1231 electromagnetic interaction, namely photons and electrons. They are required in
1232 many neutral meson and direct photon analyses. In addition the energy informa-
1233 tion enhance jet measurements.

1234 ALICE has two electromagnetic calorimeters, the photon spectrometer
1235 (PHOS) [150] and the electromagnetic calorimeter (EMCal) [151]. PHOS is a
1236 homogeneous calorimeter that consists of scintillating PbWO_4 crystals, which
1237 generate a bremsstrahlung shower and produce scintillation light. The energy of
1238 the particle determines the amount of light produced. To improve the charged
1239 particle rejection, PHOS includes a charged particle veto detector (CPV) [?].
1240 PHOS is built to have a very fine granularity, making it well suited for measuring
1241 direct photons and neutral mesons.

1242 In comparison to PHOS, EMCal has coarser granularity, but a significantly
1243 larger acceptance, making it suitable for jet physics. The acceptance of EMCal in
1244 the azimuthal angle is $80 \text{ deg} < \phi < 187 \text{ deg}$. During long shutdown 1 in 2013-
1245 2015, EMCal was extended with the di-jet calorimeter (DCal) [152], giving an
1246 additional acceptance region of $260 \text{ deg} < \phi < 320 \text{ deg}$. This provides partial
1247 back-to-back coverage.

1248 EMcal is segmented into 10 full size super modules (SM), 5 for A side and 5 for
1249 C side, and two 1/3 sized SMs, one for each side. This segmentation can be seen
1250 in Fig. 30. Each SM is divided into 24 strips, each covering full η (24 towers) and
1251 2 towers in η . Each strip is composed of 2×2 tower modules. Thus each full size
1252 super module includes 1152 towers and in total the EMCal is made up of 12288
1253 towers.

1254 The build of individual towers is shown in Fig. 31. Each tower is built up from
1255 76 alternating layers of 1.44 mm Pb and 77 layers of 1.76 mm polystyrene base
1256 injection moulded scintillator. The lead tiles produce the shower and scintillator
1257 tiles the light. Each tower scintillator is equipped with reflectors on all sides
1258 to provide better gain and keep the four towers inside one module isolated. The
1259 scintillation photons produced in the active volume of the tower are collected by 36
1260 longitudinally placed wave length shifting light guide fibres. The light is eventually
1261 directed to the Avalanche Photo Diodes (APD) for readout.

1262 **2.3.6 Forward and trigger detectors**

1263 ALICE includes a few small and specialised detectors of importance. The event
1264 time is determined with very good precision ($< 25 \text{ ns}$) by the T0 detector [153].
1265 T0 consists of two sets of Cherenkov counters that are mounted around the beam

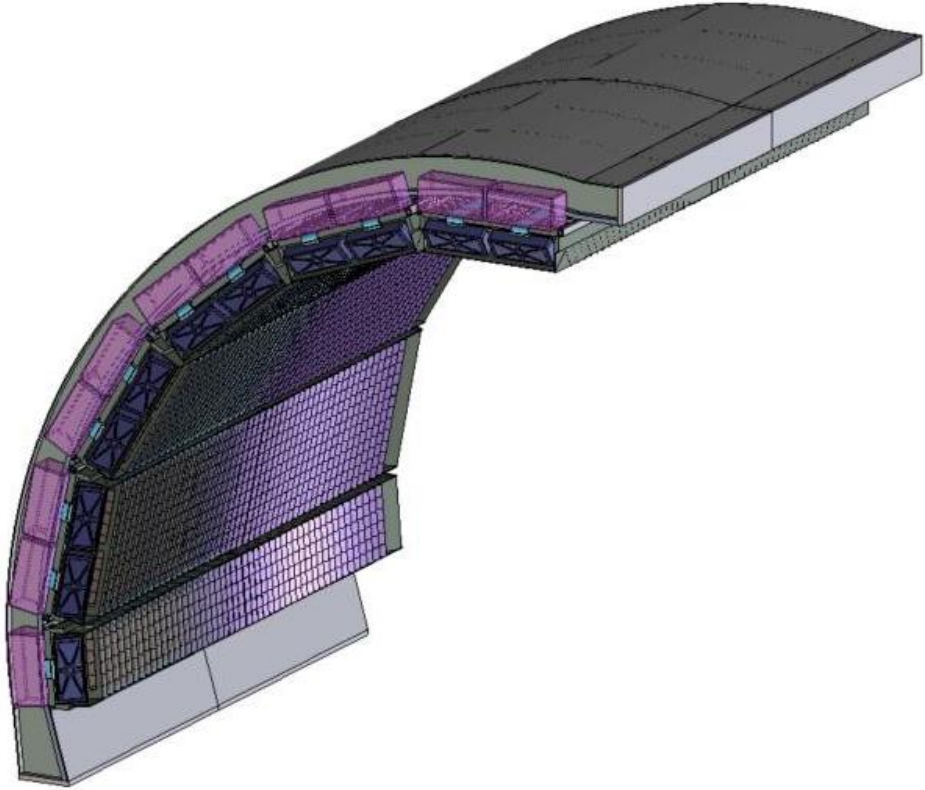


Figure 30: The EMCal detector arc, where the segmentation into 10 full size and 2 $\frac{1}{3}$ -sized (5 and 1 per side) supermodules can be seen.

1266 pipe on both sides of the interaction point. T0 gives the luminosity measurement
1267 in ALICE.

1268 Another small detector in the forward direction is the V0 detector [153]. This
1269 consists of two arrays of segmented scintillator counters located at $-3.7 < \eta <$
1270 -1.7 and $2.8 < \eta < 5.1$. V0 is used as a minimum bias trigger and for rejection
1271 of beam-gas background. Particle multiplicity in the forward direction can be
1272 related to the event centrality. Thus V0 is the main detector used in centrality
1273 determination in PbPb collisions.

1274 The multiplicity measurement of V0 is complimented by the forward multiplicity
1275 detector (FMD) [153]. FMD includes five rings of silicon strip detectors that
1276 make up the FMD. FMD gives acceptance in the range $-3.4 < \eta < -1.7$ and
1277 $1.7 < \eta < 5.0$.

1278 During long shutdown 2 in 2019-2020, V0 and T0 will be replaced by the Fast
1279 Interaction Trigger (FIT) detector [154]. For historical reasons elements of FIT are
1280 also referred to as V0+ and T0+. FIT will allow centrality, event plane, luminosity

THE EMCAL Module Components

Containment: 88 parts

- 1) Back (holes: 144 thru for fibers + springs + mech. support), 1
- 2) Compression (holes: 144 thru for fibers + springs), 1
- 3) Front Plate (holes: 144 thru for fibers + springs + mech. support), 1
- 4) 5) Plungers (10)
- 6) Belleville washers (75)

Tensioning and Insulation:

40 parts

- 7) Stainless steel straps (4)
- 8) Screws (24)
- 9) Flanges (8)
- 10) Light tight stickers (4)

Sandwich:

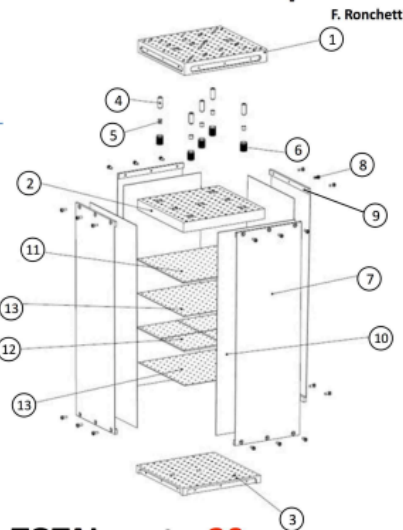
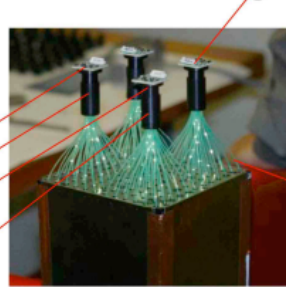
538 parts

- 11) Lead tiles (76)
- 12) Scintillator tiles (308)
- 13) Bond paper sheets (154)

Readout and Electronics:

165 parts

- 14) WLS fibers (144)
- 15) APD (4)
- 16) CSP (4)
- 17) Light guides (4)
- 18) Mount (4)
- 19) Collars (4)
- 20) Diffuser (1)



TOTAL parts: 20

TOTAL components: 831

Plus cabling, GMS and mech. supports

Figure 31: The exploded EMCAL tower view

and interaction time determination in the continuous readout mode, that ALICE will operate in after 2020.

For photon multiplicity measurement ALICE has the photon multiplicity detector (PMD) [155]. PMD uses two planes of gas proportional counters with a cellular honeycomb structure. PMD gives the multiplicity and spatial distribution of photons in the region $2.3 < \eta < 3.7$.

On top of the ALICE magnet there is an array of 60 large scintillators called the ALICE cosmic ray detector (ACORDE) [156]. ACORDE is used as a trigger for cosmic rays for calibration and alignment.

The only hadronic calorimeters in ALICE are the zero degree calorimeters (ZDC) [157], which are located next to the beam pipe in the machine tunnel about 116 m from the interaction point. There are two sets of calorimeters. One is made of tungsten, specialising in measuring neutrons, while the other, made of brass, is specialised in measuring protons. ZDC is meant to detect spectators, i.e. parts of the colliding ions that do not take part in the interaction. If there are more spectators, the collisions is likely to be more peripheral. Thus ZDC gives information about the centrality of the event especially in proton-lead collisions [1], but also in Pb–Pb collisions [158].

1299 A new detector installed during the long shutdown 1 is the ALICE diffractive
1300 detector (AD) [?]. AD consists of two assemblies, one in each side of the interaction
1301 point, both made of two layers of scintillators. These assemblies are situated about
1302 17 m and 19.5 m away from the interaction points. The pseudorapidity coverage is
1303 $-6.96 < \eta < -4.92$ and $4.78 < \eta < 6.31$. AD greatly enhances ALICE's capability
1304 for diffractive physics measurements that require a large pseudorapidity gap.

1305 2.3.7 Muon spectrometer

1306 Outside the main magnet, ALICE has a spectrometer dedicated to measuring
1307 muons [159]. In heavy ion physics muons are mainly used to measure the produc-
1308 tion of the heavy quark resonances J/ψ , Ψ' , Υ , Υ' and Υ'' .

1309 The muon spectrometer consists of three parts, the absorber, the muon tracker
1310 and the muon trigger. The absorber is meant to remove the hadronic background
1311 as efficiently as possible. After the absorber there are ten plates of thin cathode
1312 strip tracking stations with high granularity, the muon tracker. After the muon
1313 tracker there is a layer of iron to filter out any remaining particles, other than
1314 muons. The muon trigger is located behind this layer. The trigger consists of four
1315 resistive plate chambers.

1316 2.3.8 Triggers

1317 High energy physics experiments need triggers to select interesting physics. Ex-
1318 periments such as CMS and ATLAS at CERN look for extremely rare events with
1319 up to 40 million events each second. Such amounts can't be recorded real-time as
1320 many detectors require some time for the readout, up to 1 ms/event in ALICE.
1321 Thus one uses triggers, i.e. a set of very fast hardware based decisions on which
1322 events are to be saved. Additionally one needs some confirmation that an event
1323 has even occurred to tell other detectors that the event needs to be recorded.

1324 For ALICE the target event rates are 1 MHz for ppcollisions, 0.1-2 kHz for
1325 Pb-Pbcollisions and 200 kHz for the 2013 p-Pbcollisions.

1326 At ALICE the main system responsible for the trigger decisions is the AL-
1327 ICE Central Trigger Processor (CTP) [?]. The CTP generates three levels of
1328 hierarchical hardware triggers - Level 0, Level 1 and Level 2, (L0, L1 and L2 re-
1329 spectively) before an event is accepted and transmitted to the Data Acquisition
1330 system (DAQ). Afterwards additional software assessments are performed by the
1331 High Level Trigger (HLT).

1332 Triggers can be roughly put into two classes, minimum bias triggers that make
1333 sure no empty events are recorded, and rare triggers that require specific signatures
1334 in ALICE detectors, such as large energy deposits in EMCAL or two muons in the
1335 muon arm acceptance.

1336 **Minimum bias trigger**

1337 Several of the ALICE detectors are used to make the initial minimum bias trigger
1338 decisions. These include the SPD layers of ITS, V0 and T0. SPD can count the
1339 number of hits in the first two layers of ITS. Minimum bias ppcollisions typically
1340 require at least one hit in either SPD or V0A/V0C. Similarly Pb–Pbtriggers look
1341 at both V0 and SPD hits. The p–Pbdata has been mainly triggered using V0
1342 information.

1343 **EMCal trigger**

1344 In addition to the minimum bias triggers, the most relevant trigger for this thesis
1345 is the EMCal trigger. Much of the EMCal trigger has been developed at the
1346 University of Jyväskylä. Extensive details of the trigger and the development
1347 work can be found in the thesis of Jiří Král [160]. Personally I have spent time at
1348 CERN helping in the maintenance of the level 0 trigger.

1349 ALICE EMCal provides two levels of trigger signal, L0 and L1, which allows
1350 triggering on either single shower deposits or integrated energy deposits in larger
1351 ares, i.e. jets [161].

1352 As inputs the trigger gets exclusive sets of 2×2 EMCal towers, to limit the
1353 number of channels that need to be processed. The L0 trigger then checks for
1354 energy deposits within a rolling window of 2×2 trigger channels (4×4 towers).
1355 Areas of 4×4 towers most probably will contain only a single shower. (or two
1356 adjacent showers coming from a single decayed π^0) Thus the trigger is called the
1357 single shower trigger.

1358 For L0 the trigger decision is done in Trigger Region Units (TRU) that each
1359 cover 4×42 channels (8×48 towers). The amplitude from the sliding window
1360 is compared to a constant threshold. Additionally a peak finding algorithm is
1361 implemented to define correctly the time of the signal maximum. A single bit OR
1362 decision of all individual TRUs is forwarded to the CTP as the EMCal L0 trigger
1363 decision.

1364 The L0 information is additionally forwarded to the Level 1 trigger, which
1365 recomputes similar 2×2 channel decisions to produce the single shower trigger,
1366 but L1 can perform the calculation also on the borders between trigger units. In
1367 addition the L1 trigger can check for energy deposits inside a larger 16×16 channel
1368 (32×32 towers) window, which is considered to be the jet trigger.

1369 The L1 trigger can compare up to two thresholds for each single shower and
1370 jet trigger. There is a dedicated link in between the V0 detector and EMCal STU,
1371 which can provide centrality information that is used to compute a dynamical
1372 threshold as a function of the V0 multiplicity.

1373 The trigger subsystem provides both the L0 and L1 decisions to the CTP and

₁₃₇₄ DAQ.

3 Event and track selection

The $\sqrt{s_{\text{NN}}} = 5.02$ TeV p–Pb ($1.3 \cdot 10^8$ events, $\mathcal{L}_{\text{int}} = 620 \text{ nb}^{-1}$) collisions were recorded in 2013 by the ALICE detector [162]. The details of the performance of the ALICE detector during LHC Run 1 (2009–2013) are presented in Ref. [163].

3.1 Event selection

This analysis uses both a minimum bias trigger and an EMCal based trigger to select the analysed events. For the 2013 p–Pb collisions minimum bias events are required to have signals in both V0A and V0C. This condition is used later offline to reduce the contamination of the data sample from beam-gas events by using the timing difference of the signal between the two stations [163].

EMCal is also used to provide the jet trigger used in triggered datasets. EMCal can be used to trigger on single shower deposits or energy deposits integrated over a larger area. Latter case is used for jet triggers. The EMCal trigger definition in the 2013 p–Pb collisions requires an energy deposit of either 10 GeV for the low threshold trigger or 20 GeV for the high threshold trigger in a 32×32 patch size.

The EMCal

Triggers, V0 and EMCal are discussed in more detail in sections 2.3.6, 2.3.8 and 2.3.5.

3.2 Track reconstruction

The analysis uses charged tracks that are reconstructed with the Inner Tracking System (ITS) [164] and the Time Projection Chamber (TPC) [165]. These are discussed in sections 2.3.1 and 2.3.2. A detailed overview of track reconstruction in ALICE can be found from [163].

The track reconstruction procedure is shown in Fig. 32. The figure shows only one track, but in reality the reconstruction has to deal with many tracks. The main reconstruction of tracks starts in TPC. There are 159 tangential pad rows in the TPC readout chambers. The track reconstruction starts from the outermost layer and the hits are paired with hits in the next layer inwards, taking into account a proximity cut. When this track finding procedure hits the innermost pad row in TPC, this information is used as an initial seed for the track finding in ITS. Similar procedure of pairing adjacent layers with a proximity cut is repeated in ITS.

After the reconstruction of tracks in ITS is completed, all the tracks are extrapolated to their point of closest approach to the preliminary interaction vertex. Then the second track fitting step begins, this time starting from the interaction point and proceeding outwards. A Kalman filter [166] technique is used to do the

1411 new fit using the hits found in the previous stage. This time the tracks are matched
1412 also to the other detectors in the central barrel beyond TPC. When this step is
1413 complete, a final refit from the outermost TPC pad rows towards the interaction
1414 point is performed. The final track parameters come from this refit.

1415 With the final track parameters the primary vertex can be determined with
1416 better accuracy than with only SPD information. The tracks are extrapolated to
1417 the nominal beam line and a weighted average of the points of closest approach
1418 determines the accurate primary vertex position.

1419 The final step of the track reconstruction is the determination of the secondary
1420 vertices. For this, all the tracks whose distance of closest approach (DCA) to
1421 the primary vertex is larger than a defined minimum value ($??$ mm in p–Pb) are
1422 selected. For these tracks, points of closest approaches are determined for pairs of
1423 tracks. If the tracks are sufficiently close to each other and show characteristics of
1424 short lived particle decays, these points are identified as secondary vertices.

1425 Combining the information from the ITS and the TPC provides a resolution
1426 ranging from 1 to 10 % for charged particles with momenta from 0.15 to 100 GeV/c.
1427 For tracks without the ITS information, the momentum resolution is comparable
1428 to that of ITS+TPC tracks below transverse momentum $p_T = 10$ GeV/c, but for
1429 higher momenta the resolution reaches 20 % at $p_T = 50$ GeV/c [163, 167].

1430 Track selection

1431 In p–Pb collisions the tracks are selected following the hybrid approach [168] which
1432 ensures a uniform distribution of tracks as a function of azimuthal angle (φ). The
1433 parameters in the approach are summarised in table 3.

1434 The first requirements are on the quality of the track fit in ITS and TPC.
1435 The ITS requirement only removes tracks that are clear outliers. For TPC the
1436 requirement is much more strict. For step 1 it is required that a track has 3 out
1437 of the 6 possible hits in ITS, one of which must be in the SPD. In step 2 this
1438 is replaced by an additional vertex constraint, where the primary vertex itself is
1439 added as a point to the track to improve the momentum resolution.

1440 For the TPC, 70 crossed pad rows out of the maximum 159 is required. This
1441 measures the effective track length inside the TPC. This takes into account the
1442 possibility of having pad rows missing in the middle of the track due to charge in
1443 these clusters being below the threshold for some reason. Additionally it is required
1444 that the ratio between crossed rows and findable clusters is at least 0.8. Findable
1445 clusters are defined as the number of geometrically possible clusters which can be
1446 assigned to a track, taking into account dead zones due to chamber boundaries
1447 and limited η -acceptance. For both steps of the hybrid cut is is required that the
1448 fraction of clusters shared with several tracks is less than 40%.

1449 The remaining cuts are meant to make sure that the measured tracks are

Table 3: Parameters in the hybrid track cut

Track Cut	Step 1	Step 2
$\chi^2 / \text{ITS cluster}$	< 36	< 36
$\chi^2 / \text{ITS cluster}$	< 4	< 4
Hits in ITS	3	0
ITS hit requirements	1 in SPD	No requirement
Vertex constraint	No	Yes
Number of crossed rows in TPC	70	70
TPC crossed rows over findable clusters	> 0.8	> 0.8
Fraction of shared TPC clusters	< 0.4	< 0.4
Kink daughters	Rejected	Rejected
DCA_{xy}	< 3.2 cm	< 3.2 cm
DCA_z	< 2.4 cm	< 2.4 cm
Other		Rejected by step 1

1450 really produced in the primary collision. A track might gain a kink due to a
 1451 particle scattering decay. After this, it is no longer describing the properties of the
 1452 primary collisions. The particle after such a kink, a kink daughter, is rejected in
 1453 the cuts. The final cuts are on the distance of closest approach (DCA) of the track
 1454 to primary vertex. To have confidence that the track comes from the primary
 1455 collision, the track must be close enough to the primary vertex. The cuts are
 1456 different for the distance along (DCA_z) and perpendicular to (DCA_{xy}) the beam
 1457 axis.

1458 The momentum resolutions of the two classes of particles are comparable up
 1459 to $p_T \approx 10 \text{ GeV}/c$, but after that, tracks without ITS requirements have a worse
 1460 resolution [163, 167].

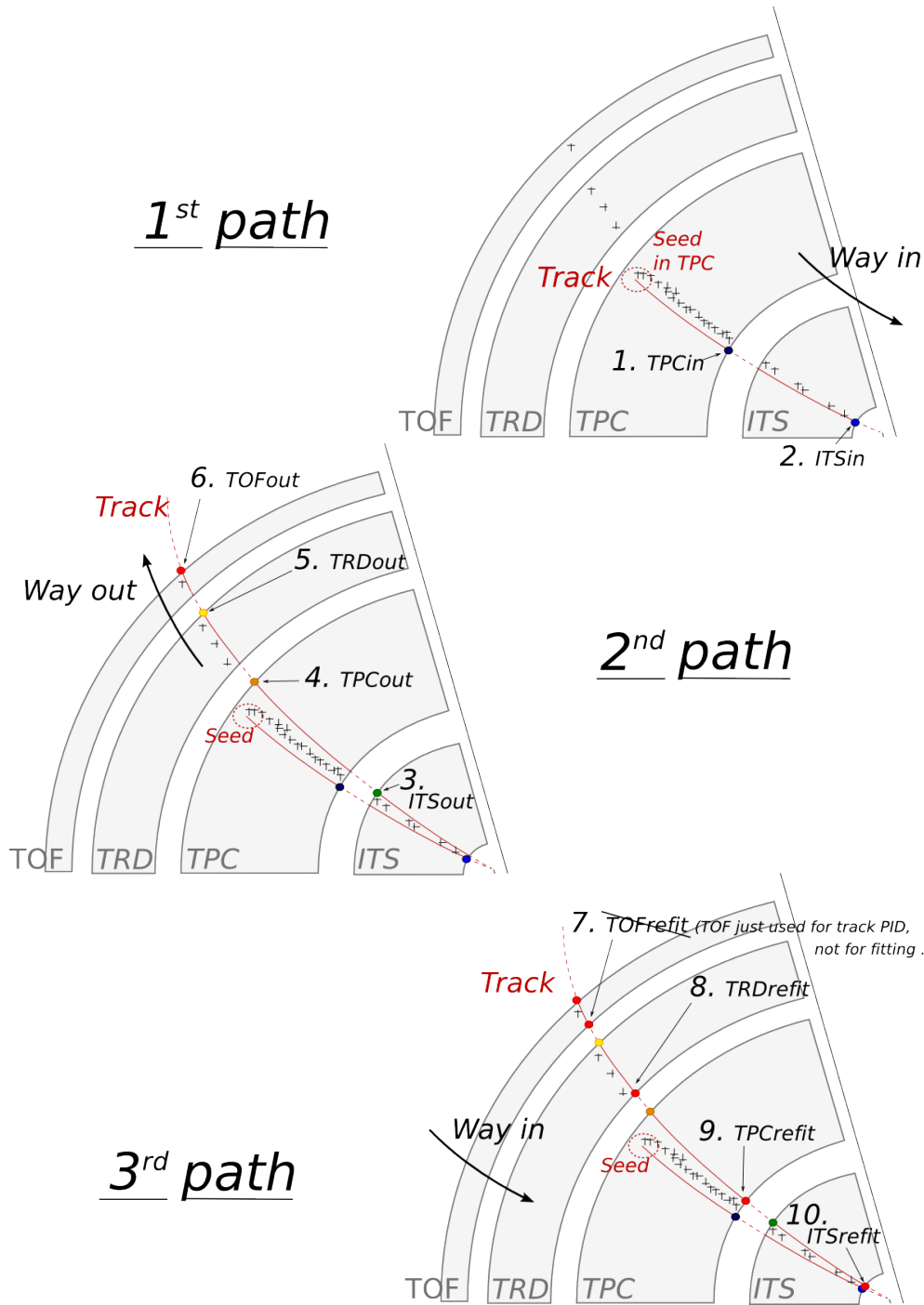


Figure 32: Principles of tracking in the ALICE experiment, showing the three successive paths allowing to build a track and refine its parameters. Numbers ranging from 1 to 10 mention the bits that are activated in case of success during the propagation of the Kalman filter at the considered stage. Figure from [?]

1461 3.3 Cluster selection

1462 Neutral particles used in jet reconstruction are reconstructed by the Electromagnetic Calorimeter (EMCal [151]. The EMCal covers an area with a range of
1463 $|\eta| < 0.7$ in pseudorapidity and 100 deg in azimuth. EMCal is complimented
1464 with the Dijet Calorimeter (DCal) [152] and Photon Spectrometer (PHOS) [150]
1465 that are situated opposite of the EMCal in azimuth. PHOS covers 70 degrees in
1466 azimuth and $|\eta| < 0.12$. The DCal is technologically identical to EMCal. The
1467 DCal coverage spans over 67 degrees in azimuth, but in pseudorapidity the mid
1468 region is occupied by the PHOS. In between PHOS and DCal active volumes, there
1469 is a gap of 10 cm. DCal is fully back-to-back with EMCal.
1470

1471 The clusters used in the analysis were obtained from EMCal by the v2 clusteriser.
1472 Clusters matched to charged tracks are removed from the analysis as well
1473 as clusters being identified as fake. The parameters used in the clusteriser are
1474 summarised in table 4

1475 The clusteriser searches for a tower with energy deposit greater than a defined
1476 seed energy and merges all surrounding (sharing a side) towers with energy deposit
1477 higher than a defined threshold. In the next step all towers sharing a side with
1478 already included towers are added, again requiring that the energy deposits exceeds
1479 the threshold. The algorithm can identify local minima and halts the clustering
1480 in case that the neighbouring tower energy is higher. Already clustered towers are
1481 removed from the pool, so one tower can only be clustered once.

1482 Highly energetic calorimeter hits should spread into several towers as the elec-
1483 tromagnetic shower evolves. However, some clusters with high energy have their
1484 energy located in a single tower. These are believed to come from slow neutron
1485 hitting the APD readout of the towers. These are called exotic clusters. The
1486 measure of exoticity is denoted as

$$1 - \frac{E_{\text{cross}}}{E_{\text{max}}}, \quad (36)$$

1487 where E_{max} is the energy in the most energetic tower and E_{cross} is the sum of the
1488 four towers neighbouring the most energetic one. The closer this is to 1, the more
1489 exotic the cluster is and the larger the probability that it is fake. Cut of 0.97 has
1490 been adopted as default for EMCal analyses, including this one.

1491 A method of matching the cluster position to TPC track extrapolation is used
1492 to suppress charged hadron contribution to hits in EMCal. Tracks identified by the
1493 tracking detectors are extrapolated close to the EMCal surface, where the closest
1494 cluster is found and the track extrapolation is continued until reaching the same
1495 depth as the cluster. The remaining distance in between the extrapolated track
1496 and the cluster is then used to reject hadronic hits.

Table 4: Parameters used in the EMCal clusteriser

Setting	Value
Clusteriser seed	0.2 MeV
Clusteriser cutoff	0.05 MeV
Cells in cluster	> 1
Track matching radius	0.025
Fiducial cut	1 tower
Exotic cut	0.97
Minimal cluster Energy	0.3 GeV

1497 4 Analysis method

1498 4.1 Jet Finding

1499 The analysis uses reconstructed jets as estimates of the original parton. Jet recon-
1500 struction essentially combines nearby tracks into jets.

1501 Collisions between hadrons are never as clean as electron-electron collisions.
1502 Even for a proton-proton collision there are participant partons, that will produce
1503 a soft background in addition to the hard scattering products. Jet reconstruction
1504 must deal with this soft background. The reconstruction is never perfect, one can
1505 have uncorrelated tracks that get included in the jet and some tracks originating
1506 from the parton are missed by the reconstruction. There are several methods to
1507 perform the reconstruction, all of which require some kind of size parameter, which
1508 cuts out jet participants too far from the jet axis. The tracks that are grouped
1509 into a jet are referred to as jet constituents.

1510 In each collision event, the jets are reconstructed using FastJet [169] with the
1511 anti- k_T algorithm [170]. Jets for $R=0.4$ are selected in $|\eta| < 0.25$ to satisfy the
1512 fiducial acceptance of the EMCAL. In jet reconstruction both charged tracks with
1513 $p_T > 0.15 \text{ GeV}/c$ and neutral clusters with $p_T > 0.30 \text{ GeV}/c$ are considered. The
1514 analysis is then performed by analysing the charged jet constituents and results
1515 are presented in terms of the jet transverse momentum $p_{T\text{jet}}$.

1516 4.1.1 Anti k_T algorithm

1517 Jets are reconstructed using the anti- k_T algorithm [170]. The algorithm works by
1518 trying to undo the splittings through combining protojets. First the algorithm
1519 creates a list of protojets. At the beginning the list is populated by converting
1520 each track in the event into a protojet. Then the algorithm proceeds by combining
1521 these protojets. A simplified picture of the process for a limited number of tracks
1522 is shown in Fig. 33

1523 The algorithm calculates distance measures for each individual protojet and
1524 for each possible pair of protojets. For individual protojets this depends only on
1525 the transverse momentum of the track.

$$k_{Ti}^2 = p_{Ti}^{2p} \quad (37)$$

1526 For each pair of protojets the distance measure is calculated as

$$k_{Ti,j}^2 = \min(p_{Ti}^{2p}, p_{Tj}^{2p}) \frac{\Delta R_{i,j}^2}{D^2}, \quad (38)$$

1527 where

$$R_{i,j} = (\phi_i - \phi_j)^2 + (y_i - y_j)^2. \quad (39)$$

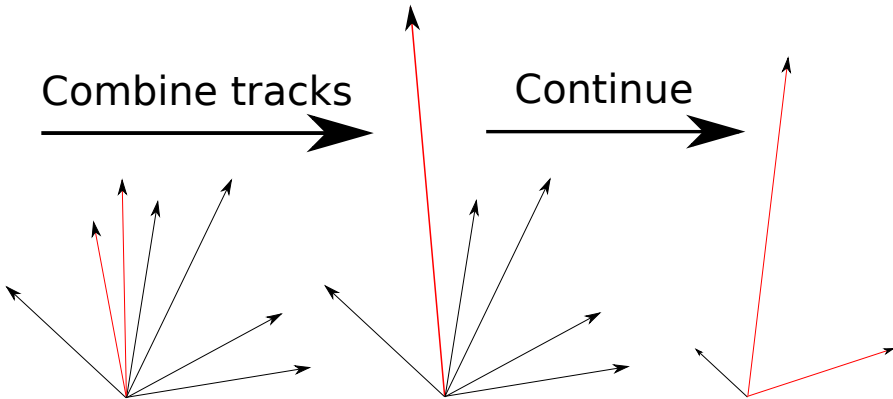


Figure 33: A simple example of the antil- k_T algorithm in progress. The red tracks in the leftmost figure are identified to have the smallest $k_{T,i}$ in the event and are combined into the red track of the middle figure. As this continues the remaining tracks are added to this or other jets. One tracks was deemed to be isolated enough to be counted as a protojet by itself. Note that the rightmost figure is zoomed out.

1528 If k_{Ti} is the smallest quantity then the protojet is a jet and it is removed from
1529 further consideration. If $k_{Ti,j}$ is the smallest quantity the two protojets i and j are
1530 merged. This is repeated until no protojets are left.

1531 The choice of the power p in the distance measure depends on the algorithm
1532 used

- 1533 • $p = 1$: k_T algorithm
- 1534 • $p = 0$: Cambridge Aachen algorithm
- 1535 • $p = -1$: anti- k_T algorithm

1536 With the choice $p = -1$ in anti- k_T algorithm, the softest splittings are un-
1537 done first. One consequence of the power choice in the anti- k_T algorithm is that
1538 reconstructed jets have a shape close to circular.

1539 4.2 Definition of j_T

1540 The jet fragmentation transverse momentum, \vec{j}_T , is defined as the component of
1541 the constituent particle momentum, \vec{p}_a , transverse to the jet momentum, \vec{p}_{jet} . The
1542 resulting \vec{j}_T is illustrated in Fig. 34. The length of the \vec{j}_T vector is

$$j_T = \frac{|\vec{p}_{jet} \times \vec{p}_{track}|}{|\vec{p}_{jet}|}. \quad (40)$$

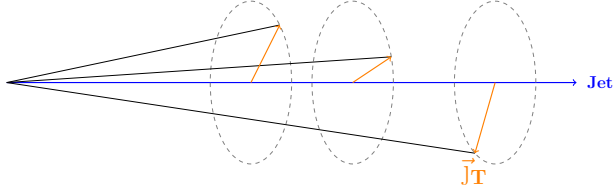


Figure 34: Illustration of \vec{j}_T . The jet fragmentation transverse momentum, \vec{j}_T , is defined as the transverse momentum component of the track momentum, \vec{p}_{track} , with respect to the jet momentum, \vec{p}_{jet} .

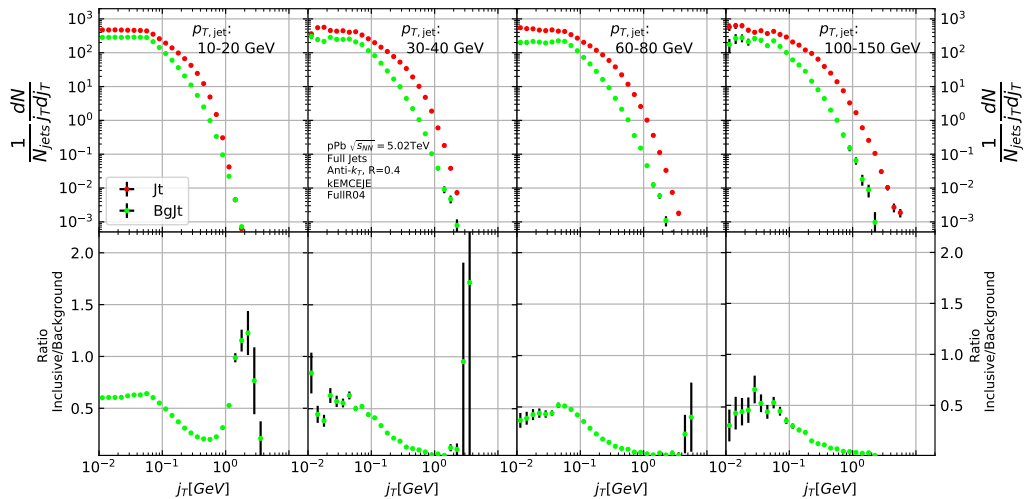


Figure 35: Inclusive j_T with background

1543 It is commonly interpreted as a transverse kick with respect to the initial hard
 1544 parton momentum that is given to a fragmenting particle during the fragmentation
 1545 process, which is a measure of the momentum spread of the jet fragments [].

1546 The reconstructed jet axis is used for j_T reference. Any charged track within
 1547 a fixed cone with radius R is taken as a jet constituent, as opposed to using the
 1548 constituent list provided by the jet algorithm. Anti- k_T produces jets that are
 1549 very circular in shape. Thus this doesn't change the constituent list considerably.
 1550 Neutral tracks are used only in jet reconstruction.

1551 Results of the raw inclusive j_T distribution in four $p_{\text{T},\text{jet}}$ bins with background
 1552 are shown in figure 35. Background is further discussed in Sec. 4.4

Resulting j_T distributions are shown as

$$\frac{1}{j_T} \frac{dN}{dj_T} \quad (41)$$

distributions. The logic behind this is that j_T is inherently a two-dimensional observable, comprised of j_{Tx} and j_{Ty} components. So the actual physical observable would be

$$\frac{d^2N}{dj_{Tx} dj_{Ty}} \quad (42)$$

Changing into polar coordinates with $j_{Tr} = j_T$ and θ gives

$$\frac{d^2N}{j_T dj_T d\theta}, \quad (43)$$

where j_T over the azimuth θ should stay constant and it can be integrated over, which gives

$$\frac{1}{2\pi} \frac{dN}{j_T dj_T}. \quad (44)$$

4.3 Unfolding detector effects

The raw inclusive j_T distributions are corrected for the detector inefficiency with an unfolding procedure. The procedure uses response matrices obtained from a PYTHIA [171] simulation.

Measured distributions are affected by two main factors; Limited acceptance - The probability to observe a given event is less than one and limited resolution - Quantity x cannot be determined exactly, but there is a measurement error. True $f(x)$ and measured $g(y)$ distributions are connected by a convolution integral. Including statistical fluctuations this becomes

$$\hat{g}(y) = \int_a^b A(y, x) f(x) dx + \epsilon(y), \quad (45)$$

where A is the detector response obtained by (for example) Monte Carlo simulations and $\epsilon(y)$ is the term coming from statistical fluctuations. If x and y are discrete variables we have

$$\hat{g}_i = \sum_{j=1}^m A_{ij} f_j + \epsilon_i, \quad (46)$$

where i and j give the j_T bins in the true and measured distributions. f_j and g_i give the counts in these bins. Or in matrix form

$$\hat{g} = Af + \epsilon, \quad (47)$$

1574 where \hat{g} and f are vectors corresponding to the measured and true histograms. If
 1575 the only detector effect is limited acceptance, A is a diagonal matrix, i.e. $A_{ij} =$
 1576 0 for $i \neq j$. We want to deduce the true distribution f , when the measured
 1577 distribution g is known. In a general discrete case the (naive) solution is obtained
 1578 by the inverse matrix

$$\hat{f} = A^{-1}\hat{g} \quad (48)$$

1579 However this usually leads to oscillating solutions and determining the inverse
 1580 matrix can be difficult.

1581 Two common methods to perform this inversion are Bayesian and SVD unfold-
 1582 ing methods. Often the solution requires some additional *a priori* information.
 1583 For example the solution should be smooth in most cases.

1584 4.3.1 Bayesian unfolding

The bayesian (iterative) method is based on the Bayes formula [].

$$P(C_i|E_j) = \frac{P(E_j|C_i) P_0(C_i)}{\sum_{l=1}^{n_C} P(E_j|C_l) P_0(C_l)},$$

1585 i.e. the probability of Cause C_i ("truth") given Effect E_j ("observed") is propor-
 1586 tional to the probability of observing E_j given C_i , $P(E_j|C_i)$ (response matrix) and
 1587 the true distribution $P_0(C_i)$.

In the unfolding procedure P_0 is given some starting distribution, either a uniform distribution or some guess of the final distribution. Taking into account the inefficiency this gives

$$\hat{n}(C_i) = \frac{1}{\epsilon_i} \sum_{j=1}^{n_E} n(E_j) P(C_i|E_j),$$

where

$$P(C_i|E_j) = \frac{P(E_j|C_i) P_0(C_i)}{\sum_{l=1}^{n_C} P(E_j|C_l) P_0(C_l)},$$

1588 and

$$\hat{n}(C_i) = \frac{1}{\epsilon_i} \sum_{j=1}^{n_E} n(E_j) P(C_i|E_j). \quad (49)$$

1589

First $P(C_i|E_j)$ is calculated with the uniform distribution or best guess of the shape of the distribution. This is then used to calculate the new distribution $\hat{P}(C_i)$

$$\hat{N}_{true} = \sum_{i=1}^{n_C} \hat{n}(C_i), \quad \hat{P}(C_i) = P(C_i|n(E)) = \frac{\hat{n}(C_i)}{\hat{N}_{true}}$$

1590 P_0 is then replaced with \hat{P} and the procedure is repeated until an acceptable
1591 solution is found.

1592 The bayesian procedure alongside with the SVD unfolding method are imple-
1593 mented in the RooUnfold package [172], which is used to perform the unfolding in
1594 practice. In RooUnfold the number of iterations is given beforehand. In practice
1595 this requires some trial and error. The number of iterations should be as low as
1596 possible, as the errors increase when going further in the iterations, but the number
1597 of iterations must be high enough so that the correct distribution is extracted.

1598 Error propagation in the Bayesian procedure

1599 The measured distribution has some statistical uncertainty, this should be reflected
1600 in the unfolded distribution. Additionally the response matrix may have some
1601 uncertainty if the statistics used in the Monte Carlo simulation were limited.

1602 For errors originating from the measured distribution RooUnfold uses the error
1603 propagation matrix

$$\frac{\partial \hat{n}(C_i)}{\partial n(E_j)} = M_{ij} + \frac{\hat{n}(C_i)}{n_0(C_i)} \frac{\partial n_0(C_i)}{\partial n(E_j)} - \sum_{k=1}^{n_E} \sum_{l=1}^{n_C} \frac{n(E_k) \epsilon_l}{n_0(C_l)} M_{ik} M_{lk} \frac{\partial n_0(C_l)}{\partial n(E_j)}, \quad (50)$$

1604 where $\hat{n}(C_i)$ is the unfolded result from Eq. 49. This depends upon the matrix
1605 $\frac{\partial n_0(C_i)}{\partial n(E_j)}$, which is $\frac{\partial \hat{n}(C_i)}{\partial n(E_j)}$ from the previous iteration. In the first iteration, $\frac{\partial n_0(C_i)}{\partial n(E_j)} = 0$
1606 and $\frac{\partial \hat{n}(C_i)}{\partial n(E_j)} = M_{ij}$.

1607 The error propagation matrix V is used to obtain the covariance matrix on the
1608 unfolded distribution

$$V(\hat{n}(C_k), \hat{n}(C_l)) = \sum_{i,j=1}^{n_E} \frac{\partial \hat{n}(C_k)}{\partial n(E_i)} V(\hat{n}(E_i), \hat{n}(E_j)) \frac{\partial \hat{n}(C_l)}{\partial n(E_j)}, \quad (51)$$

1609 where $V(\hat{n}(E_i), \hat{n}(E_j))$ is the covariance matrix of the measurements. In count-
1610 ing experiments common in particle physics, each bin is independently Poisson
1611 distributed, with

$$V(\hat{n}(E_i), \hat{n}(E_j)) = n(E_i) \delta_{ij} \quad (52)$$

1612 The error propagation matrix for the response matrix is

$$\begin{aligned} \frac{\partial \hat{n}(C_i)}{\partial P(E_j|C_k)} &= \frac{1}{\epsilon_i} \left(\frac{n_0(C_i) n(E_j)}{f_j} - \hat{n}(C_i) \right) \delta_{ik} - \frac{n_0(C_k) n(E_j)}{f_j} M_{ij} + \\ &\quad \frac{\hat{n}(C_i)}{n_0(C_i)} \frac{\partial n_0(C_i)}{\partial P(E_j|C_k)} - \frac{\epsilon_i}{n_0(C_i)} \sum_{l=1}^{n_E} \sum_{r=1}^{n_C} n(E_l) M_{il} M_{rl} \frac{\partial n_0(C_r)}{\partial P(E_j|C_k)}, \end{aligned} \quad (53)$$

where $\frac{\partial n_0(C_i)}{\partial P(E_j|C_k)}$ is the error propagation matrix from the previous iteration, $\frac{\hat{n}(C_i)}{\partial P(E_j|C_k)}$. For the first iteration, this is zero and the final two terms in Eq. 53 disappear.

The covariance matrix due to these errors is given by

$$V(\hat{n}(C_k), \hat{n}(C_l)) = \sum_{j,s=1}^{n_E} \sum_{i,r=1}^{n_C} \frac{\partial \hat{n}(C_k)}{\partial P(E_j|C_i)} V(P(E_j|C_i), P(E_s|C_r)) \frac{\partial \hat{n}(C_l)}{\partial P(E_s|C_r)}, \quad (54)$$

where $V(P(E_j|C_i), P(E_s|C_r))$ can be taken as multinomial, Poisson or other distribution.

4.3.2 Toy Monte Carlo

remove / move to appendix? A toy Monte Carlo simulation was performed to see the performance of unfolding in an ideal case. The simulations samples jet p_T values from the observed p_T distribution. Starting from this p_T the simulations starts creating tracks with

$$p_{\text{track}} = z_{\text{track}} p_{T\text{jet}} \quad (55)$$

where z_{track} is sampled from the observed z distribution. All tracks below 0.15 GeV are discarded. Sampling is continued until the sum of the track transverse momenta exceeds the jet transverse momentum. Jet is then defined as the sum of the track momenta.

Simultaneously a p_T dependant observation efficiency is applied to the tracks and a separate observed jet is calculated using only the observed tracks. Additionally a set of fake tracks is added to the observed jet. Tracks are always either observed or not at the true momentum. No smearing is added to the observed momentum.

Afterwards the tracks are looped over for j_T calculation. For observed tracks we calculate j_T with respect to both the true jet axis and the observed jet. 2D Response matrix is filled with

$$(j_T^{\text{obs}}, p_{T\text{jet}}^{\text{obs}}, j_T^{\text{true}}, p_{T\text{jet}}^{\text{true}}) \quad (56)$$

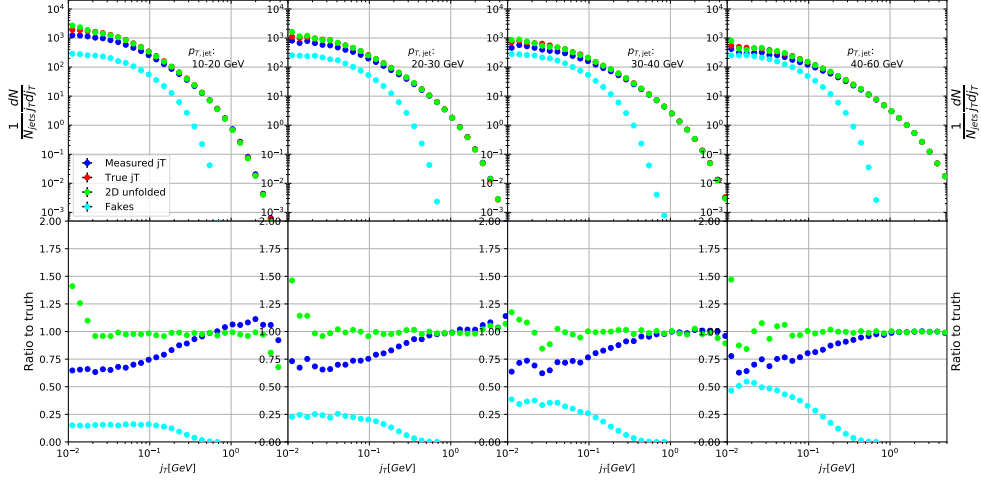


Figure 36: Results from unfolding in Toy Monte Carlo

1636 In practice this is done with a set of 3D histograms, where $p_{T,\text{jet},\text{true}}$ determines
 1637 the histogram index and the remaining three values the bin in the 3D histogram.

1638 After creating the response matrices, an identical procedure is carried out to
 1639 the create testing data. Now instead of filling response matrices, 2D histograms
 1640 are filled with $(j_T^{\text{obs}}, p_{T,\text{jet}}^{\text{obs}})$ and $(j_T^{\text{true}}, p_{T,\text{jet}}^{\text{true}})$

1641 The observed distributions are unfolded using RooUnfold's 2D Bayesian (iter-
 1642 ative) algorithm. Results are shown in figure 36. Aside from some discrepancy at
 1643 very low j_T the true distribution is retrieved well.

1644 4.3.3 Pythia Response matrices

1645 A PYTHIA6 simulation was carried out to determine the response matrices. [Details](#)
 1646 of the simulation

1647 Response matrices are filled through correlation between MC detector and
 1648 particle level jets and tracks.

1649 The ranges of both j_T and $p_{T,\text{jet}}$ extend the ranges in end results. These are
 1650 shown in Tab. 5. The ranges are the same in detector and particle level.

1651 When calculating j_T for MC particles the code checks whether a corresponding
 1652 detector level track exists and if that track had a j_T value. Additionally the code
 1653 checks for detector level tracks that don't have corresponding particle level track
 1654 with a j_T value.

1655 There are several possibilities that have to be taken into account:

- 1656 • We find a corresponding track with a j_T value, response matrix is filled
 1657 normally with $(j_T^{\text{obs}}, p_{T,\text{jet}}^{\text{obs}}, j_T^{\text{true}}, p_{T,\text{jet}}^{\text{true}})$

Table 5: j_T and p_T ranges used in unfolding. The same ranges are used for detector and truth level.

	j_T	$p_{T\text{jet}}$
Min	0.01	5
Max	20	500

- We don't find a corresponding track. Record $(j_T^{\text{true}}, p_{T\text{jet}}^{\text{true}})$ as a miss
- We find a corresponding track, but it didn't have j_T value. Most likely because it was not part of a jet in the detector level set. Similary record $(j_T^{\text{true}}, p_{T\text{jet}}^{\text{true}})$ as a miss
- For detector level tracks that have no correspondence in particle level set the code records $(j_T^{\text{obs}}, p_{T\text{jet}}^{\text{obs}})$ as a fake

In the analysis code the response matrix is made of an array of 3 dimensional histograms, with $(j_T^{\text{obs}}, p_{T\text{jet}}^{\text{obs}}, j_T^{\text{true}})$ as axes. The histogram index gives the $p_{T\text{jet}}^{\text{true}}$ value.

4.3.4 Unfolding algorithm

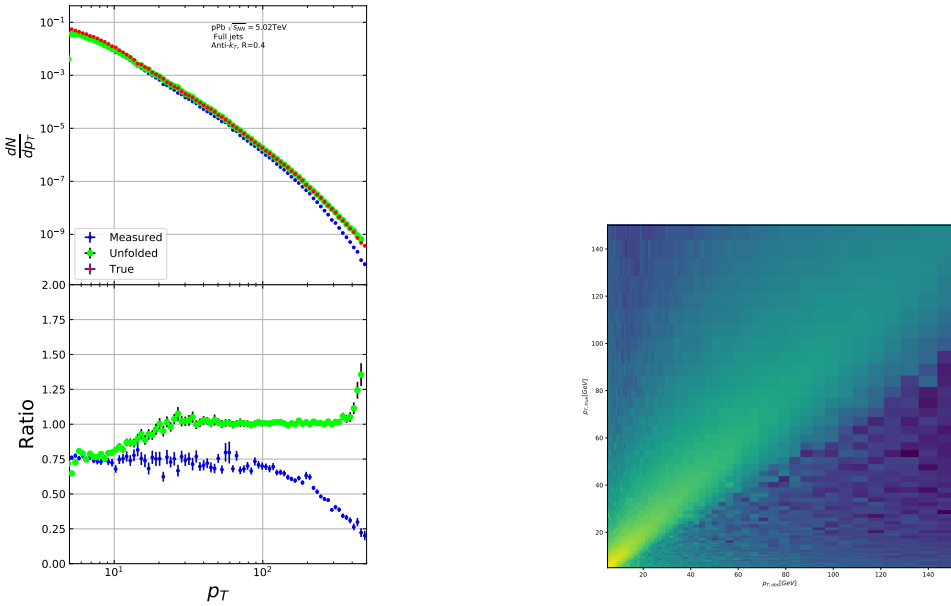
As a primary method unfolding is performed with an iterative (bayesian) algorithm using the RooUnfold [172] package. The number of iterations used is 4. The default ranges of j_T and $p_{T\text{jet}}$ are shown in 5. As a default the true j_T distribution from the PYTHIA simulation is used as the prior.

4.3.5 Unfolding closure test

The PYTHIAset is divided into 2 halves. First is used to fill the response matrices, as well as record missed and fake tracks. Second half is used to test the effectiveness of the unfolding method. Jet p_T distributions are shown in figure 37a and response matrix are shown in figure 37b.

Response matrices within single jet p_T bins are shown in figure 38. Results from the closure test are shown in figure 39. In the lowest jet p_T bins unfolding fails to recover the true distribution. The lowest jet p_T bins are dominated by combinatorial jets and thus the true detector response is likely not retrieved.

Above $30 \text{ GeV} < p_{T\text{jet}} < 40 \text{ GeV}$ the distribution is recovered well in the mid j_T region. At $j_T < 0.1 \text{ GeV}$ there is clear discrepancy. The final results are shown only for $j_T > 0.1 \text{ GeV}$. Additionally there is some discrepancy at very high j_T . This is taken into account in the unfolding systematics. (TODO: Show this)



(a) Unfolded jet p_T distribution in PYTHIA closure test
(b) Jet p_T response matrix from unfolding closure test

Figure 37: Jet p_T in unfolding closure test

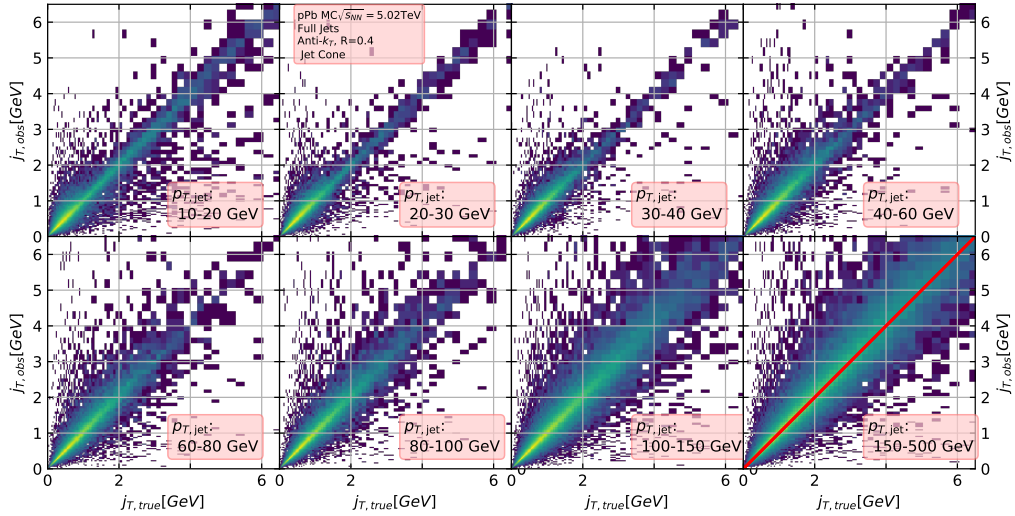


Figure 38: j_T Response matrices in individual $p_{T,jet}$ bins

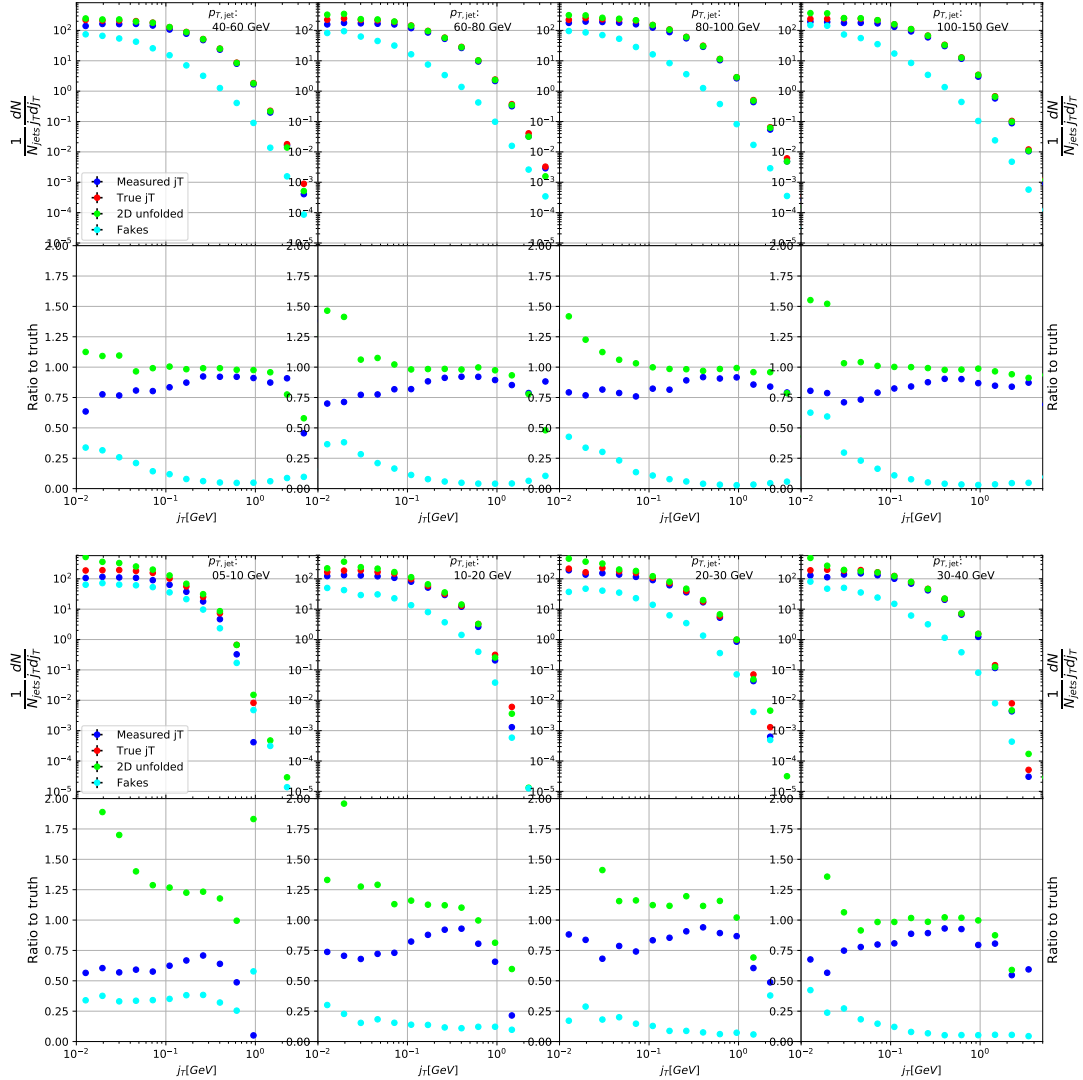


Figure 39: Pythia closure test results. Fake tracks include also tracks that do exist in the true dataset, but for one reason or another were not given j_T values. j_T is only calculated for tracks that are associated with jets

1685 4.4 Background

1686 When calculating j_T distributions for jet constituents there is a contribution from
 1687 the underlying event (UE), i.e. tracks that just happen to be close to the jet axis.
 1688 To find the signal coming from the actual jet we need to subtract the background
 1689 (UE) contribution. On a jet-by-jet basis this is impossible, so one must estimate
 1690 the background contribution in the inclusive distribution. A schematic view of the
 1691 background contribution is shown in Fig. 40.

1692 We have two methods for background estimation. In the first we look at the
 1693 direction perpendicular to the jet. This is assumed to be the region least likely to
 1694 contain jet contributions. In the second method we randomly assign the tracks of
 1695 event new ϕ and η values. The result is thus guaranteed to be uncorrelated.

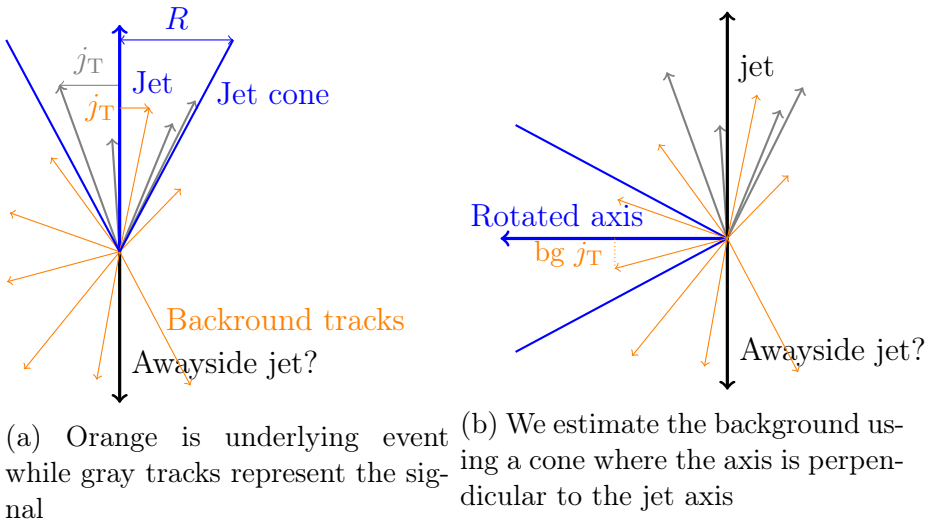


Figure 40: Background estimation

1696 4.4.1 Perpendicular cone background

1697 As a primary method to estimate the background we look at regions of the detector
 1698 where there are no tracks from jets, but only uncorrelated tracks from the under-
 1699 lying event. The underlying event is thus estimated by looking at an imaginary
 1700 jet cone perpendicular to the observed jet axis ($\frac{\pi}{2}$ Rotation in ϕ).

1701 After calculating the j_T values for tracks in the jet, we rotate the jet axis by $\frac{\pi}{2}$
 1702 in positive ϕ direction. We check that there are no other jets closer than $2R$ to the
 1703 rotated axis. Otherwise background calculation is skipped for this jet. Probability
 1704 of this happening is 1-2% depending on the jet p_T bin.

1705 If we don't find other jets in the vicinity we move on to estimate the background.
 1706 We find all tracks within a cone of radius R around the rotated axis and calculate
 1707 j_T of these tracks with respect to the rotated axis. Auto-correlations are discussed
 1708 in Sec. 4.4.3.

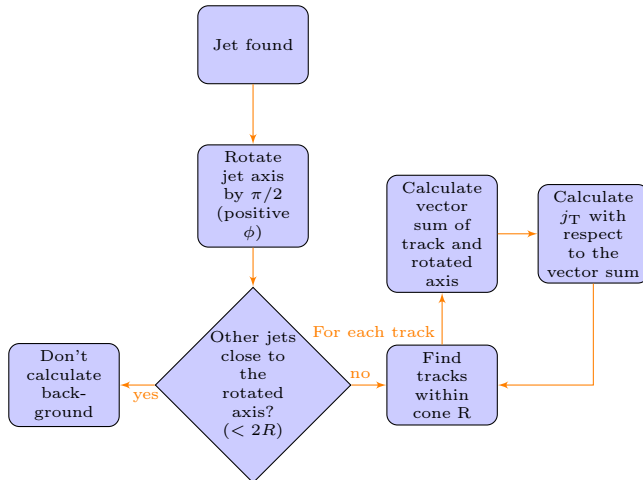


Figure 41: Flowchart representation of the perpendicular cone background procedure

1709 4.4.2 Random background

1710 In the random background method we look at all tracks in the event, except for
 1711 tracks close to jets found by the jet algorithm. We randomly assign new η and ϕ
 1712 values to all tracks using uniform distributions with $|\eta| < 1.0$. p_T values are kept
 1713 the same. To increase statistics there is a possibility to create a number of random
 1714 tracks for each actual track. In the analysis we do this 10 times for each track.
 1715 Again the track p_T value is kept the same.

1716 We create a random jet cone from uniform η and ϕ distributions. Here $|\eta| <$
 1717 0.25. Now we calculate j_T of the random tracks with respect to the random cone
 1718 axis. Auto-correlations are added before calculating j_T (see 4.4.3).

1719 4.4.3 Auto-correlations

1720 Jet axis is simply a vector sum of all its constituents. Thus having an additional
 1721 track in the jet from the underlying event moves the jet axis towards this track.
 1722 Since the axis is now closer to the track, it has a smaller j_T value. Assuming a
 1723 1 GeV background track at the edge of a $R = 0.4$ cone the j_T value would be
 1724 0.4 GeV. If this is added to a 5 GeV jet, the j_T value becomes 0.33 GeV after the

jet axis moves. In a 50 GeV jet it would be 0.39 GeV. This is a region where the inclusive j_T distribution is dominated by background. The distribution is also steeply falling. Overestimating the background can lead to a situation where the background estimation exceeds the inclusive distribution.

To take this effect into account we can't use a fixed axis for background, but it has to behave like a jet would when additional tracks are added. Thus before calculating j_T values we make a vector sum of the track and the axis used for background, which is either the perpendicular cone axis or the random axis depending on the background method. In each case the momentum of this background axis is assumed to be the same as the jet which initiated the background estimation.

In pPb data there is on average about one underlying event track in a $R = 0.4$ cone. If there would be more, one should consider taking the vector sum of all tracks inside the cone. As there is usually only one track and if there are more it's unlikely that more than one has high momentum, taking the vector sum track-by-track should be enough.

4.4.4 Comparing background methods

Comparison between perpendicular cone and random background in figure 42. The advantage of the random background method is the added amount of statistics as the procedure can be repeated several times for each event. However, it seems that, especially in the highest $p_{T\text{jet}}$ bins there is some jet contribution left at the high end. Naturally there is no correlation between the tracks and the background axis, but if some high momentum tracks originating from jets were not subtracted and happen to hit the edge of the background cone, they can increase the high j_T yield in the background estimation.

One should note that the results from perpendicular cone background show no observable change between $p_{T\text{jet}}$ bins. It is a good indication that the background is actually dominated by the underlying event over the entire j_T region.

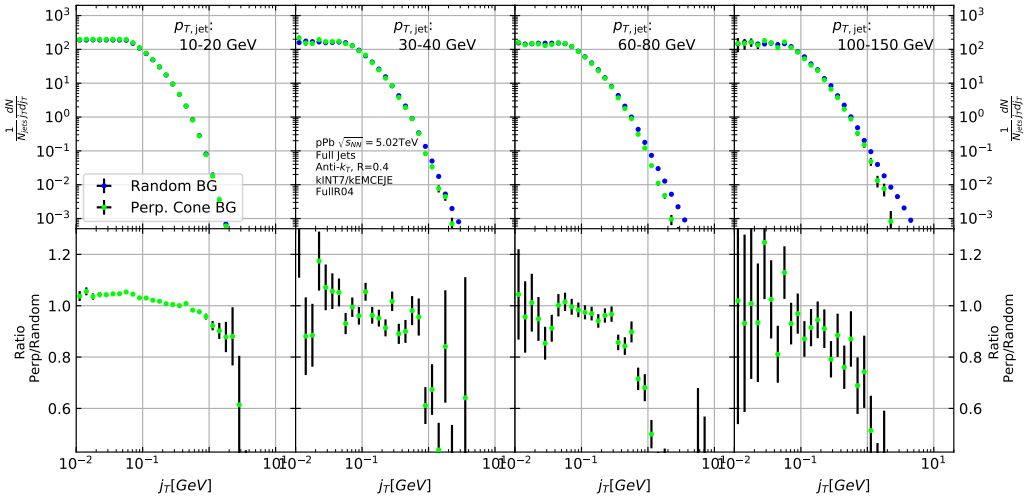


Figure 42: j_T background with two different methods

1752 4.5 Fitting

1753 After unfolding and background subtraction the resulting signal distributions are
 1754 fitted with a 2 component function shown in Eq. 57. Gaussian distribution is used
 1755 for low j_T and an inverse gamma function is used for high j_T . The gaussian is
 1756 taken to have the center at $j_T = 0$. In total this gives 5 parameters. The fitting
 1757 procedure was inspired by the dihadron j_T analysis by ALICE [2]. The complete
 1758 fitting function is

$$\frac{1}{N_{\text{jets}} j_T \text{d}j_T} \frac{\text{d}N}{\text{d}j_T} = \frac{B_2}{B_1 \sqrt{2\pi}} e^{-\frac{j_T^2}{2B_1^2}} + \frac{B_3 B_5^{B_4}}{\Gamma(B_4)} e^{-\frac{B_5}{j_T^{B_4+1}}}. \quad (57)$$

1759 To achieve stable results the fitting is performed in two steps. First both
 1760 components are fitted separately. Gaussian component is fitted to the low end of
 1761 j_T . Inverse gamma component is fitted to j_T above 1 GeV/c. After getting the
 1762 results from the individual fits they are combined into a single function with initial
 1763 values from the individual results and an additional fit is performed.

1764 After getting the fit function $\sqrt{\langle j_T^2 \rangle}$ (RMS) and yield values are extracted
 1765 separately from each component. The narrow component RMS is

$$\sqrt{\langle j_T^2 \rangle} = \sqrt{2} B_1,$$

1766 and the wide component RMS value is calculated as

$$\sqrt{\langle j_T^2 \rangle} = \frac{B_5}{\sqrt{(B_4 - 2)(B_4 - 3)}},$$

₁₇₆₇ where it is required that $B_4 > 3$.

₁₇₆₈ The statistical errors can be calculated with the general error propagation
₁₇₆₉ formulas. As a result one gets errors for the narrow component RMS

$$\delta \sqrt{\langle j_T^2 \rangle} = \sqrt{2} \delta B_1 \quad (58)$$

₁₇₇₀ and for the wide component RMS

$$\delta \sqrt{\langle j_T^2 \rangle} = \sqrt{\left(\frac{(5 - 2B_4) B_5 \delta B_4}{(2(B_4 - 2)(B_4 - 3))^{\frac{3}{2}}} \right)^2 + \left(\frac{\delta B_5}{\sqrt{(B_4 - 2)(B_4 - 3)}} \right)^2} \quad (59)$$

1771 5 Systematic errors

1772 Extend Systematics The main systematic uncertainties in this analysis come from
1773 the background estimation, the unfolding procedure and uncertainty in the track-
1774 ing efficiency.

1775 The systematics in background estimation were studied using an alternative
1776 method to extract the background, the random background method.

1777 The systematic uncertainty that arises from the unfolding procedure is esti-
1778 mated by performing the unfolding with two separate methods. Data corrected
1779 by the iterative unfolding method are used as the results and the SVD unfolding
1780 method is employed to estimate the uncertainty. In a PYTHIA closure test the
1781 true distribution was in general found to be between the unfolded distributions
1782 from the iterative and SVD method. The difference between the methods when
1783 unfolding data should give a reasonable estimate of the unfolding uncertainty. The
1784 resulting uncertainty is below 8% for both wide and narrow component RMS.

1785 5.1 Background

1786 The uncertainty coming from background estimation is estimated by subtracting
1787 the background separately for the perpendicular cone and random background
1788 methods. Comparisons of the resulting signal distributions are shown in Fig. 43.

1789 Fits are then performed on both perpendicular cone and random background
1790 signals. Difference between them is taken as the systematic error. The fits for
1791 individual bins from the random background method are shown in figure 44. Re-
1792 sulting differences between the methods for different components are shown in
1793 figure 45. The dotted lines are put at $\pm 5\%$ for the narrow component and at
1794 $\pm 8\%$ for the wide component. These are taken as systematic estimates for the
1795 entire $p_{T\text{jet}}$ range.

1796 5.2 Unfolding

1797 Unfolding is the second major source of systematic uncertainty. To estimate the
1798 uncertainty related to the unfolding procedure several checks are performed. The
1799 main systematic uncertainty estimation comes from comparing results performed
1800 using both SVD and Bayesian unfolding. Difference between the methods is taken
1801 as the systematic error. Since SVD unfolding does not have a 2 dimensional
1802 options, the unfolding is done bin by bin. The resulting distributions after SVD
1803 unfolding and background subtraction with the perpendicular cone method are
1804 shown in fig 46.

1805 As in the background systematic estimation, fits are performed for both cases
1806 separately. Resulting differences between the methods for different components

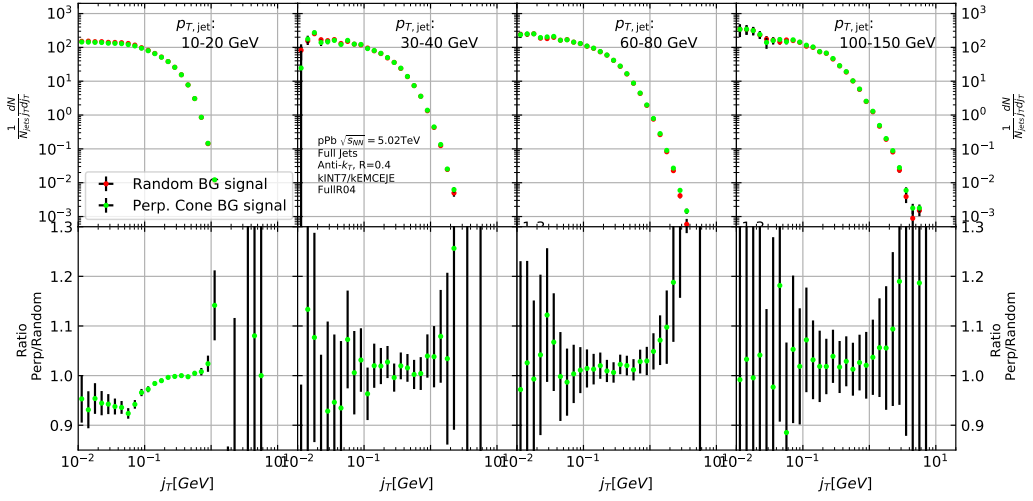


Figure 43: Comparison of the effect of background method on j_T signal.

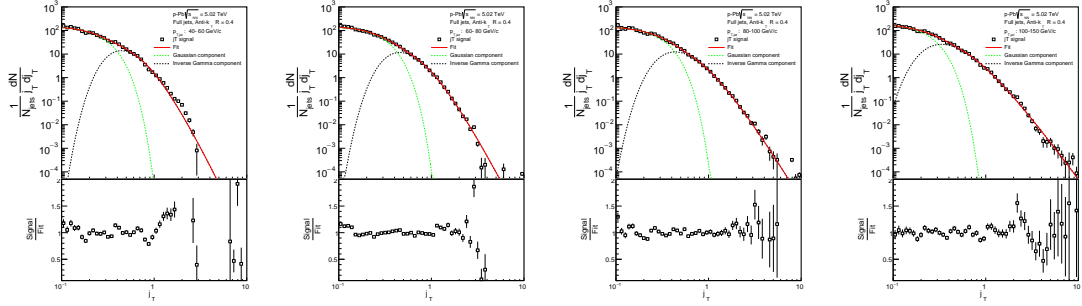


Figure 44: j_T signal with random background subtraction fits in different jet p_T bins

are shown in figure 47. The dotted lines are at $\pm 8\%$ for both components. These are taken to be the systematic uncertainty related to unfolding.

Several other systematic checks were performed with the Bayesian unfolding procedure. They are described in the following sections. As these are small compared to the main uncertainty they are not included separately.

5.2.1 Effect of number of iterations

The iterative unfolding algorithm permits the change of number of iterations. The unfolding procedure was carried out using different numbers of iterations. The results from these different cases are shown in Fig. 48. The results are compared to the default unfolding algorithm with 4 iterations. The difference in results

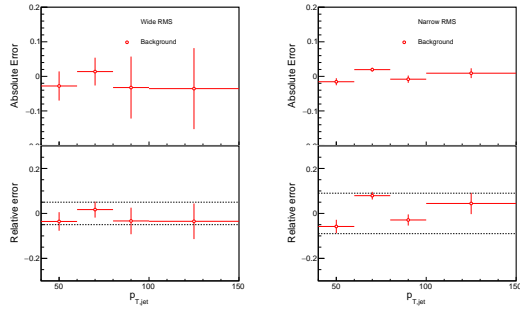


Figure 45: Differences between perpendicular cone and random background subtraction in the resulting RMS values.

Figure 46: Resulting signal distributions from SVD unfolding with the perpendicular cone background methods. These are compared to the results from the Bayesian algorithm to estimate the systematic uncertainty.

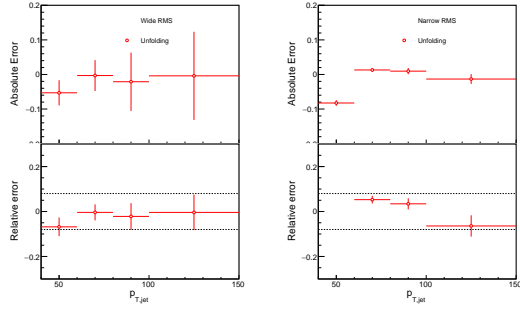


Figure 47: Differences between Bayesian and SVD unfolding in the resulting RMS values

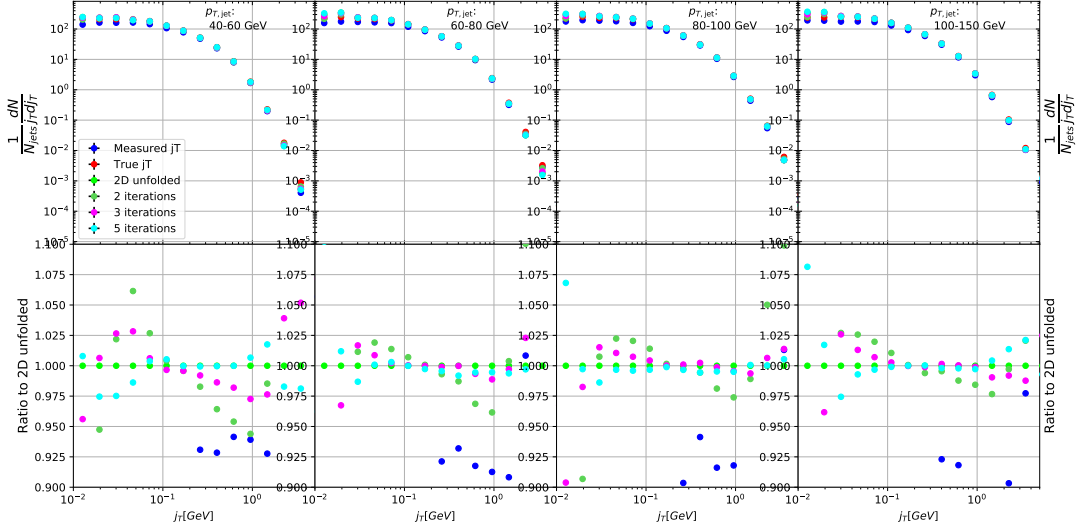


Figure 48: Unfolding with different number of iterations

Figure 49: Effect of changing prior from true distribution in PYTHIA to the unfolded distribution. [Missing figure](#)

1817 between the different cases is mostly less than 2.5%.

1818 5.2.2 Effect of different prior

1819 The iterative algorithm requires a prior estimate of the shape of the distribution.
 1820 As a default prior the truth (particle level) distribution is used. To test the effect
 1821 of changing the prior we instead use the unfolded j_T distribution as prior. The
 1822 results are compared to the unfolding algorithm with the default prior. This is
 1823 shown in Fig. 49. The difference in results between the different cases is mostly less
 1824 than 2.5%.

1825 5.2.3 Effect of p_T truncation

1826 As an additional check the unfolding is carried out with different $p_{T\text{jet}}$ truncation
 1827 values. By default the full range of $p_{T\text{jet}} > 5\text{GeV}$ is used. We test the unfolding
 1828 by only using the response matrix for $p_{T\text{jet}} > 10\text{GeV}$. The results of this test are
 1829 shown in Fig. 50. The effects are strongest in the lower $p_{T\text{jet}}$ bins. Also in this
 1830 case the difference is less than 2.5 % in all $p_{T\text{jet}}$ bins.

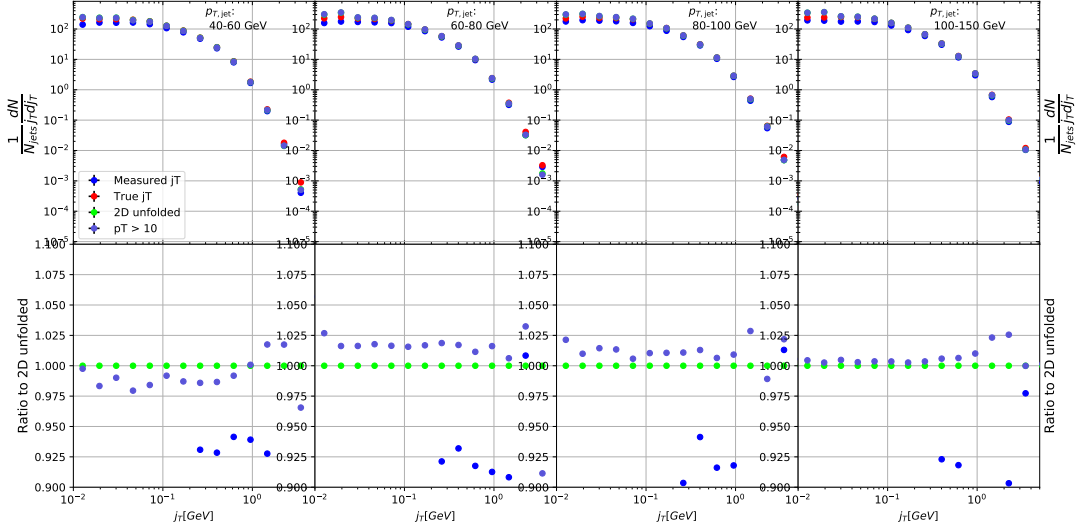


Figure 50: Effect of changing minimum jet p_T used in unfolding from 5 to 10 GeV

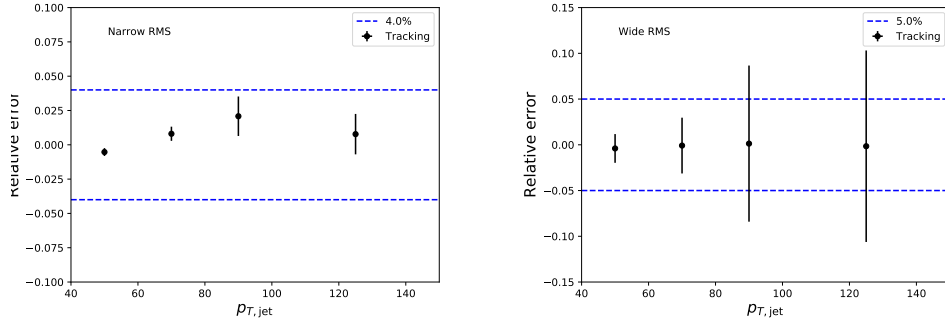


Figure 51: Relative systematic errors resulting from tracking efficiency uncertainty.

1831 5.3 Tracking

1832 Systematic effects originating from uncertainty in the tracking efficiency are es-
 1833 timated through a PYTHIA simulation, where an artificial inefficiency of 3% is
 1834 introduced i.e. 3 % of tracks are randomly removed from each event. The effect
 1835 of this artificial inefficiency is shown in Fig. 51. The systematic uncertainties as-
 1836 signed to tracking efficiency are 4 % for the narrow component and 5 % for the
 1837 wide component.

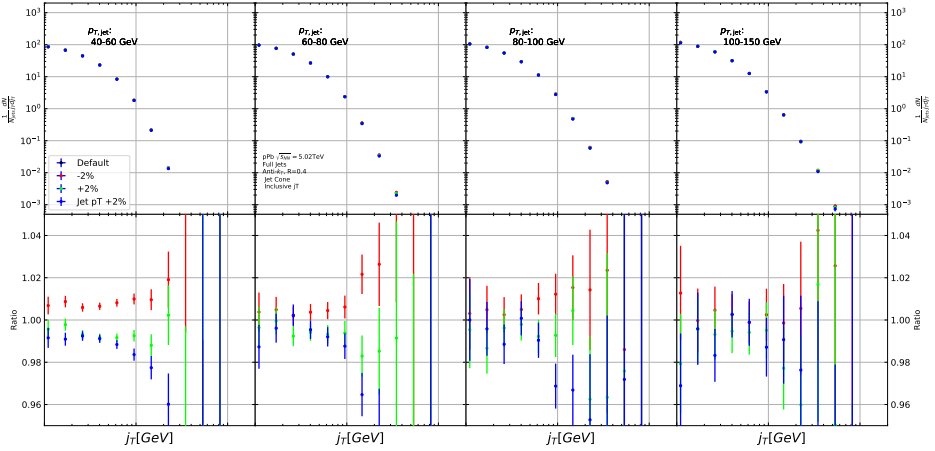


Figure 52: Results from PYTHIA simulations with Cluster energies scaled up and down by 2 %. Additionally jet momenta were scaled by 2 % when determining the jet p_T bin.

1838 5.4 EMCAL clusters

1839 The analysis uses EMCAL clusters only in the reconstruction of jets. Thus the only
 1840 way uncertainty in EMCAL performance can affect the results is through modifica-
 1841 tion of jet momentum or axis.

1842 Uncertainty related to the EMCAL energy scale was estimated by scaling cluster
 1843 energies up and down by 2 % in a PYTHIA particle level simulation. Similarly
 1844 the jet momentum was scaled by $\pm 2\%$ when determining the jet p_T bin. In the
 1845 analysis EMCAL is used only in jet reconstruction, not for calculating j_T . The only
 1846 ways EMCAL uncertainty can affect the analysis are changes in jet energy and jet
 1847 axis. Jet axis shouldn't significantly change, so the main contribution should be
 1848 changes in jet p_T bin.

1849 The resulting differences in the inclusive j_T distributions are shown in Fig. 52.
 1850 Qualitatively the effect of scaling cluster energies is the same as scaling the jet
 1851 energies.

1852 Like in the previous cases fits are performed for the unscaled case and for cases
 1853 with $\pm 2\%$ scaling. The resulting systematic uncertainties are shown in Fig. 53.
 1854 The uncertainty is taken to be 1% for both components.

1855 5.5 Summary/Combining systematics

1856 The different source of the systematic uncertainty are considered as uncorrelated
 1857 and the values of each source are summed in quadrature.

1858 Resulting systematic errors are shown in table 6. The different source of the

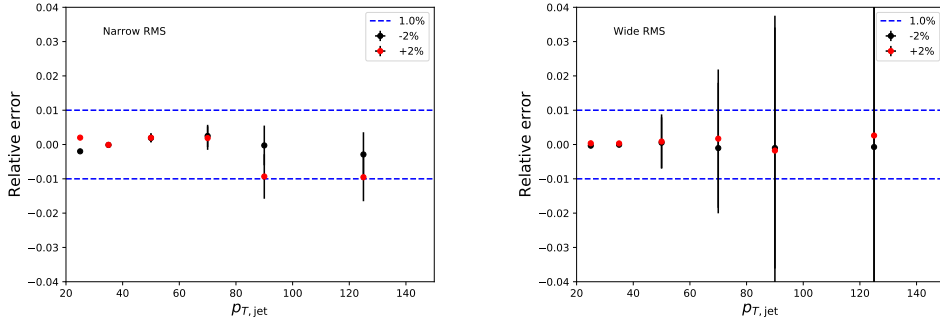


Figure 53: Relative systematic errors resulting from cluster energy uncertainty.

1859 systematic uncertainty are considered to be uncorrelated and are thus combined
1860 bin-by-bin in quadrature to get the total systematic errors. The resulting uncer-
1861 tainty is approximately 9 % for the wide component RMS and 12 % for the narrow
component RMS.

Table 6: Summary of systematic errors

Systematic	Wide RMS	Narrow RMS
Background	5 %	9 %
Unfolding	8 %	8 %
Tracking	4 %	5 %
EMCal	1 %	1 %
Total	10 %	13%

1862

1863 5.6 Additional checks

1864 5.6.1 Comparison between A and C side

1865 In 2013 there were issues with tracking. To rule out effects on j_T distributions
1866 a study was performed comparing j_T distributions between A and C side. (In
1867 the p-Pb configuration the proton beam is travelling from A to C) No systematic
1868 differences were observed. Figure 54 shows the comparison between inclusive dis-
1869 tributions between the different sides, both for minimum bias and EMCal triggered
1870 datasets.

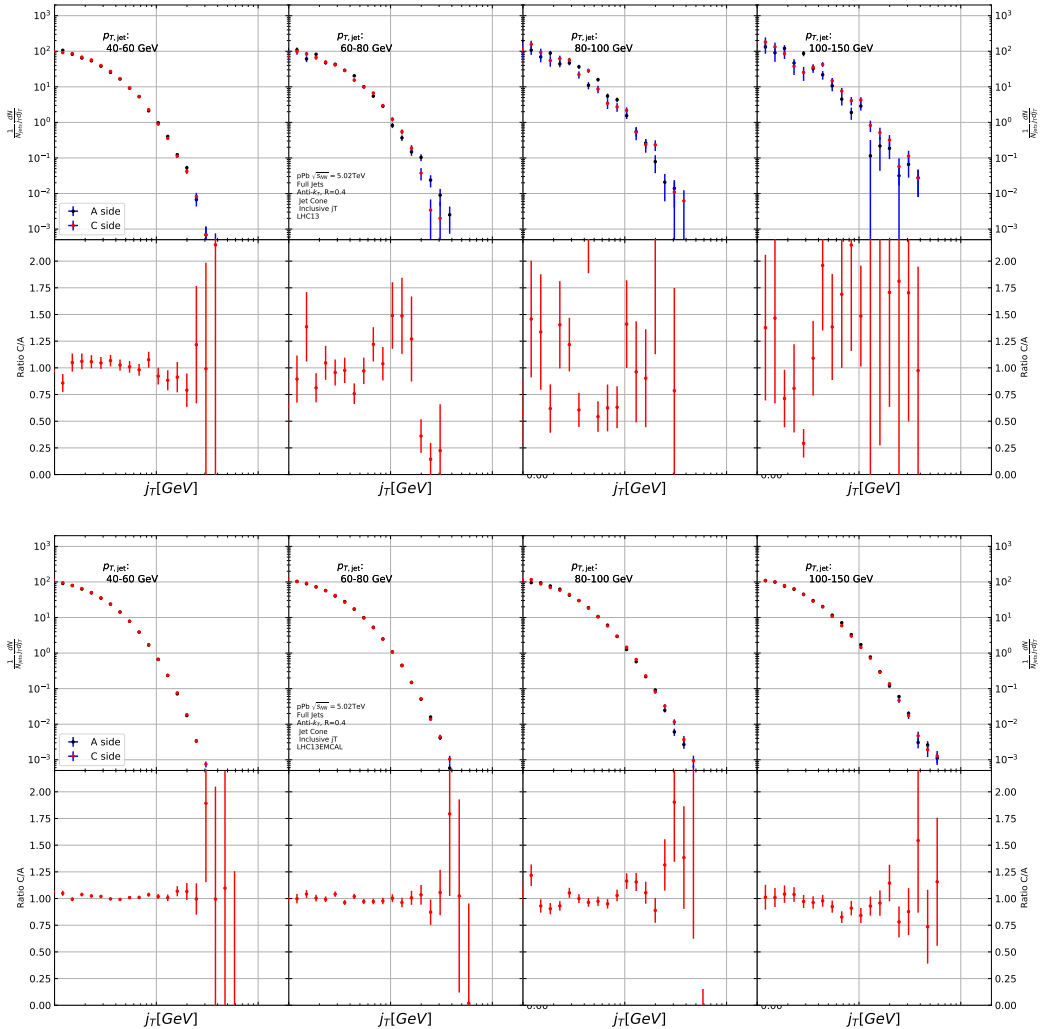


Figure 54: Comparison of inclusive j_T distributions between A and C side for minimum bias and EMCAL triggered data.

6 Results

6.1 Fitting

Fits of j_T distributions in different $p_{T\text{jet}}$ bins with $p_{T\text{jet}} > 40 \text{ GeV}$ are shown in figure 55. Additional $p_{T\text{jet}}$ bins are shown in appendix A. In lowest $p_{T\text{jet}}$ bins the jets are mainly combinatorial which makes background subtraction and unfolding difficult and thus the signal can't be trusted.

The fits describe the data well. There is some fluctuation of the order of 10 % around the fit function. At hight j_T the statistical errors in the signal are large.

6.1.1 RMS values from fitted distributions

RMS results with systematic errors are shown separately in figure 56. Figure 57 shows RMS values for both components combined. The figure also includes results from a PYTHIA simulation.

6.2 High multiplicity

The analysis was repeated taking only events with high multiplicity. Three different multiplicity cuts were used; 10 %, 1 % and 0.1 %. We used ZDC(TODO) as a centrality estimator. As argued in section 1.6.3 the zero-degree energy deposit should provide a centrality estimator with minimal bias from jets production. Resulting j_T distributions are shown Fig. 58. As the statistics are limited in the high multiplicity runs, it was hard to achieve stable fits to the distributions. Thus the RMS values are not shown.

From the figure one can observe no systematic modification when tighter multiplicity cuts are introduced.

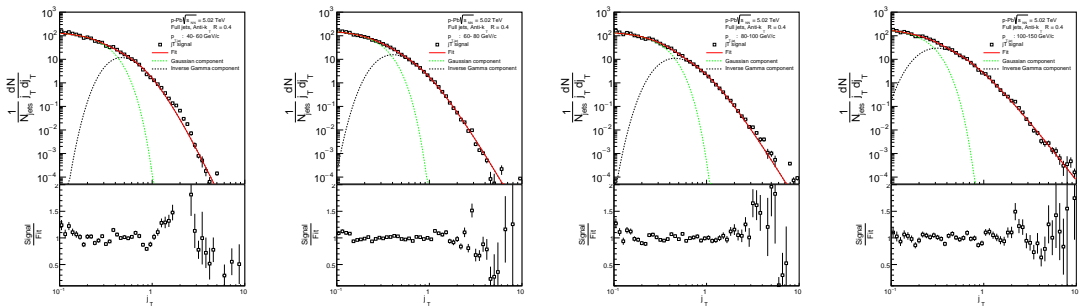


Figure 55: j_T signal fits in different jet p_T bins

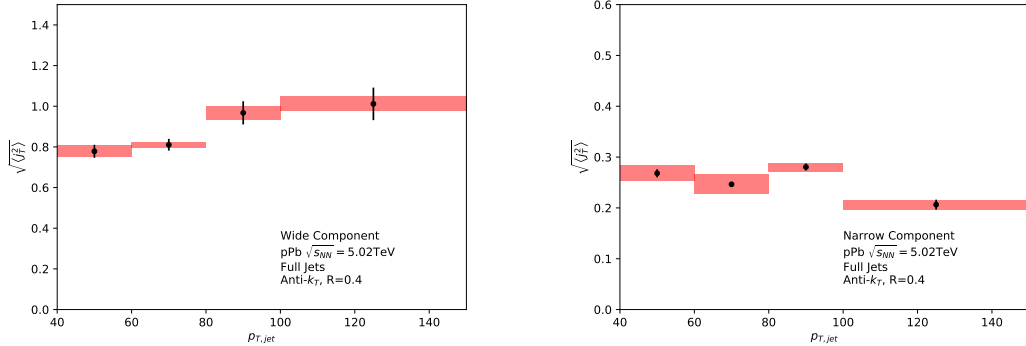


Figure 56: RMS values extracted from the fits for the gaussian (narrow) and inverse gamma (wide) components

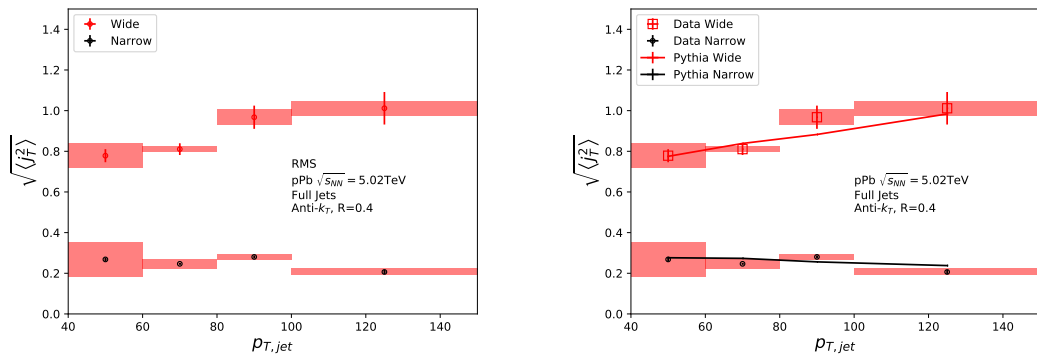


Figure 57: RMS values extracted from the fits for the gaussian (narrow) and inverse gamma (wide) components

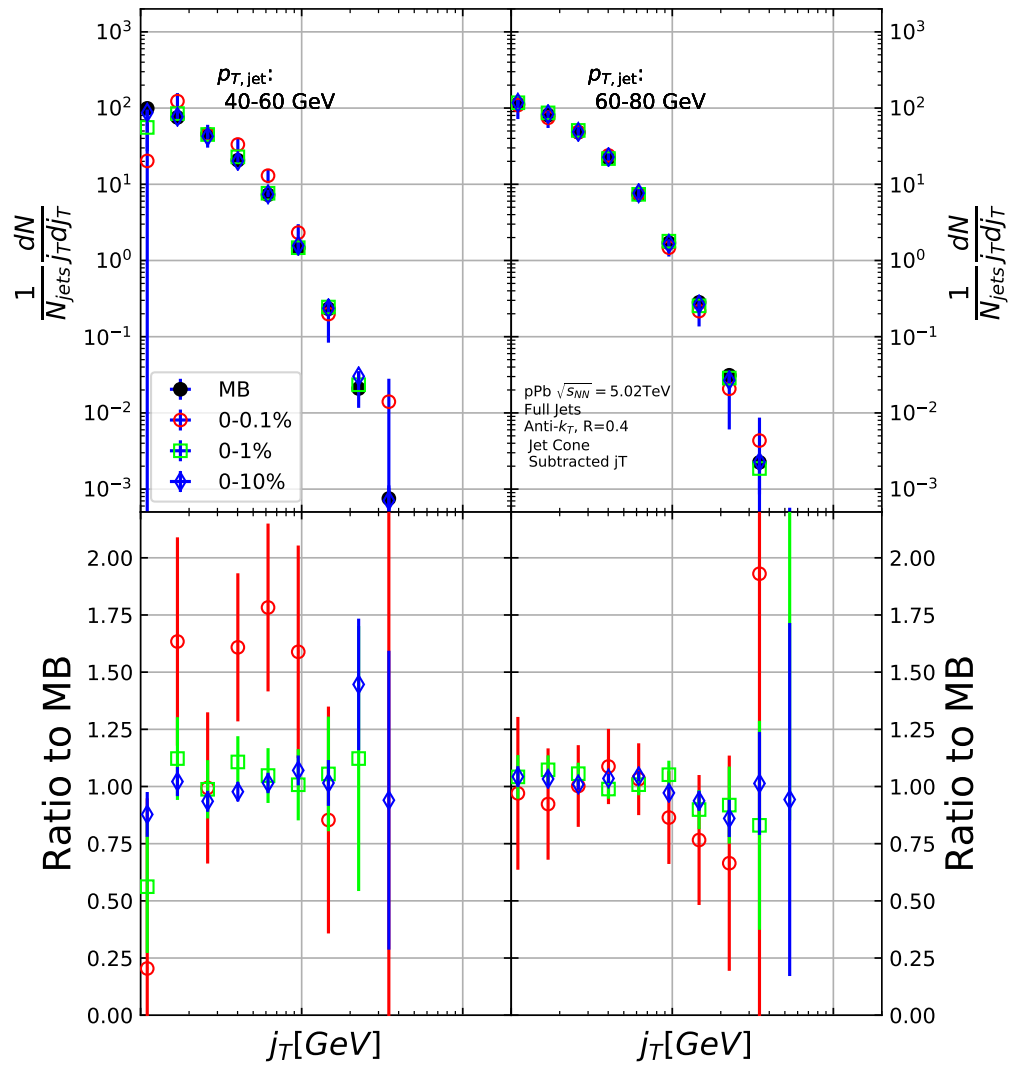


Figure 58: j_T distributions for high multiplicity p–Pb events. Replace figure

¹⁸⁹³ **7 Discussion**

¹⁸⁹⁴ [173, 174]

¹⁸⁹⁵ **7.1 Dihadron j_T**

¹⁸⁹⁶ The jet fragmentation transverse momentum j_T has been studied previously at
¹⁸⁹⁷ ALICE with dihadron correlations [2]. The study took the leading hadron in
¹⁸⁹⁸ each event and calculated j_T for any near-side tracks with respect to the leading
¹⁸⁹⁹ hadron. Thus there is no kinematical limit to j_T from the jet cone. In the analysis
¹⁹⁰⁰ the background shape is estimated using pairs with large $\Delta\eta$. The normalisation of
¹⁹⁰¹ the background is done when fitting the j_T distribution. The inclusive and signal
¹⁹⁰² distributions from the analysis are shown in Fig. 59. The inclusive distribution is
¹⁹⁰³ fitted with a three component function,

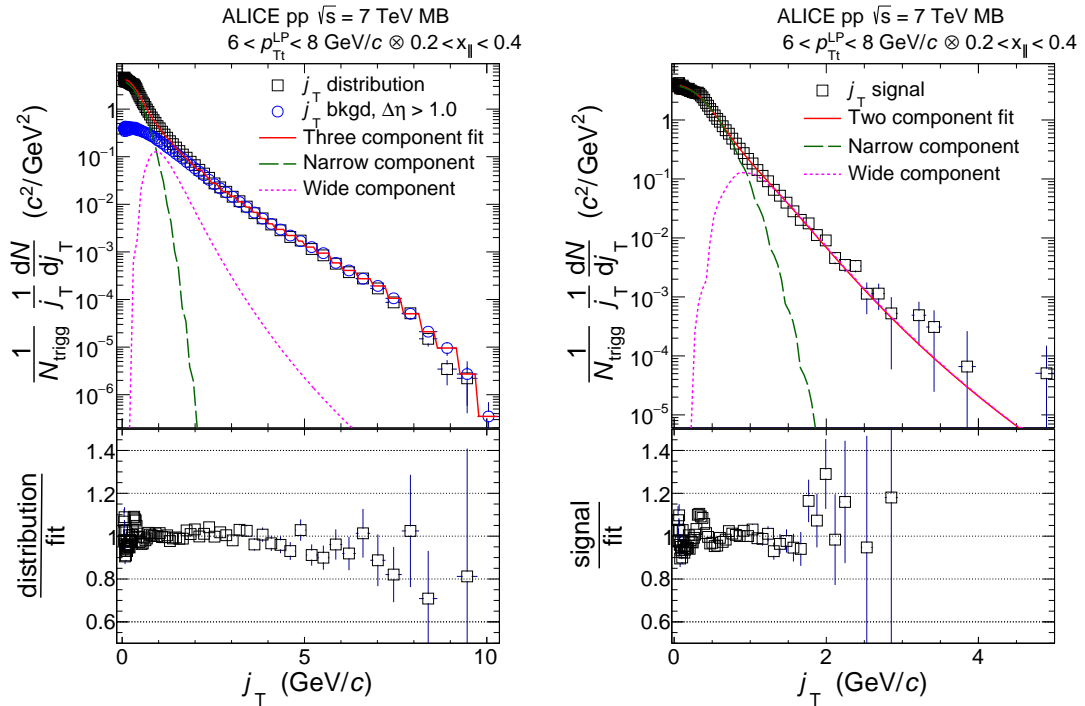


Figure 59: *Left:* Measured j_T distribution including a three-component fit. The three components describe the background (circular symbols), hadronization (long dashed line), and showering (short dashed line). *Right:* The same j_T distribution but with background subtracted.

¹⁹⁰⁴ The analysis was the first to introduce this factorisation of j_T into components.

At $j_T \approx 0.4\text{GeV}$ there is a small bump in the distribution to fit ratio. This was attributed to cases where the trigger particle decayed after hadronisation. As it is difficult to correct for, this bump is included in the systematic errors of the results.

The RMS results from the fitting in both pp and p–Pb collisions are shown in Fig. 60. Qualitatively the results are similar to jet j_T results. The RMS value of the wide component has an increasing trend with respect to p_{Tt}/p_{Tjet} , while the RMS value of the narrow component stays constant. Both components are well described by PYTHIA simulations. As seen in the figures there is no difference between pp and p–Pb results in the dihadron analysis.

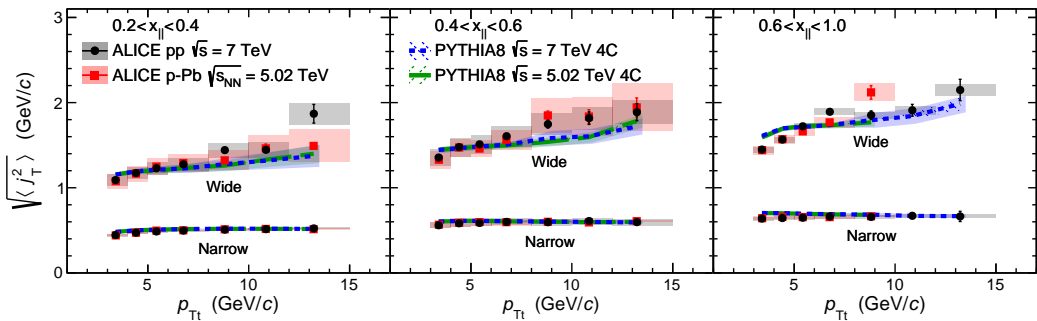


Figure 60: RMS values of the narrow and wide j_T components in the dihadron correlation analysis. Results from pp collisions at $\sqrt{s} = 7\text{ TeV}$ (circular symbols) and from p–Pb collisions at $\sqrt{s_{NN}} = 5.02\text{ TeV}$ (square symbols) are compared to PYTHIA 8 tune 4C simulations at $\sqrt{s} = 7\text{ TeV}$ (short dashed line) and at $\sqrt{s} = 5.02\text{ TeV}$ (long dashed line). Different panels correspond to different $x_{||}$ bins with $0.2 < x_{||} < 0.4$ on the left, $0.4 < x_{||} < 0.6$ in the middle, and $0.6 < x_{||} < 1.0$ on the right. The statistical errors are represented by bars and the systematic errors by boxes. [2]

7.2 Comparing dihadron and jet j_T results

Comparison to RMS values in dihadron analysis [2] are shown in figure 61. For comparison the dihadron trigger p_T bins are converted to jet p_T bins and vice versa. Bin-by-bin comparison is still not possible, but dihadron analysis gives systematically larger RMS values. This could be caused by several kinematical factors. In jet j_T analysis the jet cone limits possible j_T values and thus the width and RMS of the j_T distributions. The effect of this limitation can be studied by changing the cone size as is described in section 7.2.1.

The trends are similar in dihadron and jet j_T results. Wide component RMS values tend to increase with increasing $p_{T,trigger}/p_{Tjet}$. Narrow component RMS

1925 increases slightly in dihadron analysis but not in jet j_T , WHY? (Depends on $x_{||}$
 1926 bin in dihadron)

1927 In general dihadron j_T gives wider distributions with larger RMS values. In
 1928 jet analysis the cone size limits width and thus the RMS values. The effect of this
 1929 limitation can be studied by changing the cone size as is described in section 7.2.1.

1930 Additionally the leading track is an imperfect estimate of the jet/original par-
 1931 ton. Because the leading track in general is at an angle compared to the jet axis,
 1932 the resulting j_T values are different. In practice the jet axis found by the jet finding
 1933 algorithm tends to minimize the average j_T of jet constituents. Thus the yield
 1934 at high j_T is limited and the RMS values are smaller. The effect of having the
 1935 leading hadron as reference instead of the jet axis is discussed in section 7.2.2

1936 Lastly the results from the dihadron analysis are done in $p_{T\text{trigger}}$ bins. This
 1937 favours hard jets, i.e. jets where the leading hadron carries a large momentum
 1938 fraction and the jet multiplicity is small. In $p_{T\text{jet}}$ bins jets are more likely to be
 1939 soft, i.e. small leading momentum fraction and high multiplicity jets.

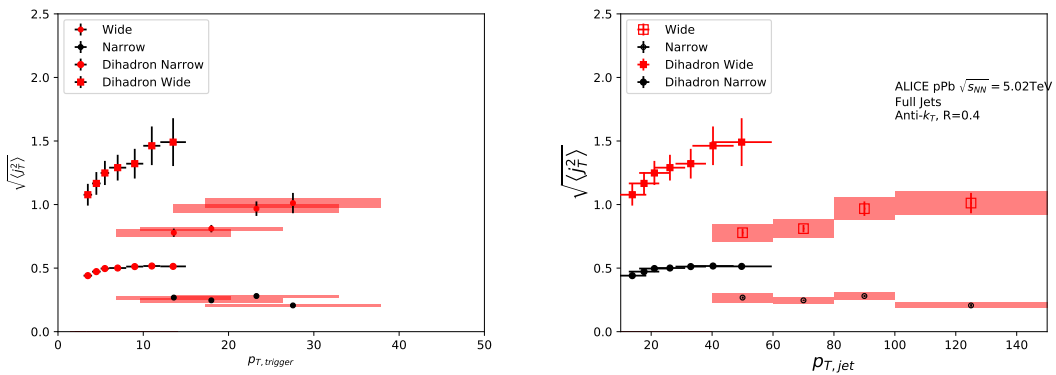


Figure 61: Jet j_T results are compared to results obtained in the dihadron analysis. Dihadron trigger p_T bins are converted to jet p_T bins using observed mean $p_{T\text{jet}}$ values in $p_{T\text{trigger}}$ bins. Dihadron results are for $0.2 < x_{||} < 0.4$

1940 7.2.1 Different R parameters

1941 The size of the jet cone gives a limit for j_T . For a track with a fixed momentum p
 1942 this is a hard limit. This is conveniently seen as j_T can be given in terms of cone
 1943 size R and momentum p in the small angle approximation limit as

$$j_T \approx p \cdot R \quad (60)$$

1944 Thus for tracks with $p_{T\text{track}} < p_{T0}$, $j_T < p_{T0} \times R$.

1945 In practice the effect of cone sizes on j_T distribution is studied in a PYTHIA simulation. Results of the individual distributions and resulting RMS values from this
 1946 simulation are shown in Fig. 62 and Fig. 63 respectively. Increasing the cone size
 1947 of jets gives more room for high j_T tracks. This is seen in the individual j_T distributions as increased high j_T production. At low j_T there is no change.
 1948

1950 When looking at RMS values from wide component we see an increase/decrease
 1951 of about 10% when going from $R = 0.4$ to $R = 0.5/R = 0.3$.

1952 The message from narrow component RMS values is less clear. At low jet p_T
 the behaviour is similar, but at high p_T the order is reversed.

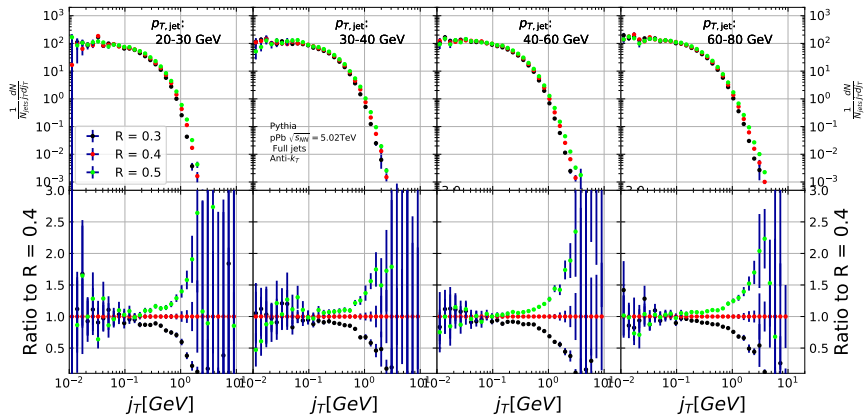


Figure 62: Effect of changing R parameter in jet finding on j_T distributions

1953

1954 7.2.2 Leading tracks versus jet

1955 The leading track is an imperfect estimate of the jet/original parton. Because the
 1956 leading track in general is at an angle compared to the jet axis, the resulting j_T
 1957 values are different. In practice the jet axis found by the jet finding algorithm
 1958 tends to minimize the average j_T of jet constituents. Thus the yield at high j_T is
 1959 limited and the RMS values are smaller.

1960 A PYTHIA study was performed where j_T was calculated with respect to the
 1961 leading track momentum, instead of the jet axis. The results are shown in Fig. 64.
 1962 The resulting j_T distributions are significantly wider than j_T distributions from
 1963 the typical method. The effect seems to be larger than the effect seen in comparing
 1964 different R values.

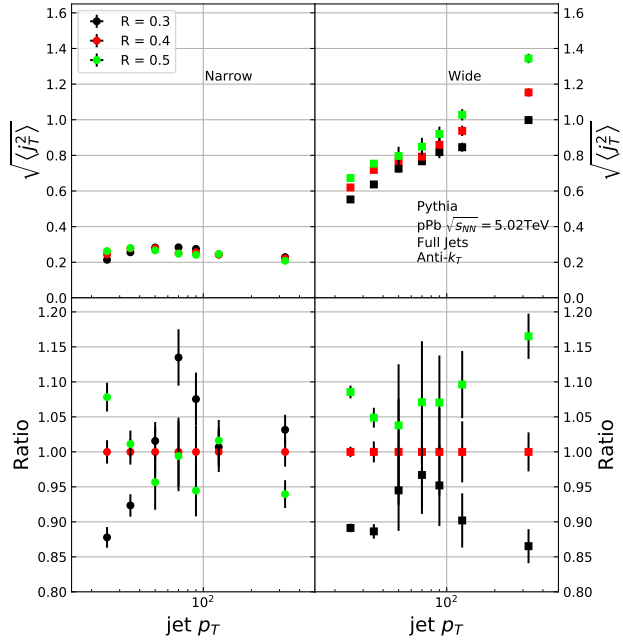


Figure 63: Effect of changing R parameter in jet finding on narrow and wide component RMS values. Wide component RMS values increase with increasing cone size.

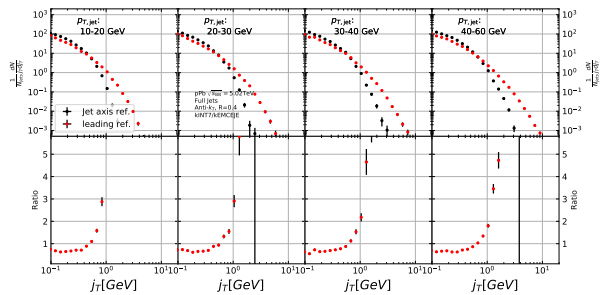


Figure 64: Results of calculating j_T with respect to the jet axis or the leading hadron. The assumption is that because the leading hadron is an imperfect estimate of the jet axis, low j_T tracks should on average be shifted to higher j_T

1965 **8 Summary**

1966 In this work two distinct j_T components were extracted for narrow and wide contributions using jet reconstruction in $\sqrt{s_{NN}} = 5.02$ TeV p–Pb collisions. RMS values 1967 for both components were obtained. The width of the wide component is found to 1968 increase for increasing $p_{T\text{jet}}$. This is in part explained by the changing kinematical limits when going to higher $p_{T\text{jet}}$ which allows higher $p_{T\text{track}}$. Additionally the 1969 1970 larger phase space allows stronger parton splitting. The results are qualitatively 1971 1972 compatible with previous studies that studied j_T using two-particle correlations.

1973 [Extend summary](#)

¹⁹⁷⁴ Appendices

¹⁹⁷⁵ A Additional graphs

¹⁹⁷⁶ References

- ¹⁹⁷⁷ [1] ALICE, J. Adam *et al.*, Phys. Rev. **C91**, 064905 (2015), 1412.6828.
- ¹⁹⁷⁸ [2] <https://alice-publications.web.cern.ch/node/3655>, 2018.
- ¹⁹⁷⁹ [3] PHENIX Collaboration, K. Adcox *et al.*, Nucl.Phys. **A757**, 184 (2005), nucl-ex/0410003.
- ¹⁹⁸⁰
- ¹⁹⁸¹ [4] STAR Collaboration, J. Adams *et al.*, Nucl.Phys. **A757**, 102 (2005), nucl-ex/0501009.
- ¹⁹⁸²
- ¹⁹⁸³ [5] J.-Y. Ollitrault, Phys. Rev. D **46**, 229 (1992).
- ¹⁹⁸⁴ [6] U. Heinz and P. Kolb, Nucl. Phys. **A702**, 269 (2002).
- ¹⁹⁸⁵ [7] E. Shuryak, Prog. Part. Nucl. Phys. **62**, 48 (2009).
- ¹⁹⁸⁶ [8] ATLAS Collaboration, J. Jia, Nucl.Phys.A904-905 **2013**, 421c (2013), 1209.4232.
- ¹⁹⁸⁷
- ¹⁹⁸⁸ [9] R. A. Lacey *et al.*, (2012), 1207.1886.
- ¹⁹⁸⁹ [10] R. Bjorklund, W. Crandall, B. J. Moyer, and H. York, Phys. Review **77**, 213 (1950).
- ¹⁹⁹⁰
- ¹⁹⁹¹ [11] W. Heisenberg, Zeitschrift für Physik **77**, 1 (1932).
- ¹⁹⁹² [12] M. Gell-Mann, Phys. Rev. **125**, 1067 (1962).
- ¹⁹⁹³ [13] M. Gell-Mann, Phys. Lett. **8**, 214 (1964).
- ¹⁹⁹⁴ [14] O. Greenberg, Phys. Rev. Lett. **13**, 598 (1964).
- ¹⁹⁹⁵ [15] Crystal Ball Collaboration, D. Williams *et al.*, Phys.Rev. **D38**, 1365 (1988).
- ¹⁹⁹⁶ [16] W. Krolikowski, Nuovo Cim. **A27**, 194 (1975).
- ¹⁹⁹⁷ [17] D. J. Gross and F. Wilczek, Physical Review Letters **30**, 1343 (1973).
- ¹⁹⁹⁸ [18] H. D. Politzer, Physical Review Letters **30**, 1346 (1973).
- ¹⁹⁹⁹ [19] D. J. Gross and F. Wilczek, Physical Review D **8**, 3633 (1973).
- ²⁰⁰⁰ [20] D. J. Gross and F. Wilczek, Physical Review D **9**, 980 (1974).
- ²⁰⁰¹ [21] H. Georgi and H. D. Politzer, Physical Review D **9**, 416 (1974).

- 2002 [22] H. Fritzsch, M. Gell-Mann, and H. Leutwyler, Physics Letters B **47**, 365
 2003 (1973).
- 2004 [23] I. Flegel and P. Söding, CERN courier (2004).
- 2005 [24] R. Brandelik *et al.*, Physics Letters B **86**, 243 (1979).
- 2006 [25] J. K. L. MacDonald, Phys. Rev. **43**, 830 (1933).
- 2007 [26] C. Berger *et al.*, Physics Letters B **86**, 418 (1979).
- 2008 [27] J. Collins and M. Perry, Phys. rev. Lett. **34**, 1353 (1975).
- 2009 [28] E. Shuryak, Phys. Reps. **61**, 71 (1980).
- 2010 [29] K. Rajagopal, SLAC Beam Line **31-2**, 9 (2001).
- 2011 [30] P. Kovtun, D. Son, and A. Starinets, Phys.Rev.Lett. **94**, 111601 (2005),
 2012 hep-th/0405231.
- 2013 [31] R. A. Lacey *et al.*, Phys. Rev. Lett. **98**, 092301 (2007).
- 2014 [32] E. Lofgren, *ACCELERATOR DIVISION ANNUAL REPORTS, 1 JULY*
 2015 *1972 12/31/1974* (, 1975).
- 2016 [33] D. S. Barton, Heavy ion program at bnl: Ags, rhic, in *Proc. 1987 Particle*
 2017 *Accelerator Conference, Washington, D.C., March, 1987*, 1987.
- 2018 [34] I. Vitev and M. Gyulassy, Phys.Rev.Lett. **89**, 252301 (2002), hep-
 2019 ph/0209161.
- 2020 [35] A. Kovalenko *et al.*, Status of the nuclotron, in *Proceedings of EPAC Vol. 94*,
 2021 pp. 161–164, 1994.
- 2022 [36] NA61/SHINE, K. Grebieszkow, PoS **CPOD2013**, 004 (2013).
- 2023 [37] BRAHMS Collaboration, I. Arsene *et al.*, Nucl.Phys. **A757**, 1 (2005), nucl-
 2024 ex/0410020.
- 2025 [38] B. Back *et al.*, Nucl.Phys. **A757**, 28 (2005), nucl-ex/0410022.
- 2026 [39] S. A. Voloshin, A. M. Poskanzer, and R. Snellings, (2008), 0809.2949.
- 2027 [40] S. A. Voloshin, A. M. Poskanzer, A. Tang, and G. Wang, Phys.Lett. **B659**,
 2028 537 (2008), 0708.0800.

- 2029 [41] H. Holopainen, H. Niemi, and K. J. Eskola, Phys.Rev. **C83**, 034901 (2011),
2030 1007.0368.
- 2031 [42] ALICE Collaboration, Phys. Rev. C **88**, 044909 (2013).
- 2032 [43] M. L. Miller, K. Reygers, S. J. Sanders, and P. Steinberg,
2033 Ann.Rev.Nucl.Part.Sci. **57**, 205 (2007), nucl-ex/0701025.
- 2034 [44] R. Glauber, Lectures in theoretical physics, 1959.
- 2035 [45] W. Czyż and L. Maximon, Annals of Physics **52**, 59 (1969).
- 2036 [46] A. Białas, M. Bleszyński, and W. Czyż, Nuclear Physics B **111**, 461 (1976).
- 2037 [47] PHENIX Collaboration, S. Afanasiev *et al.*, Phys.Rev. **C80**, 054907 (2009),
2038 0903.4886.
- 2039 [48] J.-Y. Ollitrault, Eur.J.Phys. **29**, 275 (2008), 0708.2433.
- 2040 [49] P. Romatschke, Int.J.Mod.Phys. **E19**, 1 (2010), 0902.3663.
- 2041 [50] L. LD, Izv. Akad. Nauk Ser. Fiz. **17**, 51 (1953).
- 2042 [51] J. D. Bjorken, Phys. Rev. D **27**, 140 (1983).
- 2043 [52] G. Baym, B. L. Friman, J. P. Blaizot, M. Soyeur, and W. Czyz, Nucl. Phys.
2044 **A407**, 541 (1983).
- 2045 [53] H. von Gersdorff, L. McLerran, M. Kataja, and P. V. Ruuskanen, Phys.
2046 Rev. D **34**, 794 (1986).
- 2047 [54] K. A. *et al.* [ALICE Collaboration], Phys. Rev. Lett **106** (2011), 032301.
- 2048 [55] J.-Y. Ollitrault, Phys.Rev. D **48**, 1132 (1993), hep-ph/9303247.
- 2049 [56] P. Danielewicz and G. Odyniec, Physics Letters B **157**, 146 (1985).
- 2050 [57] P. Danielewicz and M. Gyulassy, Physics Letters B **129**, 283 (1983).
- 2051 [58] T. Abbott *et al.*, Phys. Rev. Lett. **70**, 1393 (1993).
- 2052 [59] S. Voloshin and Y. Zhang, Z.Phys. **C70**, 665 (1996), hep-ph/9407282.
- 2053 [60] E877 Collaboration, J. Barrette *et al.*, Phys.Rev.Lett. **73**, 2532 (1994), hep-
2054 ex/9405003.

- 2055 [61] V. N. Gribov and L. N. Lipatov, Sov. J. Nucl. Phys. **15**, 438 (1972), [Yad.
2056 Fiz.15,781(1972)].
- 2057 [62] G. Altarelli and G. Parisi, Nucl. Phys. **B126**, 298 (1977).
- 2058 [63] Y. L. Dokshitzer, Sov. Phys. JETP **46**, 641 (1977), [Zh. Eksp. Teor.
2059 Fiz.73,1216(1977)].
- 2060 [64] Y. I. Azimov, Y. L. Dokshitzer, V. A. Khoze, and S. I. Trovan, Zeitschrift
2061 für Physik C Particles and Fields **27**, 65 (1985).
- 2062 [65] B. Andersson, G. Gustafson, G. Ingelman, and T. Sjöstrand, Physics Reports
2063 **97**, 31 (1983).
- 2064 [66] A. Buckley *et al.*, Phys. Rept. **504**, 145 (2011), 1101.2599.
- 2065 [67] M. Bahr *et al.*, Eur. Phys. J. **C58**, 639 (2008), 0803.0883.
- 2066 [68] ALICE Collaboration, K. Aamodt *et al.*, Phys.Lett. **B696**, 30 (2011),
2067 1012.1004.
- 2068 [69] WA98 Collaboration, M. Aggarwal *et al.*, Eur.Phys.J. **C23**, 225 (2002),
2069 nucl-ex/0108006.
- 2070 [70] D. G. d'Enterria, Phys.Lett. **B596**, 32 (2004), nucl-ex/0403055.
- 2071 [71] PHENIX Collaboration, A. Adare *et al.*, Phys.Rev.Lett. **101**, 232301 (2008),
2072 0801.4020.
- 2073 [72] STAR Collaboration, J. Adams *et al.*, Phys.Rev.Lett. **91**, 172302 (2003),
2074 nucl-ex/0305015.
- 2075 [73] A. Dainese, C. Loizides, and G. Paic, Eur.Phys.J. **C38**, 461 (2005), hep-
2076 ph/0406201.
- 2077 [74] I. Vitev, J.Phys. **G30**, S791 (2004), hep-ph/0403089.
- 2078 [75] C. A. Salgado and U. A. Wiedemann, Phys.Rev. **D68**, 014008 (2003), hep-
2079 ph/0302184.
- 2080 [76] N. Armesto, A. Dainese, C. A. Salgado, and U. A. Wiedemann, Phys.Rev.
2081 **D71**, 054027 (2005), hep-ph/0501225.
- 2082 [77] T. Renk, H. Holopainen, R. Paatelainen, and K. J. Eskola, Phys.Rev. **C84**,
2083 014906 (2011), 1103.5308.

- 2084 [78] CMS Collaboration, S. Chatrchyan *et al.*, Eur.Phys.J. **C72**, 1945 (2012),
2085 1202.2554.
- 2086 [79] PHENIX Collaboration, S. Afanasiev *et al.*, Phys. Rev. C **80**, 054907 (2009).
- 2087 [80] ALICE Collaboration, K. Aamodt *et al.*, Phys.Rev.Lett. **108**, 092301 (2012),
2088 1110.0121.
- 2089 [81] R. Baier, Y. L. Dokshitzer, A. H. Mueller, S. Peigne, and D. Schiff, Nucl.
2090 Phys. **B484**, 265 (1997), hep-ph/9608322.
- 2091 [82] W. H. H. Bethe and, Proc.Roy.Soc.Lond. **A146** (1934).
- 2092 [83] L. D. Landau and I. Pomeranchuk, Dokl. Akad. Nauk Ser. Fiz. **92**, 535
2093 (1953).
- 2094 [84] A. B. Migdal, Phys. Rev. **103**, 1811 (1956).
- 2095 [85] P. Bosted *et al.*, Quantum-mechanical suppression of bremsstrahlung*, 1993.
- 2096 [86] A. Majumder and M. Van Leeuwen, Prog.Part.Nucl.Phys. **A66**, 41 (2011),
2097 1002.2206.
- 2098 [87] F. Dominguez, C. Marquet, A. Mueller, B. Wu, and B.-W. Xiao, Nucl.Phys.
2099 **A811**, 197 (2008), 0803.3234.
- 2100 [88] M. Gyulassy, P. Levai, and I. Vitev, Nucl.Phys. **B571**, 197 (2000), hep-
2101 ph/9907461.
- 2102 [89] U. A. Wiedemann, Nucl.Phys. **B588**, 303 (2000), hep-ph/0005129.
- 2103 [90] P. B. Arnold, G. D. Moore, and L. G. Yaffe, JHEP **0112**, 009 (2001), hep-
2104 ph/0111107.
- 2105 [91] X.-N. Wang and X.-f. Guo, Nucl.Phys. **A696**, 788 (2001), hep-ph/0102230.
- 2106 [92] T. Sjostrand, S. Mrenna, and P. Z. Skands, Comput.Phys.Commun. **178**,
2107 852 (2008), 0710.3820.
- 2108 [93] I. Lokhtin and A. Snigirev, Eur.Phys.J. **C45**, 211 (2006), hep-ph/0506189.
- 2109 [94] N. Armesto, L. Cunqueiro, and C. A. Salgado, Nucl.Phys. **A830**, 271C
2110 (2009), 0907.4706.
- 2111 [95] K. Zapp, G. Ingelman, J. Rathsman, J. Stachel, and U. A. Wiedemann,
2112 Eur.Phys.J. **C60**, 617 (2009), 0804.3568.

- 2113 [96] T. Renk, Phys.Rev. **C79**, 054906 (2009), 0901.2818.
- 2114 [97] PHENIX, K. Adcox *et al.*, Phys. Rev. Lett. **88**, 022301 (2002), nucl-ex/0109003.
- 2116 [98] STAR, J. Adams *et al.*, Phys. Rev. Lett. **91**, 072304 (2003), nucl-ex/0306024.
- 2117 [99] BRAHMS, I. Arsene *et al.*, Phys. Rev. Lett. **91**, 072305 (2003), nucl-ex/0307003.
- 2119 [100] CMS, V. Khachatryan *et al.*, JHEP **04**, 039 (2017), 1611.01664.
- 2120 [101] ALICE, S. Acharya *et al.*, JHEP **11**, 013 (2018), 1802.09145.
- 2121 [102] PHENIX, A. Adare *et al.*, Phys. Rev. **C77**, 011901 (2008), 0705.3238.
- 2122 [103] PHENIX, A. Adare *et al.*, Phys. Rev. Lett. **111**, 032301 (2013), 1212.3323.
- 2123 [104] ALICE, J. Adam *et al.*, Phys. Lett. **B746**, 1 (2015), 1502.01689.
- 2124 [105] CMS, A. M. Sirunyan *et al.*, Phys. Rev. Lett. **121**, 242301 (2018), 1801.04895.
- 2126 [106] CMS, S. Chatrchyan *et al.*, Phys. Rev. **C90**, 024908 (2014), 1406.0932.
- 2127 [107] ALICE, S. Acharya *et al.*, JHEP **10**, 139 (2018), 1807.06854.
- 2128 [108] A. Kurkela and U. A. Wiedemann, Phys. Lett. **B740**, 172 (2015), 1407.0293.
- 2129 [109] JETSCAPE, Y. Tachibana *et al.*, Jet substructure modification in a QGP from a multi-scale description of jet evolution with JETSCAPE, 2018, 1812.06366.
- 2132 [110] P. Aurenche and B. G. Zakharov, Eur. Phys. J. **C71**, 1829 (2011), 1109.6819.
- 2133 [111] A. Beraudo, J. G. Milhano, and U. A. Wiedemann, Phys. Rev. **C85**, 031901 (2012), 1109.5025.
- 2135 [112] A. Beraudo, J. G. Milhano, and U. A. Wiedemann, JHEP **07**, 144 (2012), 1204.4342.
- 2137 [113] J. Casalderrey-Solana, Y. Mehtar-Tani, C. A. Salgado, and K. Tywoniuk, Phys. Lett. **B725**, 357 (2013), 1210.7765.
- 2139 [114] F. D'Eramo, M. Lekaveckas, H. Liu, and K. Rajagopal, JHEP **05**, 031 (2013), 1211.1922.

- ²¹⁴¹ [115] A. Ayala, I. Dominguez, J. Jalilian-Marian, and M. E. Tejeda-Yeomans, Phys. Rev. **C94**, 024913 (2016), 1603.09296.
- ²¹⁴³ [116] J. L. Nagle and W. A. Zajc, Ann. Rev. Nucl. Part. Sci. **68**, 211 (2018), 1801.03477.
- ²¹⁴⁵ [117] E735, T. Alexopoulos *et al.*, Phys. Rev. **D48**, 984 (1993).
- ²¹⁴⁶ [118] MiniMax, T. C. Brooks *et al.*, Phys. Rev. **D61**, 032003 (2000), hep-ex/9906026.
- ²¹⁴⁸ [119] C. Shen, Z. Qiu, and U. Heinz, Phys. Rev. **C92**, 014901 (2015), 1502.04636.
- ²¹⁴⁹ [120] PHENIX, A. Adare *et al.*, Phys. Rev. **C94**, 064901 (2016), 1509.07758.
- ²¹⁵⁰ [121] C. A. Salgado and J. P. Wessels, Ann. Rev. Nucl. Part. Sci. **66**, 449 (2016).
- ²¹⁵¹ [122] M. Gyulassy, I. Vitev, X.-N. Wang, and B.-W. Zhang, p. 123 (2003), nucl-th/0302077.
- ²¹⁵³ [123] E. Norbeck, K. Šafařík, and P. A. Steinberg, Annual Review of Nuclear and Particle Science **64**, 383 (2014), <https://doi.org/10.1146/annurev-nucl-102912-144532>.
- ²¹⁵⁶ [124] A. Accardi, F. Arleo, W. K. Brooks, D. D'Enterria, and V. Muccifora, Riv. Nuovo Cim. **32**, 439 (2010), 0907.3534.
- ²¹⁵⁸ [125] 2019.
- ²¹⁵⁹ [126] P. M. Watkins, Contemp. Phys. **27**, 291 (1986).
- ²¹⁶⁰ [127] Cern experiments, 2019.
- ²¹⁶¹ [128] O. S. Brüning *et al.*, *LHC Design Report*CERN Yellow Reports: Monographs (CERN, Geneva, 2004).
- ²¹⁶³ [129] ATLAS, G. Aad *et al.*, Phys. Lett. **B716**, 1 (2012), 1207.7214.
- ²¹⁶⁴ [130] CMS, S. Chatrchyan *et al.*, Phys. Lett. **B716**, 30 (2012), 1207.7235.
- ²¹⁶⁵ [131] LHCb, A. A. Alves, Jr. *et al.*, JINST **3**, S08005 (2008).
- ²¹⁶⁶ [132] LHCf, O. Adriani *et al.*, JINST **3**, S08006 (2008).
- ²¹⁶⁷ [133] TOTEM, G. Anelli *et al.*, JINST **3**, S08007 (2008).
- ²¹⁶⁸ [134] MoEDAL, B. Acharya *et al.*, JHEP **08**, 067 (2016), 1604.06645.

- ²¹⁶⁹ [135] T. ALICE Collaboration *et al.*, Journal of Instrumentation **3**, S08002 (2008).
- ²¹⁷⁰ [136] ALICE, K. Aamodt *et al.*, Phys. Rev. Lett. **105**, 252301 (2010), 1011.3916.
- ²¹⁷¹ [137] ALICE, G. Dellacasa *et al.*, (2000).
- ²¹⁷² [138] ALICE, G. Dellacasa *et al.*, (1999).
- ²¹⁷³ [139] ALICE, I. Belikov, EPJ Web Conf. **125**, 01004 (2016), 1607.01171.
- ²¹⁷⁴ [140] ALICE Collaboration, B. Abelev *et al.*, CERN Report No. CERN-LHCC-2012-012. LHCC-I-022. ALICE-UG-002, 2012 (unpublished).
- ²¹⁷⁵
- ²¹⁷⁶ [141] Report No. CERN-LHCC-2015-001. ALICE-TDR-018, 2015 (unpublished).
- ²¹⁷⁷ [142] The ALICE Collaboration, Report No. CERN-LHCC-2013-020. ALICE-TDR-016, 2013 (unpublished).
- ²¹⁷⁸
- ²¹⁷⁹ [143] M. Vargyas, *Jet shape modification in Pb-Pb collisions at $\sqrt{s_{NN}} = 2.76 \text{ TeV}$ using two-particle correlations*, PhD thesis, University of Jyväskylä, 2018.
- ²¹⁸⁰
- ²¹⁸¹ [144] ALICE TPC upgrade, J. E. Brückner and T. E. Hildén, The GEM QA Protocol of the ALICE TPC Upgrade Project, in *5th International Conference on Micro Pattern Gas Detectors (MPGD2017) Temple University, Philadelphia, USA, May 22-26, 2017*, 2018, 1811.07043.
- ²¹⁸²
- ²¹⁸³
- ²¹⁸⁴
- ²¹⁸⁵ [145] T. Hildén *et al.*, Nucl. Instrum. Meth. **A770**, 113 (2015), 1704.06691.
- ²¹⁸⁶ [146] ALICE Collaboration, P. Cortese, *ALICE transition-radiation detector: Technical Design Report* Technical Design Report ALICE (CERN, Geneva, 2001).
- ²¹⁸⁷
- ²¹⁸⁸
- ²¹⁸⁹ [147] ALICE, G. Dellacasa *et al.*, (2000).
- ²¹⁹⁰ [148] ALICE, S. Beole *et al.*, (1998).
- ²¹⁹¹ [149] for the ALICE, C. Zampolli, Particle Identification with the ALICE detector at the LHC, in *Proceedings, PLHC2012: Physics at the LHC 2012 (PLHC2012): Vancouver, BC, Canada, June 4-9, 2012*, 2012, 1209.5637.
- ²¹⁹²
- ²¹⁹³
- ²¹⁹⁴ [150] ALICE, G. Dellacasa *et al.*, (1999).
- ²¹⁹⁵ [151] ALICE, P. Cortese *et al.*, (2008).
- ²¹⁹⁶ [152] J. Allen *et al.*, Report No. CERN-LHCC-2010-011. ALICE-TDR-14-add-1, 2010 (unpublished).
- ²¹⁹⁷

- ₂₁₉₈ [153] ALICE, P. Cortese *et al.*, (2004).
- ₂₁₉₉ [154] ALICE, A. I. Maevskaya, (2018), 1812.00594.
- ₂₂₀₀ [155] ALICE Collaboration, *ALICE Photon Multiplicity Detector (PMD): Technical Design Report*Technical Design Report ALICE (CERN, Geneva, 1999).
- ₂₂₀₂ [156] ACORDE, A. Fernández *et al.*, Nucl. Instrum. Meth. **A572**, 102 (2007),
₂₂₀₃ physics/0606051.
- ₂₂₀₄ [157] ALICE, G. Dellacasa *et al.*, (1999).
- ₂₂₀₅ [158] ALICE, B. Abelev *et al.*, Phys. Rev. **C88**, 044909 (2013), 1301.4361.
- ₂₂₀₆ [159] ALICE, S. Beole *et al.*, (1996).
- ₂₂₀₇ [160] J. Král, *Intrinsic transverse momentum distribution of jet constituents in p-Pb collisions at ALICE*, PhD thesis, University of Jyväskylä, 2014.
- ₂₂₀₉ [161] J. Kral, T. Awes, H. Muller, J. Rak, and J. Schambach, Nuclear Instruments
₂₂₁₀ and Methods in Physics Research Section A: Accelerators, Spectrometers,
₂₂₁₁ Detectors and Associated Equipment **693**, 261 (2012).
- ₂₂₁₂ [162] ALICE, K. Aamodt *et al.*, JINST **3**, S08002 (2008).
- ₂₂₁₃ [163] ALICE, B. B. Abelev *et al.*, Int. J. Mod. Phys. **A29**, 1430044 (2014),
₂₂₁₄ 1402.4476.
- ₂₂₁₅ [164] ALICE, K. Aamodt *et al.*, JINST **5**, P03003 (2010), 1001.0502.
- ₂₂₁₆ [165] J. Alme *et al.*, Nucl. Instrum. Meth. **A622**, 316 (2010), 1001.1950.
- ₂₂₁₇ [166] R. Fruhwirth, Nucl. Instrum. Meth. **A262**, 444 (1987).
- ₂₂₁₈ [167] ALICE, B. Abelev *et al.*, JHEP **03**, 053 (2012), 1201.2423.
- ₂₂₁₉ [168] ALICE, B. Abelev *et al.*, Phys. Lett. **B719**, 29 (2013), 1212.2001.
- ₂₂₂₀ [169] M. Cacciari, G. P. Salam, and G. Soyez, Eur. Phys. J. **C72**, 1896 (2012),
₂₂₂₁ 1111.6097.
- ₂₂₂₂ [170] M. Cacciari, G. P. Salam, and G. Soyez, JHEP **04**, 063 (2008), 0802.1189.
- ₂₂₂₃ [171] T. Sjöstrand, S. Mrenna, and P. Z. Skands, Comput. Phys. Commun. **178**,
₂₂₂₄ 852 (2008), 0710.3820.

- 2225 [172] Roounfold: Root unfolding framework, <http://hepunx.rl.ac.uk/~adye/software/unfold/RooUnfold.html>, 2013.
- 2226
- 2227 [173] CMS, S. Chatrchyan *et al.*, Phys. Rev. **D90**, 072006 (2014), 1406.0324.
- 2228 [174] M. Dasgupta, L. Magnea, and G. P. Salam, JHEP **02**, 055 (2008), 0712.3014.